Naval Research Laboratory
Stennis Space Center, MS 39529-5004

NRL/FR/7322--97-9672

A Comparison of Several Coastal Ocean Models

PAUL J. MARTIN

Ocean Dynamics and Prediction Branch
Oceanography Division

GERMANA PEGGION

Center for Ocean and Atmospheric Modeling
University of Southern Mississippi
Stennis Space Center, MS

K. JOSEPH YIP

Department of Oceanography
Texas A&M University
College Station, TX

December 31, 1998

REPORT DOCUMENTATION PAGE

Form Approved
OBM No. 0704-0188

1. AGENCY USE ONLY *(Leave blank)*	2. REPORT DATE	3. REPORT TYPE AND DATES COVERED
	December 31, 1998	Final

4. TITLE AND SUBTITLE
A Comparison of Several Coastal Ocean Models

5. FUNDING NUMBERS
Job Order No. 573W10008
Program Element No. 0602435N
Project No.
Task No.
Accession No. DN16-4296

6. AUTHOR(S)
Paul J. Martin, Germana Peggion*, and K. Joseph Yip**

7. PERFORMING ORGANIZATION NAME(S) AND ADDRESS(ES)
Naval Research Laboratory
Oceanography Division
Stennis Space Center, MS 39529-5004

8. PERFORMING ORGANIZATION REPORT NUMBER
NRL/FR/7322--97-9672

9. SPONSORING/MONITORING AGENCY NAME(S) AND ADDRESS(ES)
Office of Naval Research
800 N. Quincy St.
Arlington, VA 22217-5000

10. SPONSORING/MONITORING AGENCY REPORT NUMBER

11. SUPPLEMENTARY NOTES
*Center for Ocean and Atmospheric Modeling, University of Southern Mississippi, Stennis Space Center, MS
**Department of Oceanography, Texas A&M University, College Station, TX

12a. DISTRIBUTION/AVAILABILITY STATEMENT
Approved for public release; distribution unlimited.

12b. DISTRIBUTION CODE

13. ABSTRACT *(Maximum 200 words)*

Several ocean models that are being used for coastal ocean simulation and prediction were tested for their ability to simulate physical processes of importance in the coastal ocean. The models tested were the Princeton Ocean Model, the Estuarine and Coastal Ocean Model, semi-implicit version (ECOM-si), the Sigma/z-level Model, and the S-Coordinate, Rutgers University Model (SCRUM), Version 2.1. The basic processes for which the models were tested included advection, vertical mixing, propagation of surface, internal, and coastal trapped waves, and the formation of upwelling and downwelling fronts.

The model tests revealed some particular problems and limitations of the individual models and parameterizations. The forward time-differencing scheme used by ECOM-si suffers from significantly higher truncation error than the leapfrog and Adams-Bashforth schemes used by the other models. The sigma vertical coordinate system can suffer from advective overshoot if there are large changes in depth between adjacent gridpoints, and also from spurious diffusive effects, depending on how the horizontal diffusion is treated. The step-like bottom of a *z*-level vertical grid in which the bathymetry is rounded to the nearest model level can incur error due to the inaccurate representation of the bottom depth. The Crank-Nicolson treatment of vertical mixing in SCRUM 2.1 generates noisy, inaccurate vertical mixing due to diffusive overshoot when the vertical eddy coefficients are large.

14. SUBJECT TERMS	15. NUMBER OF PAGES
ocean model, coastal, modeling, numerical model	99
	16. PRICE CODE

17. SECURITY CLASSIFICATION OF REPORT	18. SECURITY CLASSIFICATION OF THIS PAGE	19. SECURITY CLASSIFICATION OF ABSTRACT	20. LIMITATION OF ABSTRACT
Unclassified	Unclassified	Unclassified	Same as report

CONTENTS

A COMPARISON OF SEVERAL COASTAL OCEAN MODELS

1.0 INTRODUCTION

This report presents results from a comparison of several ocean models that are being used for coastal simulation and prediction. The models are tested to determine their ability to simulate basic physical processes of importance in the coastal ocean. The purpose of the comparison is to look at the pros and cons of the models, to identify particular problems, and to provide a baseline for testing future models and making improvements. The overall goal is to try to determine the best models and/or parameterizations for either general or particular applications.

Physical processes important in the coastal ocean include tides, wind setup and storm surge, wind-driven circulation, river outflows and fresh water runoff, surface and internal waves, advection, mixing, coastal-trapped waves, upwelling and downwelling, and frontal dynamics. With the exception of short-spatial-scale, non-hydrostatic effects, e.g., such as occur with short-wavelength, high-amplitude internal waves, these processes can generally be adequately simulated with hydrostatic, three-dimensional (3-D) models of the type to be compared in this study.

We note that sediment and biological processes and their effect on the water's optical properties are also very important in the coastal environment. However, investigation of these processes, which requires that sediment, biological, and optical submodels be linked to the ocean circulation models, is not addressed here.

The model comparison was restricted to ocean models that include a free surface and predict the 3-D fields of ocean currents, temperature, and salinity. A number of widely used ocean models employ a rigid lid to filter out surface gravity waves and avoid the timestep restriction imposed by surface waves. Rigid-lid models can be used to investigate many important coastal processes. However, a free surface is needed for the prediction of tides and storm surge. Hence, a model that is to be used to simulate the complete range of coastal processes should have a free surface.

The models compared here include the Princeton Ocean Model (POM), which was originally developed by Alan Blumberg and George Mellor (Blumberg and Mellor 1987); the Estuarine and Coastal Ocean Model, Semi-Implicit version (ECOM-si) of Alan Blumberg, which is based on the original Princeton model, but has some significant modifications (Blumberg 1992); the Sigma *z*-level model (SZM), developed in house at the Naval Research Laboratory (NRL) (Martin 1998); and the S-Coordinate Rutgers University Model (SCRUM), which was developed by Tony Song and Dale Haidvogel (Song and Haidvogel 1994).

POM is probably the most widely used of all baroclinic coastal ocean models and has been applied to a wide range of coastal problems. A list of publications in which POM has been used is available from the POM ftp site at Princeton University (ftp.gfdl.gov) and has over 100 listings. POM was originally developed by Alan Blumberg and George Mellor in the early 1980s. Since that

time, there have been contributions to the program by others, notably Leo Oey, Boris Galperin, and Lakshmi Kantha. The major features of POM are (a) the use of an Arakawa "C" grid, (b) second-order, centered spatial finite differencing, (c) leapfrog time differencing with an Asselin temporal filter to eliminate time splitting, (d) an explicit treatment of the surface waves using a smaller timestep than that used for the internal mode, (e) a sigma (bottom following) vertical coordinate, (f) an implicit treatment of vertical mixing, and (g) the use of the Mellor-Yamada Level 2.5 (MYL2.5) turbulence scheme to calculate vertical mixing.

ECOM-si is based on POM, but contains some significant modifications that were implemented by Alan Blumberg, Vincenzo Casulli, and Ralph Cheng. The main differences from POM are (a) the use of a two-time-level temporal scheme rather than leapfrog, (b) the use of an implicit rather than an explicit scheme for the free surface, and (c) the addition of a wetting/drying capability.

SZM was developed at NRL to provide a model than can use both sigma and z-level (i.e., fixed depth) vertical coordinates. The model uses sigma coordinates down to a user-specified depth and z-levels below. This allows some flexibility in setting up the vertical grid and allows comparisons to be made between sigma and z-level coordinates. In other respects, SZM is similar to POM, except that it has an implicit treatment of the free surface and uses the simpler Mellor-Yamada Level 2 (MYL2) turbulence scheme.

SCRUM is one of a variety of ocean models that have been developed by Dale Haidvogel's ocean modeling group at Rutgers University. Dale Haidvogel's group is known for trying a wide range of ocean modeling techniques, including spectral and finite element (FE) methods. The best known of their models is the Semi-spectral Primitive Equation Model (SPEM) (Haidvogel et al. 1991). SPEM has been used in a number of modeling studies that have appeared in the oceanographic literature; however, SPEM is limited for coastal applications because of its rigid lid.

SCRUM (Version 2.1) uses finite differences (FD) in the horizontal, but uses FE in the vertical. Other major differences from the other models being compared here are (a) the use of a third-order Adams-Bashforth temporal scheme for most the baroclinic terms, (b) the use of the Crank-Nicolson semi-implicit scheme for vertical advection and mixing, and (c) the use of a generalized sigma coordinate system in the vertical, called an "S" coordinate by Song and Haidvogel, that allows changing the relative spacing of the vertical layers as the depth of the water changes. The "S" coordinate allows greater flexibility in setting vertical resolution than a standard sigma coordinate, e.g., it allows one to maintain a minimum resolution in the surface and/or bottom boundary layers as the water depth increases. SCRUM uses a split-explicit scheme for the free surface and offers a choice of turbulence schemes, MYL2, Price, and Pacanowski and Philander (PP) to calculate the vertical mixing coefficients.

A problem that was encountered in testing SCRUM was that during the period over which the model comparisons were conducted, SCRUM was still undergoing some development. The version of SCRUM that was started with, Version 2.1, was discovered to have some problems, and testing was begun on the other three models while waiting for a more fully developed version of SCRUM to become available. About this time, Tony Song (who did most of the original development of SCRUM) left Rutgers, and the development of SCRUM at Rutgers was continued by Hernan Arango. SCRUM Version 3.0 was released by Rutgers (Arango, pers. comm.) in August 1996. This version of SCRUM differed significantly from the previous version, a major change being that the FE scheme used in the vertical had been replaced by a FD scheme similar to that used by the other models. Because of the goal of finishing up the initial phase of the model comparison study at this time, it was deemed too late to begin testing a new version of SCRUM. Hence, the discussion of

SCRUM in this report refers to Version 2.1 that was originally received. Since a fully sorted version of this model was never obtained, most of the tests that were conducted do not include results from SCRUM.

Besides the models being tested here, there are, of course, a significant number of other coastal models in current use. Practical considerations limited the number of models that could be included in this study, but some particular models of interest will be briefly mentioned.

Curvilinear Hydrodynamics in 3 Dimensions (CH3D) is a coastal, baroclinic model that is being used by the Coastal Engineering Research Center (CERC) of the U. S. Army Corps of Engineers (Johnson et al. 1991). This model was initially developed for CERC by Peter Sheng of the University of Florida, who has been active in coastal and lake modeling since the 1970s. CERC is a FD model and is similar in formulation to POM. In recent years, CH3D has been maintained and developed by CERC.

The Tidal, Residual, Intertidal Mudflat, Three-Dimensional Model (TRIM-3D) is a FD coastal and estuary model developed by Vince Casulli and Ralph Cheng (Casulli and Cheng 1993). A unique feature of TRIM-3D is that grid cells over land are not included in the model's storage arrays or calculations. This allows a very large increase in efficiency in simulating coastal and estuary systems in which a large fraction of the volume encompassed by the domain being investigated is land. TRIM-3D has been applied to estuary systems in which the ratio of sea points to land points within the 3-D volume encompassing the estuary system is less than 2% (Casulli and Cheng 1993). NRL has recently developed a version of POM in which land areas have, in a similar fashion, been eliminated from the array storage and model calculations (Ko, pers. comm.).

David Dietrich of Mississippi State University has developed a free surface version of his DieCAST model (Dietrich and Mehra 1998). The original version of DieCAST, which uses a rigid lid, is able to form and maintain mesoscale circulation features and fronts with relatively low horizontal resolution (Dietrich et al. 1993; Dietrich and Ko 1994).

Dan Lynch of Dartmouth University, one of the pioneers in the development and application of barotropic FE ocean models, has developed a baroclinic FE model called QUODDY3 (Lynch and Werner 1991). This model is currently being applied by Dan Lynch and colleagues to the Maine Coastal Current (Naimie et al. 1994). FE models are more complex to program than FD models, but their very flexible horizontal grids allow large changes in spatial resolution over short distances, which provides significant advantages in modeling coastal regions with complex coastlines and bathymetry. (NRL has recently acquired and begun working with QUODDY3.)

The models being compared in this study, POM, ECOM-si, SZM, and SCRUM, although similar in many ways, have some significant differences: (a) explicit versus implicit treatment of the free surface, (b) sigma versus z-level vertical coordinates, (c) different temporal differencing schemes, and (d) different vertical mixing submodels. This study will consider how these differences affect model performance.

The model tests conducted here consist of tests of basic physical processes, including advection, mixing, propagation of free and coastal-trapped waves, and formation of upwelling and downwelling fronts. There are several reasons for conducting tests of basic physical processes, rather than tests of more complex coastal situations and comparisons with observations:

- Coastal models are sometimes applied without good knowledge of how well they simulate basic physical processes.

- Knowledge of model performance in simulating basic processes can aid interpretation of results in realistic situations and help in identifying the cause of model-related problems.
- Model comparisons with real data are not always conclusive because of uncertainties in initial conditions, boundary conditions, forcing, and validation data.
- Particular simulations with real data may not provide a good test of all the important physical processes.
- Tests of basic processes can uncover problems with the models that may not be evident in particular simulations with real data.

It is acknowledged, however, that comparison with observations is the final arbiter of model skill. There are a number of studies being conducted with coastal ocean models at NRL and at other institutions where the primary focus is the comparison of model results with observations. We consider the model tests conducted here to be complimentary to these other studies.

The sections that follow include (2.0) a description of the models, (3.0)–(8.0) a discussion of the results of the various model comparison test cases, and (9.0) a summary.

2.0 DESCRIPTION OF THE MODELS

The description of the models provided here is not complete in all details. The reader is referred to the references provided for the models for a more complete description. The emphasis here is on how the model formulations differ from each other. Hence, rather than sequentially present a complete description of each model, the different aspects of the models, i.e., the horizontal and vertical coordinate systems used, the spatial and temporal differencing, the treatment of the free surface, and the parameterization of horizontal and vertical mixing, are discussed in turn for all the models. There is some additional discussion of the physics and numerics of the models in the sections describing the model tests. A listing of some of the main features of the models is presented in Table 1.

2.1 Basic Equations

All the models have a free surface and employ the hydrostatic, Boussinesq, and incompressible approximations. The equations that the models solve, written in Cartesian coordinates, are

$$\frac{\partial u}{\partial t} = -\nabla \cdot (\mathbf{v}u) + fv - \frac{1}{\rho_o}\frac{\partial p}{\partial x} + F_u + \frac{\partial}{\partial z}\left(K_M \frac{\partial u}{\partial z}\right), \tag{1}$$

$$\frac{\partial v}{\partial t} = -\nabla \cdot (\mathbf{v}v) - fu - \frac{1}{\rho_o}\frac{\partial p}{\partial y} + F_v + \frac{\partial}{\partial z}\left(K_M \frac{\partial v}{\partial z}\right), \tag{2}$$

$$p = -\rho g, \tag{3}$$

$$\frac{\partial u}{\partial x} + \frac{\partial v}{\partial y} + \frac{\partial w}{\partial z} = 0, \tag{4}$$

Table 1 — Comparison of Some of the Features of Models Being Tested in Comparison Study

	POM	ECOM-si	SZM	SCRUM
Horizontal Grid	C-Grid Curvilinear	C-Grid Curvilinear	C-Grid Cartesian	C-Grid Curvilinear
Vertical Grid	Sigma	Sigma	Sigma/*z*-level	S-Coord
Barotropic Mode	Split-Explict Leapfrog	Implict Two-Time Level	Semi-Explict Leapfrog	Split-Explicit Leapfrog
Horizontal FD	Second-Order	Second-Order	Second-Order	Second-Order
Vertical FD	Second-Order	Second-Order	Second-Order	Linear FE
Horizontal Mixing	Laplacian Smagorinsky	Laplacian Smagorinsky	Laplacian Grid Cell-RE	Laplacian or Biharmonic
Vertical Turbulence	MYL2.5	MYL2.5	MYL2	MYL2 Price PP
Bottom Friction	Quadratic	Quadratic	Quadratic or Linear	Quadratic or Linear
Wetting/Drying	No	Yes	No	No
Temporal Scheme for Barotropic Equations				
Surface Gradient	Centered	Fully Implicit	Trapezoidal	Centered
Transport Gradient	Centered	Fully Implicit	Trapezoidal	Centered
Temporal Scheme for Baroclinic Equations				
Pressured Gradient	Centered	Forward	Centered	Adams-Bashforth
Coriolis Term	Centered	Forward	Centered	Adams-Bashforth
Horizontal Advection	Centered	Forward	Centered	Adams-Bashforth
Horizontal Mixing	Forward	Forward	Forward	Adams-Bashforth
Vertical Advection	Centered	Forward	Centered	Crank-Nicolson
Vertical Mixing	Fully Implicit	Fully Implicit	Fully Implicit	Crank-Nicolson

$$\frac{\partial \zeta}{\partial t} = -\frac{\partial((\zeta + H)\overline{u})}{\partial x} - \frac{\partial((\zeta + H)\overline{v})}{\partial y}, \tag{5}$$

$$\frac{\partial T}{\partial t} = -\nabla \cdot (\mathbf{v}T) + \nabla_h (A_H \nabla_h T) + \frac{\partial}{\partial z}(K_H \frac{\partial T}{\partial z}) + Q_r \frac{\partial \gamma}{\partial z}, \tag{6}$$

$$\frac{\partial S}{\partial t} = -\nabla \cdot (\mathbf{v}S) + \nabla_h (A_H \nabla_h S) + \frac{\partial}{\partial z}(K_H \frac{\partial S}{\partial z}), \tag{7}$$

$$\rho = \rho(T, S, z), \tag{8}$$

where t is the time, x, y, and z are the three coordinate directions, u, v, and w are the three components of the vector velocity $\mathbf{v}$, T is the potential temperature, S is the salinity, ∇_h is the horizontal gradient operator, f is the Coriolis parameter, p is the pressure, ρ is the water density,

ρ_o is a reference density, g is the acceleration of gravity, F_u and F_v are horizontal mixing terms for momentum, A_H is the horizontal mixing coefficient for scalar fields (temperature and salinity), K_M and K_H are vertical eddy coefficients for the momentum and scalar fields, respectively, Q_r is the solar radiation, γ is a function describing the solar extinction, ζ is the elevation of the free surface above the undisturbed value at $z = 0$, H is the bottom depth, and $\overline{u}$ and $\overline{v}$ are the depth-averaged horizontal velocities.

With the hydrostatic assumption, vertical accelerations are assumed to be small and the vertical momentum equation (3) is taken to be a balance between the vertical pressure gradient and the gravitational force. Vertical velocity is computed from the divergence of the horizontal flow field using the continuity equation (4).

With the Boussinesq approximation, density variations are only taken into account in calculating the horizontal pressure gradient terms and in calculating vertical stability for the parameterization of vertical mixing.

All the models use some version of the nonlinear equation of state for seawater to calculate density (8) from T and S. ECOM-si, SZM, and SCRUM calculate potential density, i.e., the density at atmospheric pressure. POM calculates the in situ density, which includes the effect of pressure, to provide more accurate density gradients in deep water. Note that the in situ density must be corrected for the effect of pressure when calculating vertical stability (which POM does).

2.2 Surface and Bottom Boundary Conditions

Equations (1)–(8) are subject to boundary conditions in the form of fluxes and stresses at the ocean's surface and bottom. The boundary conditions at the surface, which are due to fluxes between the ocean and the atmosphere, are

$$K_M \frac{\partial u}{\partial z} = \frac{\tau^x}{\rho_o}, \tag{9}$$

$$K_M \frac{\partial v}{\partial z} = \frac{\tau^y}{\rho_o}, \tag{10}$$

$$K_H \frac{\partial T}{\partial z} = \frac{Q_b + Q_e + Q_s}{\rho_o c_p}, \tag{11}$$

$$K_H \frac{\partial S}{\partial z} = S\big|_{z=0} (E_v - P_r), \tag{12}$$

where τ^x and τ^y are the x and y components of the surface wind stress, Q_b, Q_e, and Q_s are the net long-wave, latent, and sensible surface heat fluxes, E_v and P_r are the surface evaporation and precipitation rates, and c_p is the specific heat of seawater. At the ocean bottom, the boundary conditions are

$$K_M \frac{\partial u}{\partial z} = \frac{\tau_b^x}{\rho_o}, \tag{13}$$

$$K_M \frac{\partial v}{\partial z} = \frac{\tau_b^y}{\rho_o}, \tag{14}$$

$$K_H \frac{\partial T}{\partial z} = 0, \tag{15}$$

$$K_H \frac{\partial S}{\partial z} = 0, \tag{16}$$

where τ_b^x and τ_b^y are the x and y components of the bottom stress. The bottom stress is parameterized either by a linear drag law

$$\tau_b^x = -\rho_o c_{b_1} u, \tag{17}$$

$$\tau_b^y = -\rho_o c_{b_1} v, \tag{18}$$

where c_{b_1} is a linear drag coefficient with units of velocity, or a quadratic law

$$\tau_b^x = -\rho_o c_b u |\mathbf{v}|, \tag{19}$$

$$\tau_b^y = -\rho_o c_b v |\mathbf{v}|, \tag{20}$$

where c_b is a dimensionless coefficient.

The models generally use a quadratic bottom drag law with the drag coefficient computed in terms of the bottom-layer thickness Δz_b and the bottom roughness z_o as

$$c_b = \max\left[\frac{\kappa^2}{\log^2\left(\frac{\Delta z_b}{2z_o}\right)}, c_{b_{\min}}\right], \tag{21}$$

where $\kappa = 0.4$ is von Karman's constant and $c_{b_{\min}}$ is a minimum value for c_b. This expression for c_b is derived by combining (19–20) with the equation for a logarithmic boundary layer velocity profile

$$u = \frac{1}{\kappa}\left(\frac{\tau_b}{\rho_o}\right)^{\frac{1}{2}} \log\left(\frac{z}{z_o}\right), \tag{22}$$

where z is the distance above the bottom.

2.3 Horizontal Coordinate

POM, ECOM-si, and SCRUM use general orthogonal, curvilinear, horizontal coordinates. SZM is written to use only Cartesian coordinates and requires the use of a constant horizontal grid spacing in x and y.

Curvilinear grids allow some flexibility in setting up the horizontal grid in terms of varying the horizontal resolution in different parts of the model domain and positioning the lateral boundaries, or alternatively, conforming to a particular map projection. There are, however, some limitations on the degree to which an orthogonal, curvilinear grid can be curved or the rate at which the grid resolution can be changed if truncation errors associated with the spatial changes in the grid are to be kept small (Crowder and Dalton 1971; Rivas 1972).

The implementation of orthogonal curvilinear coordinates in the models is primarily a matter of accounting for the changing size of the grid cells when computing fluxes between the cells and when computing the changes within a cell. Hence, the variables for the horizontal size of the grid cells, Δx and Δy, must be stored as two-dimensional (2-D) arrays rather than as constants. The only correction to the models' equations for the curvature of the horizontal grid is a correction to the advection term to account for conversion between u and v momentum for advection along curving grid coordinates. Note that the horizontal momentum diffusion terms should also, ideally, have a curvature correction. Since the models do not have such a correction, they implicitly assume that the diffusion error due to any curvature of the grid is small and can be neglected. None of the models account for changes in the grid-cell spacing when interpolating variables between the center and the interfaces of the grid cells, i.e., all the models use simple averages for these interpolations.

All of the tests in this report were conducted with Cartesian horizontal coordinates with Δx and Δy both constant. Hence, error that might arise from the particular implementation of curvilinear horizontal coordinates in the individual models was not addressed.

2.4 Vertical Coordinate

POM and ECOM-si use a sigma (σ) coordinate in the vertical in which the depths of the model layers are a fixed fraction of the total depth of the water column from the free surface to the bottom. The sigma vertical coordinate is expressed as

$$\sigma = \frac{(z-\zeta)}{(\zeta+H)}, \tag{23}$$

so that σ varies from 0 at the surface to –1 at the bottom. With sigma coordinates, the layers near the bottom follow the contours of the bottom.

SZM uses sigma coordinates for a user-specified number of upper layers and uses z-levels for the layers below. SZM can be run with all sigma layers, with sigma layers in shallow water and z-levels in deep water, or with all z-levels (except for the upper layer, which, because of the free surface, must be a sigma layer). All the models allow stretching of the vertical grid, i.e., changes in $\Delta\sigma$ or Δz with depth, to provide different vertical resolution over different parts of the water column.

SCRUM uses what Song and Haidvogel (1994) call an "S" vertical coordinate. This vertical coordinate allows changing the fractional size of the individual sigma layers ($\Delta\sigma = \Delta z/(\zeta + H)$) in different parts of the domain as the depth of the bottom changes, rather than keeping $\Delta\sigma$ for a particular layer constant everywhere, as is the case with the usual implementation of sigma layers used in POM, ECOM-si, and SZM. For example, a minimum thickness can be specified for layers near the surface and bottom to avoid the normal vertical spreading of the sigma layers as the depth of the water increases.

Similar to orthogonal, curvilinear coordinates, the implementation of sigma or "S" coordinates in the models is primarily a matter of accounting for the changing vertical thickness of the layers in calculating fluxes between adjacent grid cells and in calculating changes within the grid cells. Note that with sigma coordinates, the changes in the thickness of the grid cells occurs not only horizontally within a layer, but also from timestep to timestep because of the changing surface elevation. To avoid having to use a large number of 3-D arrays to store the thickness of the grid cells at different locations and time levels, the models express the grid thickness Δz as the product of the fractional thickness of the sigma layer $\Delta\sigma$ times the total depth, i.e., as

$$\Delta z = \Delta\sigma\,(\zeta + H)\,. \tag{24}$$

The only correction to the equations used in the models for the changing depth of the sigma layers is a correction for the horizontal pressure gradient. The horizontal pressure gradient in sigma coordinates contains an extra term to calculate and remove the vertical change in pressure between neighboring points within a sigma layer so that the net pressure change that is computed will be approximately along a level surface (Blumberg and Mellor 1987).

A problem with this calculation of the pressure gradient with sigma coordinates is that the vertical component of the pressure change along a sloping sigma surface is frequently much larger than the horizontal component (Haney 1991). In this case, the desired horizontal component is calculated as the small difference between two large terms and is subject to significant truncation error. An expedient that is employed in the models to reduce this error is to subtract the horizontally averaged density profile from the 3-D density field when calculating the horizontal pressure gradient so that the main component of the vertical change in pressure is removed from the calculation.

Strictly speaking, for a full transformation of the equations to sigma coordinates, the horizontal diffusion terms would also be corrected for the transformation so that they would still represent diffusion along level surfaces. However, all the models use the approximation discussed by Mellor and Blumberg (1985) who argued that diffusion along the sigma surfaces rather than along level surfaces was, in general, more appropriate for sigma coordinate models, particularly for proper simulation of the bottom boundary layer with sigma coordinates. A practical reason for having "horizontal" diffusion occur along the sigma surfaces is that the rather messy form of the transformed horizontal diffusion terms is avoided.

2.5 Spatial Finite Differences

All the models use standard, second-order, centered spatial interpolations and FDs except that SCRUM uses linear FEs in the vertical. With second-order, centered interpolations and differences, the value of a variable ϕ at a location x is evaluated as the average of the values defined on either side, i.e.,

$$\phi|_x = \frac{1}{2}\left(\phi_{x+\frac{1}{2}\Delta x} + \phi_{x-\frac{1}{2}\Delta x}\right), \tag{25}$$

and the gradient of ϕ at x is calculated as

$$\frac{\partial \phi}{\partial x}|_x = \frac{1}{\Delta x}\left(\phi_{x+\frac{1}{2}\Delta x} - \phi_{x-\frac{1}{2}\Delta x}\right), \tag{26}$$

where Δx is the grid spacing.

2.6 Temporal Scheme for Baroclinic Equations

The temporal schemes that are used for the 3-D baroclinic equations of the models are discussed in this section. The temporal schemes are illustrated with just the u momentum equation, since the treatment of the other model variables is similar. In the following discussion, (n) will denote model values at the current time level (i.e., values calculated on the previous timestep), $(n+1)$ will denote the newly calculated values, and $(n-1)$ and $(n-2)$ will denote values at previous time levels. Note that, for simplicity, the temporal differencing equations that are presented here do not include the temporal changes in the vertical thickness of the layers on the models' sigma-coordinate grids (and on SCRUM's S-coordinate grid) caused by changes in the surface elevation (though these changes are accounted for by the models).

POM and SZM use a standard, leapfrog time-stepping scheme. With this scheme, most of the terms, i.e., the advection, baroclinic pressure gradient, and Coriolis terms, are centered in time at (n). The horizontal diffusion terms are calculated at the previous $(n-1)$ time level (since diffusion terms evaluated at the central time level of a leapfrog scheme tend to excite time splitting and cause numerical instability), and the vertical diffusion terms are treated implicitly so as to avoid the timestep restriction for explicit vertical diffusion (the high rates of vertical diffusion sometimes calculated by the turbulence submodels would require a very small timestep for stability if the vertical diffusion were explicit). Hence, the temporal differencing of the u momentum equation can be represented as

$$\frac{u^{(n+1)} - u^{(n-1)}}{2\Delta t} = -\nabla \cdot (\mathbf{v}u)^{(n)} + fv^{(n)} - \frac{1}{\rho_o}\frac{\partial p^{(n)}}{\partial x} + F_u^{(n-1)} + \frac{\partial}{\partial z}\left(K_M \frac{\partial u^{(n+1)}}{\partial z}\right). \tag{27}$$

POM and SZM use an Asselin filter to suppress the time splitting that can occur with leapfrog (Asselin 1972). The Asselin filter is applied at the end of each timestep to the fields at time level (n) by averaging in a bit of the values at the $(n+1)$ and $(n-1)$ time levels, i.e.,

$$\phi^{(n)} = \nu(\phi^{(n+1)} + \phi^{(n-1)}) + (1 - 2\nu)\phi^{(n)}, \tag{28}$$

where ν is the filter coefficient. If (28) is rewritten as

$$\phi^{(n)} = \phi^{(n)} + \nu(\phi^{(n+1)} - 2\phi^{(n)} + \phi^{(n-1)}), \tag{29}$$

the filter looks like a numerical diffusion term, which is the way that it behaves. A typical value of ν used in POM and SZM is 0.05, and this is the value used in the tests in this report.

ECOM-si uses a two-time-level scheme in which most of the terms in the baroclinic equations are evaluated at the current (n) time level. This is sometimes referred to as a forward time-differencing scheme. Vertical diffusion, however, is treated fully implicitly as in POM and SZM. The temporal differencing of the u momentum equation for ECOM-si can be written as

$$\frac{u^{(n+1)}-u^{(n)}}{\Delta t}=-\nabla\cdot(\mathbf{v}u)^{(n)}+fv^{(n)}-\frac{1}{\rho_o}\frac{\partial p^{(n)}}{\partial x}+F_u^{(n)}+\frac{\partial}{\partial z}\left(K_M\frac{\partial u^{(n+1)}}{\partial z}\right). \tag{30}$$

Note that ECOM-si updates the velocities before updating T and S and uses the new velocities to advect T and S so that in the T and S equations, the advection velocity $\mathbf{v}$ is at $(n+1)$ rather than at (n) as in the momentum equations.

There are some advantages to the forward scheme: (a) prognostic variables only need to be saved at a single time level, which saves computer storage, (b) there is no time-splitting problem that one must deal with as there is when using the leapfrog scheme, and (c) timestep restrictions are calculated for a timestep Δt, instead of with $2\Delta t$, which is the effective timestep for the leapfrog scheme. The big disadvantage of the forward scheme is that the terms are not centered in time and can suffer significant temporal truncation error. The magnitude of this truncation error depends on the ratio of the model timestep to the timescale of the physical process being simulated. The advection terms for the forward scheme require a certain amount of diffusion to suppress numerical dispersion and can become very dispersive when $\Delta t u^2/(2A_*) > 1$ (Clancy 1981), where A_* is the horizontal diffusion coefficient. This is discussed further in the tests of the advection schemes in Sec. 3.0.

SCRUM calculates the temporal derivatives for the baroclinic equations using the difference between successive time levels, i.e., the value at $(n+1)$ minus the value at (n), as does ECOM-si. However, SCRUM uses a third-order Adams Bashforth (AB3) scheme for the baroclinic pressure gradient, horizontal advection, and Coriolis terms. This scheme provides third-order temporal accuracy by using a quadratic extrapolation of the values at the three previous time levels to the value at $(n+\frac{1}{2})$, so that the calculated value is centered with respect to the time derivative. A Crank-Nicolson scheme is used for vertical advection and vertical diffusion, where half the term is evaluated at $(n+1)$ and half at (n). The temporal differencing of the u-momentum equation for SCRUM can be written as

$$\frac{u^{(n+1)}-u^{(n)}}{\Delta t}=-(\mathbf{v}_\mathbf{h}\cdot\nabla_h)u^{(a)}-w\frac{\partial u^{(c)}}{\partial z}+fv^{(a)}-\frac{1}{\rho_o}\frac{\partial p^{(a)}}{\partial x}+F_u^{(a)}+\frac{\partial}{\partial z}\left(K_M\frac{\partial u^{(c)}}{\partial z}\right), \tag{31}$$

where the superscript (a) refers to the AB3 scheme where

$$u^{(a)}=\frac{23}{12}u^{(n)}-\frac{16}{12}u^{(n-1)}+\frac{5}{12}u^{(n-2)}, \tag{32}$$

and (c) refers to the Crank-Nicolson scheme where

$$u^{(c)}=\frac{1}{2}\left(u^{(n)}+u^{(n+1)}\right). \tag{33}$$

ECOM-si's forward treatment of the Coriolis term is numerically unstable in that inertial oscillations grow exponentially with an e-folding timescale of $2/(\Delta t f^2)$. If the timestep used in ECOM-si is small, say less than about 200 s, which is generally the case for high-resolution coastal simulations, the timescale for the growth of the inertial oscillations is fairly slow, i.e., more than 10 d. Such a slow growth of inertial motions may be masked by other variability in the model or cancelled by the natural damping of the inertial motions due to friction and dispersion. For larger timesteps, however, the growth of the inertial motions can be a significant problem, e.g., for $\Delta t = 1200$ s, the timescale is 3.6 d at 30° N. For the purpose of conducting this study, which involved performing some simulations on fairly coarse grids, the Coriolis terms in ECOM-si were converted to a second-order Adams-Bashforth (AB2) treatment. For the u equation, this is given by

$$\frac{u^{(n+1)} - u^{(n)}}{\Delta t} = \frac{3}{2} f v^{(n)} - \frac{1}{2} f v^{(n-1)} + \ldots . \tag{34}$$

The AB2 scheme provides a linear extrapolation of the Coriolis terms to $(n + \frac{1}{2})$ so that they are centered in time with respect to the time derivative. With this treatment of the Coriolis terms, the amplification of inertial oscillations is neutral, i.e., there is no significant growth or damping. From the computational point of view, the cost of the AB2 treatment of the Coriolis terms is very small. This modification to ECOM-si was used for all the tests conducted in this report and no drawbacks to this change were observed. In several tests, comparison with the original treatment of the Coriolis terms verified the improvement in stability and accuracy with the AB2 treatment. Comparison of the AB2 scheme with an AB3 scheme for the Coriolis terms in some of the tests showed similar results for these two schemes.

2.7 Numerical Treatment of the Free Surface Mode

A limitation of most explicit numerical schemes is that signals cannot propagate more than a single grid interval in a single timestep, i.e., the timestep is restricted by

$$\Delta t < \frac{\Delta x}{c}, \tag{35}$$

where c is the speed of the signal (for leapfrog schemes, the timestep is effectively $2\Delta t$ so the restriction is $\Delta t < \Delta x/(2c)$).

Surface gravity waves travel very quickly, e.g., in water of 100-m depth, the speed of surface gravity waves is $(gH)^{\frac{1}{2}} = 32$ m/s. For a grid spacing of $\Delta x = 1$ km, explicit treatment of these waves in an ocean model requires a timestep of less than 30 s. If the surface gravity waves are excluded, the timestep is limited by the propagation of internal waves and advection velocities. Since these speeds are generally less than about 2 m/s, the timestep limitation for internal wave propagation and advection for the same 1-km grid would be about 500 s (250 s for a leapfrog scheme).

The timestep restriction for explicit treatment of the surface waves ranges from 10 to more than 50 times smaller than the timestep restriction for the other processes in the model, depending on the water depth, the maximum internal wave speed, and the maximum current velocities. Hence, the speed of surface gravity waves will severely limit the timestep of an ocean model unless a special numerical treatment is applied to these waves.

The models here use two approaches to avoid the timestep restriction of surface gravity waves. POM and SCRUM use the so-called "split-explicit" scheme, wherein the terms governing the propagation of the surface gravity waves are treated explicitly, but with a much smaller timestep than the rest of the model (Blumberg and Mellor 1987; Song and Haidvogel 1994; Killworth et al. 1991; Mellor 1996). With the split-explicit scheme, the 3-D momentum and continuity equations are vertically averaged to obtain the barotropic, 2-D momentum and continuity equations that govern the propagation of the surface gravity waves. The vertically averaged equations are solved explicitly with a sufficiently small timestep to avoid violating the timestep restriction for the surface gravity waves. After the new surface elevation and depth-averaged velocities have been solved by taking a number of small timesteps, the 3-D equations are solved with a much larger timestep governed by the timestep restriction for internal waves and/or advection. POM and SCRUM use leapfrog time differencing for the barotropic mode. POM uses an Asselin temporal filter to suppress time splitting of the barotropic equations and SCRUM uses a trapezoidal correction.

ECOM-si and SZM avoid the timestep restriction of the surface gravity waves by treating the primary terms governing the propagation of these waves implicitly. These are the surface pressure gradient terms in the momentum equations and the transport gradient terms in the depth-averaged continuity equation. In ECOM-si, these terms are treated fully implicitly, i.e., fully at the new time level. In SZM, the temporal weighting of these terms can be set by the user. For the tests conducted in this report, an equal weighting of these terms at the old $(n-1)$ and new $(n+1)$ time levels was used.

A disadvantage of the implicit scheme with respect to the split-explicit scheme for the surface gravity waves is that the implicit scheme has much less temporal accuracy since it is using a much larger timestep. The loss of accuracy is most severe at smaller wavelengths. An advantage of the implicit scheme is that it tends to be more computationally efficient, especially if part of the model domain is very deep, so that the timestep for the explicit treatment of the surface waves must be very small. Another advantage of the implicit scheme over the split-explicit scheme is that it is simpler to implement. The split-explicit scheme must be implemented carefully to eliminate inconsistencies between the depth-averaged equations and the rest of the model. Potential problems are discussed by Killworth et al. (1991), Dukowicz and Smith (1994), and Mellor (1996).

2.8 Parameterization of Advection

POM, ECOM-si, and SZM use the flux form of the advection terms, as written in (1), (2), (6), and (7). SCRUM uses the advective form in which the advection term for, e.g., temperature, is written as $\mathbf{v} \cdot \nabla T$ rather than $\nabla \cdot (\mathbf{v}T)$.

An advantage of implementing the advection terms in flux form is that the advected field can be conserved. However, to ensure strict conservation, it is essential that the numerical form of the time derivative and the advection terms for the field being advected be consistent with the numerical form of the continuity equation. A simple way to check for this in the models is to set the advected field to a constant. Then the time derivative and advection terms for the advected field must cancel numerically or there will be spurious sources and sinks of the advected field that will occur at grid cells in which the net advective volume flux into a grid cell and the change in volume of the grid cell do not match.

POM, ECOM-si, and SZM go to some trouble to ensure that the advection terms for T and S are consistent with the numerical form of the continuity equation. However, this is not quite the case for advection of momentum. To have fully conservative momentum advection would require

an iterative procedure, since the momentum advection terms are needed to calculate the new surface elevation and the new surface elevation is needed to calculate the momentum advection terms in a completely conservative manner. (Another smaller source of error in calculating momentum advection is that, with a curvilinear grid and grid-cell thicknesses that change with time, interpolation of nondivergent advective volume fluxes to the staggered momentum grid cells on a *C* grid will not result in exact nondivergence at the momentum grid cells.) SZM provides for such an iteration. However, use of this option, which adds considerably to the model's run time, does not generally have a significant effect on the model results. This provides some validation of the assumption made in these models that strict conservation of momentum is generally less critical to model accuracy than conservation of scalar fields because of the less dominant role of advection in the momentum equations.

With the advective form of the model equations used by SCRUM, strict numerical conservation of the advection field is not required to avoid spurious numerical effects. The disadvantage of the advective form is that the field being advected is not strictly conserved. Note that the strict conservation of scalar fields is desirable, but tends to be more of a concern for long time integrations than the typical short simulations usually conducted in coastal modeling, and also more of a concern for large ocean regions than for coastal areas where sources, sinks, and flows through open boundaries play a larger role. Of course, errors due to nonconservation of advected fields must remain sufficiently small so as not to significantly affect results.

2.9 Parameterization of Horizontal Mixing

POM, ECOM-si, and SZM use Laplacian horizontal mixing. POM and ECOM-si use the Smagorinsky (1963) parameterization in which the horizontal friction terms are written as

$$F_u = \frac{\partial}{\partial x}\left(2A_M \frac{\partial u}{\partial x}\right) + \frac{\partial}{\partial y}\left(A_M\left(\frac{\partial u}{\partial y} + \frac{\partial v}{\partial x}\right)\right), \tag{36}$$

$$F_v = \frac{\partial}{\partial y}\left(2A_M \frac{\partial v}{\partial y}\right) + \frac{\partial}{\partial x}\left(A_M\left(\frac{\partial u}{\partial y} + \frac{\partial v}{\partial x}\right)\right). \tag{37}$$

For the Smagorinsky mixing scheme, the horizontal mixing coefficient A_M is calculated as a function of the local horizontal grid resolution and velocity shear, i.e.,

$$A_M = C_s \Delta x \Delta y \left(\left(\frac{\partial u}{\partial x}\right)^2 + \frac{1}{2}\left(\frac{\partial v}{\partial x} + \frac{\partial u}{\partial y}\right)^2 + \left(\frac{\partial v}{\partial y}\right)^2\right)^{\frac{1}{2}}. \tag{38}$$

The magnitude of the Smagorinsky eddy coefficients is scaled by the constant C_s (called HORCON in the POM and ECOM-si model programs). Values used for C_s range from about 0.01 to 0.5. Large values of C_s tend to dissipate small features, whereas values that are too small can lead to numerical noise and/or instability. Typically, a value near 0.1 is used, and 0.1 is the value used for the tests conducted in this report.

The horizontal friction terms in SZM use the form

$$F_u = \frac{\partial}{\partial x}\left(A_M \frac{\partial u}{\partial x}\right) + \frac{\partial}{\partial y}\left(A_M \frac{\partial u}{\partial y}\right), \tag{39}$$

$$F_v = \frac{\partial}{\partial x}\left(A_M \frac{\partial v}{\partial x}\right) + \frac{\partial}{\partial y}\left(A_M \frac{\partial v}{\partial y}\right). \tag{40}$$

The horizontal mixing coefficient A_M in SZM is set equal to the maximum of a constant background value A_o and a value needed to keep the grid-cell Reynolds Number R_{e_g} below a maximum specified value, i.e.,

$$A_M = \max\left(A_o, \frac{u\Delta x}{R_{e_g}}\right). \tag{41}$$

The value of R_{e_g} is typically set to a value of 30–100 in the horizontal. Values in this range generally provide a good compromise between allowing natural dynamic instability processes to develop and keeping numerical noise to acceptable levels. In most of the tests conducted here, R_{e_g} is set to a value of 100 and $A_o = a_o\ \Delta x$, where $A_o = 0.1$ cm/s.

The form used for horizontal diffusion of T and S in POM, ECOM-si, and SZM is the Laplacian form expressed in (39) and (40). The models provide for allowing A_H to be some fraction of A_M, but are frequently run with $A_H = A_M$. A_H and A_M were set equal in the tests conducted here.

In regions where there are large changes in the bottom depth, the horizontal diffusion along sloping sigma layers can cause severe cross-isopycnal diffusion (Paul 1994). An expedient that is sometimes used with sigma coordinate models, which is employed in the models tested here, is to subtract a smooth, background field from the T or S fields when calculating horizontal diffusion. By calculating the horizontal diffusion based on the anomaly from a smooth background field, most of the component of vertical diffusion that occurs when diffusion is calculated along sloping sigma layers is eliminated. In the tests conducted here, the background T and S fields are calculated as the horizontally averaged T and S profiles. This is a commonly used procedure. An alternative strategy is to use smooth but horizontally varying background fields to accommodate changes in the structure of the T and S fields in different parts of the model domain. The background fields can also be periodically updated to accommodate changes in T and S that occur in time. We note that the use of these procedures can significantly reduce the problem of severe cross-isopycnal diffusion; however, they can introduce other problems, one example of which will be discussed in the upwelling/downwelling test in Sec. 8.0.

SCRUM offers both Laplacian horizontal friction (with constant values of A_M and A_H) and high-order, biharmonic friction in the horizontal. Biharmonic friction is more effective in removing small-scale noise than Laplacian friction, but is not strictly conservative.

2.10 Parameterization of Vertical Mixing

POM and ECOM-si use the MYL2.5 turbulence model to parameterize vertical mixing (Mellor and Yamada 1982; Blumberg and Mellor 1987). This turbulence model requires the prognostic

calculation of two turbulence quantities, q^2, which is twice the turbulent kinetic energy (TKE), and $q^2\ell$, where ℓ is the turbulent length scale.

SZM uses the MYL2 turbulence model (Mellor and Yamada 1974; Mellor and Durbin 1975). The MYL2 turbulence model assumes a local balance between shear production, buoyancy production, and dissipation of TKE, and does not require prognostic prediction of any turbulence quantities. This saves computer time and memory relative to using the MYL2.5 model; however, the simplified TKE equation does not account for storage and transport of TKE. The turbulence length scale ℓ for SZM is calculated diagnostically based on the distance from the top (z_t) and bottom (z_b) of a turbulent boundary layer, i.e.,

$$\ell = \kappa \left(z_t^{-1} + z_b^{-1} \right)^{-1}, \tag{42}$$

where $\kappa = 0.4$ is von Karman's constant. The simplification of the MYL2 scheme relative to the MYL2.5 scheme may have some disadvantages in terms of accuracy and robustness. Tests will be conducted to determine how the implementations of the MYL2 and MYL2.5 schemes in the models compare for some basic mixing situations.

2.11 Position of Variables on the Model Grid

The horizontal positioning of the main variables with respect to the grid cells is the same for all the models. They all use an Arakawa *C* grid in which the horizontal velocities are defined at the edges of the grid cells, and the other variables (T, S, p, ρ, w, ζ) are defined at the center of the grid cells (Fig. 1).

Looking at the vertical location of the variables for POM, ECOM-si, and SZM, all the main variables are defined at the center of a layer except for w, which is defined at the interface between the layers (Fig. 2a). For SCRUM, which uses a FE scheme in the vertical, all the main variables are defined at the layer interfaces (Fig. 2b). For POM and ECOM-si, the turbulence variables q^2 and $q^2\ell$ are defined at the w locations.

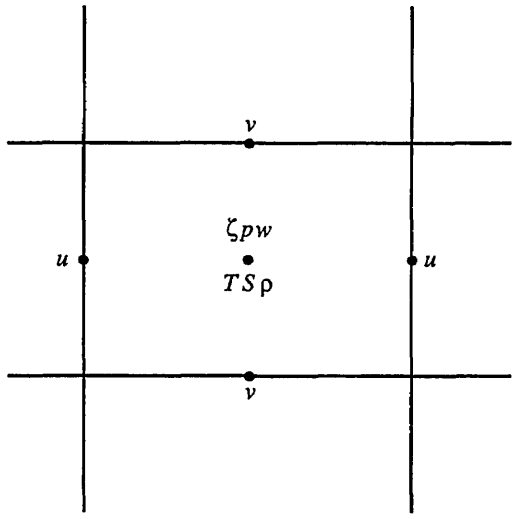

Fig. 1 — Horizontal arrangement of primary model variables on the numerical grid for all the models

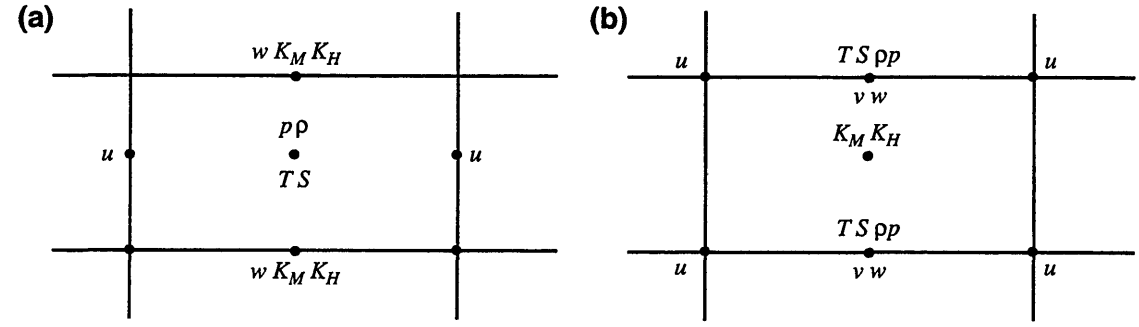

Fig. 2 — Vertical arrangement of primary model variables on the numerical grid for (a) POM, ECOM-si, and SZM and (b) SCRUM

The horizontal eddy coefficients for POM and ECOM-si are defined at the grid-cell centers. For SZM, separate horizontal eddy coefficients are calculated for diffusion in the x and y directions, and these are defined at the u and v locations, respectively. The vertical eddy coefficients for POM, ECOM-si, and SZM are defined at the w locations; however, for SCRUM they are defined at the center of the grid cells.

2.12 Setting Up the Models for Testing

POM, as obtained from Princeton University, was set up for a closed domain, and the do-loop limits used in the model were unsuitable for use with open boundaries. Hence, before beginning testing of POM, all the do-loops in the model were checked, and if necessary, modified to allow the use of open boundaries on all sides (note that the do-loop limits needed for open boundaries are not incompatible with the use of either closed or periodic boundaries).

This problem of the do-loop limits has been noted by many users of POM. In 1996, the version of POM available from Princeton was replaced with a new version in which the do-loop limits are reported to have been modified to more easily allow the use of open boundaries (this new version of POM has not yet been compared with our own modifications).

ECOM-si came with a fairly well-developed user interface that allows setting up a model run for a particular simulation by placing all the input parameters and data required for the run in two input data files. An advantage of this setup is that few (if any) changes need to be made to the model code to run a particular simulation. However, this setup proved to be cumbersome for the tests conducted here, and was replaced with a set of subroutines to define the model setup, initialization, and forcing.

The ability to use periodic lateral boundary conditions in both x and y was added to both POM and ECOM-si (this feature was already available for SZM and SCRUM). Periodic boundaries are not needed for simulations of actual coastal regions, but are very useful for testing purposes. Many of the tests conducted for this model comparison study used periodic boundaries in one or both directions.

As discussed in the introduction, there were a number of problems found with the Version 2.1 SCRUM code that was obtained from Rutgers. The Crank-Nicolson treatment of vertical mixing tended to produce noisy, inaccurate vertical mixing, and some terms were missing from the forcing

for the free surface mode. These problems were generally due to the fact that SCRUM was still undergoing changes. As previously stated, because of these problems and extensive changes that were made to SCRUM in the more recent version of the model that has been made available (Version 3.0), SCRUM was not included in most of the model tests.

3.0 TEST OF HORIZONTAL ADVECTION

3.1 Rotating Cone Advection Test

The performance of the horizontal advection schemes used in the models was investigated by performing the classic "rotating cone" advection experiment (Crowley 1968; Molenkamp 1968; Orszag 1971; Anderson and Gattahi 1974; Purnell 1976; Shannon 1979; Long and Pepper 1981; McRae et al. 1982; Smolarkiweicz and Grabowski 1990; Cantekin and Westerink 1990). In this experiment, a cone- or Gaussian-shaped feature is advected in a circular path by an advection field representing solid body rotation about the center of the domain. A perfect advection scheme would advect the feature in a circular path at the proper speed without changing its shape. The performance of the advection scheme is judged by the distortion of the shape of the feature after a certain period of advection and by errors in its position.

Figure 3a shows the model domain and the initial condition for this experiment. The model domain consists of a square region 40 km on a side. The grid spacing within the domain is a uniform 1 km. The initial feature, which is taken to be in the shape of a cone, is located 10 km south of the center of the model domain and has a radius at its base of 4 km (4 gridpoints) and a maximum amplitude of 50 units. The field being advected could be considered to be temperature, salinity, or some other constituent of the model. The advection field consists of solid body rotation about the center of the model domain with a period of rotation of 1.6 d. With this rotation period, the advection velocity at the location of the center of the cone is 45.4 cm/s.

Note that the advection tests were conducted with the numerical schemes used for advection in the models, but not with the models themselves. This was the only test in this report that was conducted in this manner. The advection test was conducted this way because it was simpler to do so than to set up this test with the models.

These advection experiments included a certain amount of explicit diffusion. This was necessary since some diffusion is needed to filter the numerical noise generated by the advection schemes. For the advection experiments, the diffusion terms were parameterized using standard, second-order, flux-conserving, Laplacian diffusion with a constant diffusion coefficient.

As discussed in the previous section, POM, ECOM-si, and SZM use the same second-order, centered, spatial finite difference scheme for the horizontal advection terms. With this scheme, the field being advected is interpolated from the grid-cell centers to the grid-cell boundaries using two-point averages, and the flux through the boundaries of the cell is computed by multiplying the value of the field at the grid-cell boundary by the normal velocity at the boundary. The change in the field due to advection is then calculated as the sum of the fluxes into and out of each of the grid cells. This scheme is conservative, since the flux leaving a cell is equal to the flux entering an adjoining cell though the common face.

SCRUM uses the advective form of the advection term in which the gradient of the field being advected is calculated at the grid-cell center using a two-point difference and is multiplied by the advection velocity averaged to the grid-cell center using a two-point average (since the advection

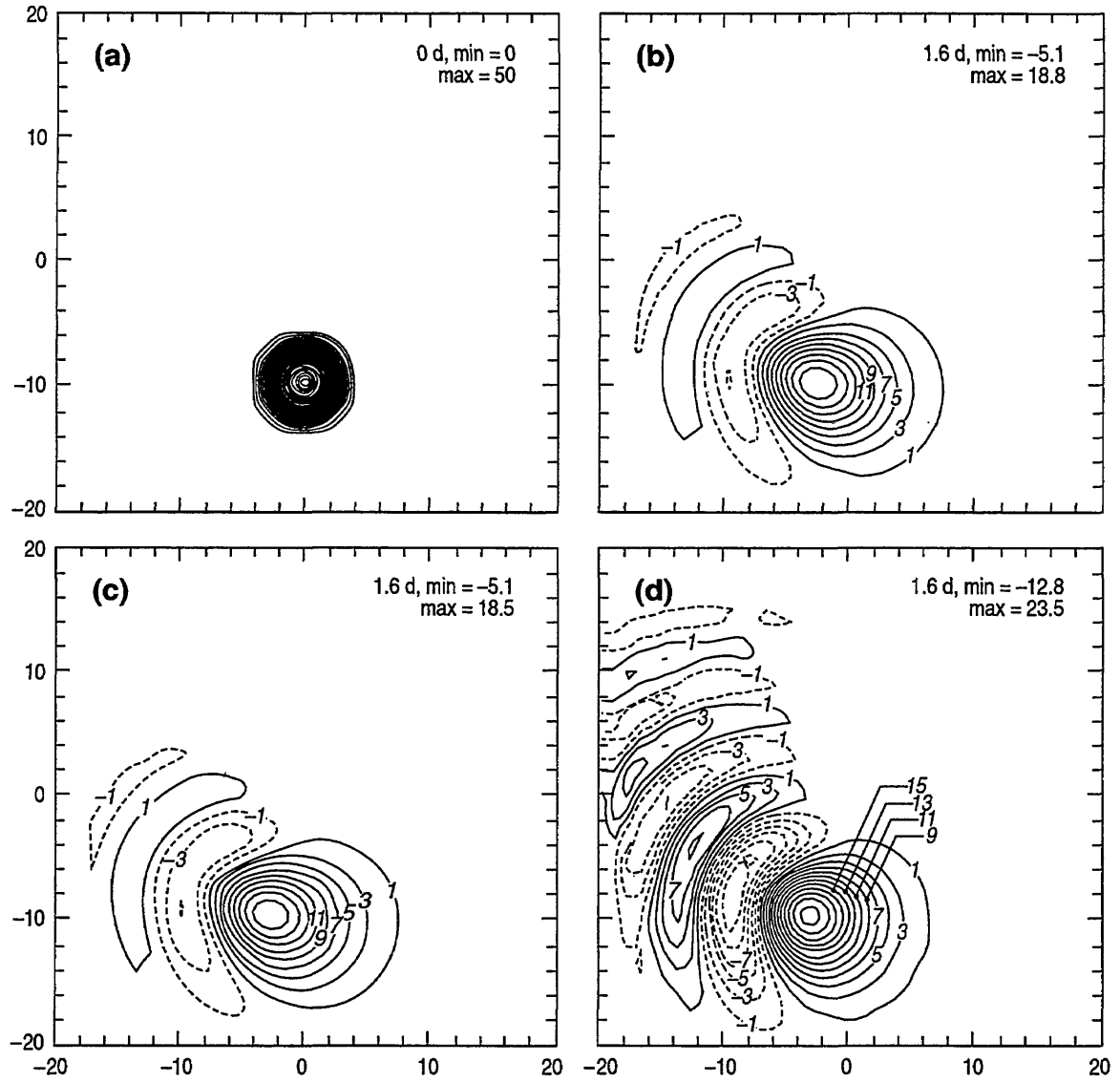

Fig. 3 — Results of rotating cone advection test after one revolution (1.6 d) for (b) leapfrog scheme used by POM and SZM, (c) AB3 scheme used by SCRUM, and (d) forward temporal scheme used by ECOM-si. The initial position and shape of the cone are shown in (a). The initial height of the cone is 50 units. The timestep was 360 s for the leapfrog and AB3 schemes and 180 s for the forward scheme. The horizontal viscosity was a constant 10 m^2/s. The gridpoint locations are denoted by the tick marks, and $\Delta x = 1$ km.

field is constant in time and varies gradually in space, the flux and advective forms of the advection term gave very similar results in this test).

The differences in the behavior of the advection schemes used by these models in this test are due mainly to the differences in the temporal differencing schemes. As discussed in Sec. 2.6, POM and SZM use a leapfrog temporal scheme in which the advection terms are calculated at the central time level, i.e, for the advection of the variable T, and ignoring other terms, we have

$$T^{(n+1)} = T^{(n-1)} + 2\Delta t C^{(n)}, \tag{43}$$

where $C^{(n)}$ denotes the advection term. The temporal accuracy of leapfrog advection is second order, i.e., the temporal truncation errors are proportional to $(\Delta t)^2$.

ECOM-si uses the two-time-level, forward temporal scheme in which the advection terms are evaluated at (n), i.e.,

$$T^{(n+1)} = T^{(n)} + \Delta t C^{(n)} . \tag{44}$$

The temporal accuracy of the forward scheme is only first order because the advection terms are not centered in time.

SCRUM updates the baroclinic fields from the values at (n) using the AB3 scheme

$$T^{(n+1)} = T^{(n)} + \Delta t((23C^{(n)} - 16C^{(n-1)} + 5C^{(n-2)})/12) , \tag{45}$$

for which the truncation error is proportional to $(\Delta t)^3$.

The standard timestep for the advection experiments was taken to be $\Delta t = 360$ s and the horizontal diffusivity A_H was set to a constant 10 m^2/s. A requirement for numerical stability of an explicit advection scheme is that

$$C_u = u\frac{\Delta t}{\Delta x} < 1 , \tag{46}$$

where C_u is the Courant Number. A similar stability requirement for explicit diffusion is given by the diffusion number d (Roache 1976).

$$d = 2A_H\frac{\Delta t}{\Delta x^2} < 1 . \tag{47}$$

For the leapfrog scheme, the value of Δt in (46) and (47) should be replaced by $2\Delta t$, since the timestep is effectively $2\Delta t$.

Also, as mentioned in Sec. 2.0, it is frequently desirable for the grid-cell Reynolds Number ($R_{e_g} = u\Delta x/A_H$), which is the ratio of the relative strengths of the advection and diffusion terms, to be in the range of 30–100 so that the natural physical instabilities of the flow on the smallest spatial scales resolvable by the model are not damped by the diffusion terms.

For the temporal differencing schemes used by ECOM-si and SCRUM, and for our standard parameter values ($\Delta t = 360$ s, $\Delta x = 1$ km, and $A_H = 10$ m^2/s), $C_u = 0.16$, $d = 0.0072$, and $R_{e_g} = 45$ at the location of the center of the cone where $u = 45.4$ cm/s. In the corners of the model grid where $u = 128.5$ cm/s, $C_u = 0.46$ and $R_{e_g} = 127$. For the leapfrog scheme used by POM and SZM, the timestep is effectively 2×360 s in (46) and (47) so that values of C_u are twice as large, i.e., 0.33 at the location of the center of the cone and 0.93 in the corners. Hence, the schemes satisfy the stability constraints described by (46) and (47) over the entire grid for the standard parameter values.

For the forward advection scheme used by ECOM-si, there is another constraint (Clancy 1981), which is

$$\frac{\Delta t u^2}{A_H} < 2 . \tag{48}$$

Failure to comply with this restriction results in severe numerical dispersion and possible instability. Note that for the standard parameters values, $\Delta t u^2/A_H = 7.3$, i.e., (48) is not satisfied. Equation (48) could be satisfied by reducing the ratio $\Delta t/A_H$ by a factor of about 4.

Figure 3 shows the initial shape of the cone and the results for the advection of the cone after one complete revolution (1.6 d) for each of the three advection schemes: the leapfrog advection scheme used by POM and SZM, the AB3 scheme used by SCRUM, and the forward scheme used by ECOM-si. Results from all the advection experiments are also summarized in Table 2. The forward advection scheme was unstable with $\Delta t = 360$ s and $A_H = 10$ m^2/s, so the timestep was reduced by half, i.e., the results for the forward scheme in Fig. 3 are for $\Delta t = 180$ s.

The results for the leapfrog and AB3 schemes in Fig. 3 are about the same. The peak of the cone is reduced from 50 to 19 units due to a combination of dispersion caused by the numerical scheme (i.e., failure of the scheme to advect the field at the true advection velocity), and actual diffusion by the diffusion term (the diffusion term alone would have reduced the peak from 50 to 25 units in 1.6 d). Numerical dispersion creates a wake behind the cone that has a maximum value of –5 units in the first wave behind the cone. Dispersion is also responsible for the fact that the peak of the cone does not quite get back to its initial position, but falls short by about 3 km.

Figure 4 shows results for the leapfrog and AB3 schemes for the same experiment, but with A_H reduced from 10 to 5 m^2/s. This decrease in A_H gives $R_{e_g} = 90$ at the location of the cone. The leapfrog and AB3 schemes again give similar results. With the reduced diffusivity, the maximum

Table 2 — Results from Cone Experiment with Advection Schemes Used by Ocean Models

SCHEME	Δt (s)	DIFFUSIVITY (m^2/s)	MAX AMPLITUDE WITHIN CONE	MAX AMPLITUDE WITHIN WAKE	PHASE ERROR (km)
Leapfrog	360	10	19	–5	3
Leapfrog	360	5	22	–8	3
Leapfrog	90	5	22	–8	3
AB3	360	10	19	–5	3
AB3	360	5	22	–7	3
AB3	90	5	22	–8	3
Forward	180	10	24	–13	3
Forward	90	10	21	–8	3
Forward	45	10	20	–6	3
Forward	30	10	19	–6	3
Forward	20	10	19	–6	3
Forward	180	20	18	–7	3

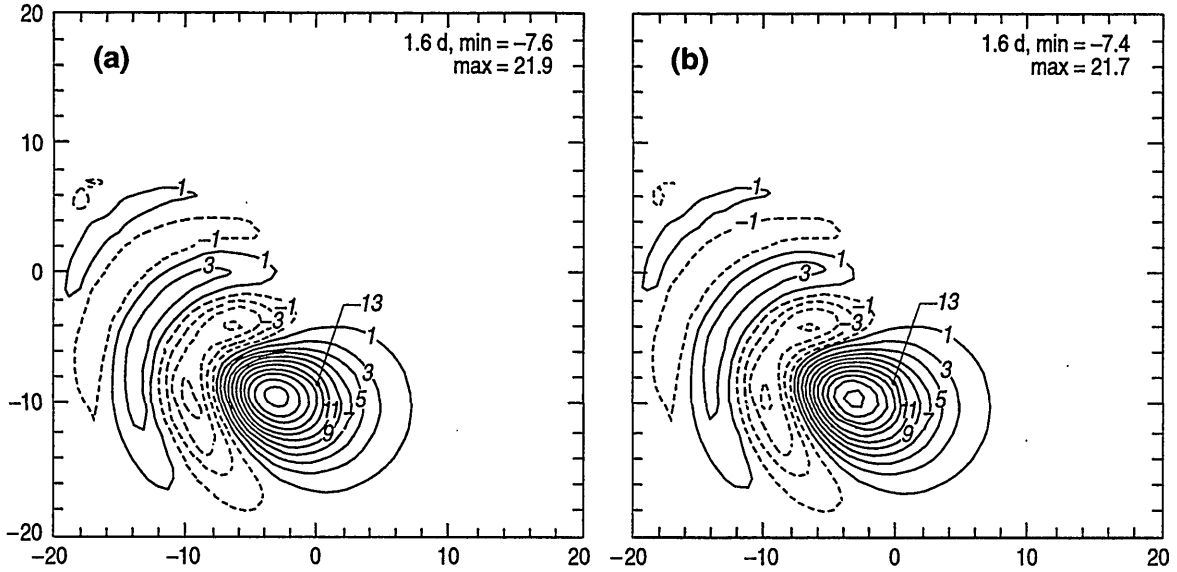

Fig. 4 — Results of rotating cone advection test after one revolution (1.6 d) for (a) leapfrog and (b) AB3 schemes with a constant horizontal viscosity of 5 m^2/s

amplitude within the cone is increased from 19 to 22 units, but the amplitude of the wake, caused by numerical dispersion, is also increased. Reducing the timestep with these two schemes did not significantly affect the results (Table 2), i.e., the error is primarily due to spatial, rather than temporal, truncation error.

The forward-in-time advection scheme is well known to be highly dispersive (Roache 1976) and the results with this scheme in Fig. 3 show much greater dispersion than with the leapfrog and AB3 schemes, in spite of the fact that a smaller timestep is used. The maximum value in the wake behind the cone after one revolution is –13 units, compared with –5 units for the leapfrog and AB3 schemes.

Figure 5a–c shows results for the forward scheme with timesteps of 90, 45, and 20 s (with $A_H = 10$ m^2/s). The values of C_u at the center of the cone for these experiments are 0.04, 0.02, and 0.01, i.e., well below the value of 1.0 required for stability with the leapfrog and AB3 schemes. Because of the large temporal truncation error of the forward scheme, the dispersion is significantly reduced as the timestep is reduced. The results with $\Delta t = 45$ s are similar to the results with the other two schemes. Further reduction of the timestep below 20 s does not improve the results, indicating that the remaining error is primarily due to spatial truncation error.

Increasing the diffusivity can also reduce the dispersion of the forward advection scheme. Figure 5d shows a result with $\Delta t = 180$ s as was used for the result in Fig. 3d, but with A_H increased to from 10 to 20 m^2/s. Note that with this larger value of A_H, the forward scheme satisfies the criteria expressed in (48). Figure 5d illustrates that increasing the diffusivity can reduce the numerical dispersion, though at the cost of increasing the diffusiveness of the numerical scheme.

In summary, the advection schemes used by POM, SZM, and SCRUM give similar results in these tests. The numerical dispersion of these schemes is certainly significant. However, based on the wide use of these advection schemes in ocean modeling, this degree of dispersion has been deemed to be tolerable (in recent years, ocean modelers have been increasingly investigating the

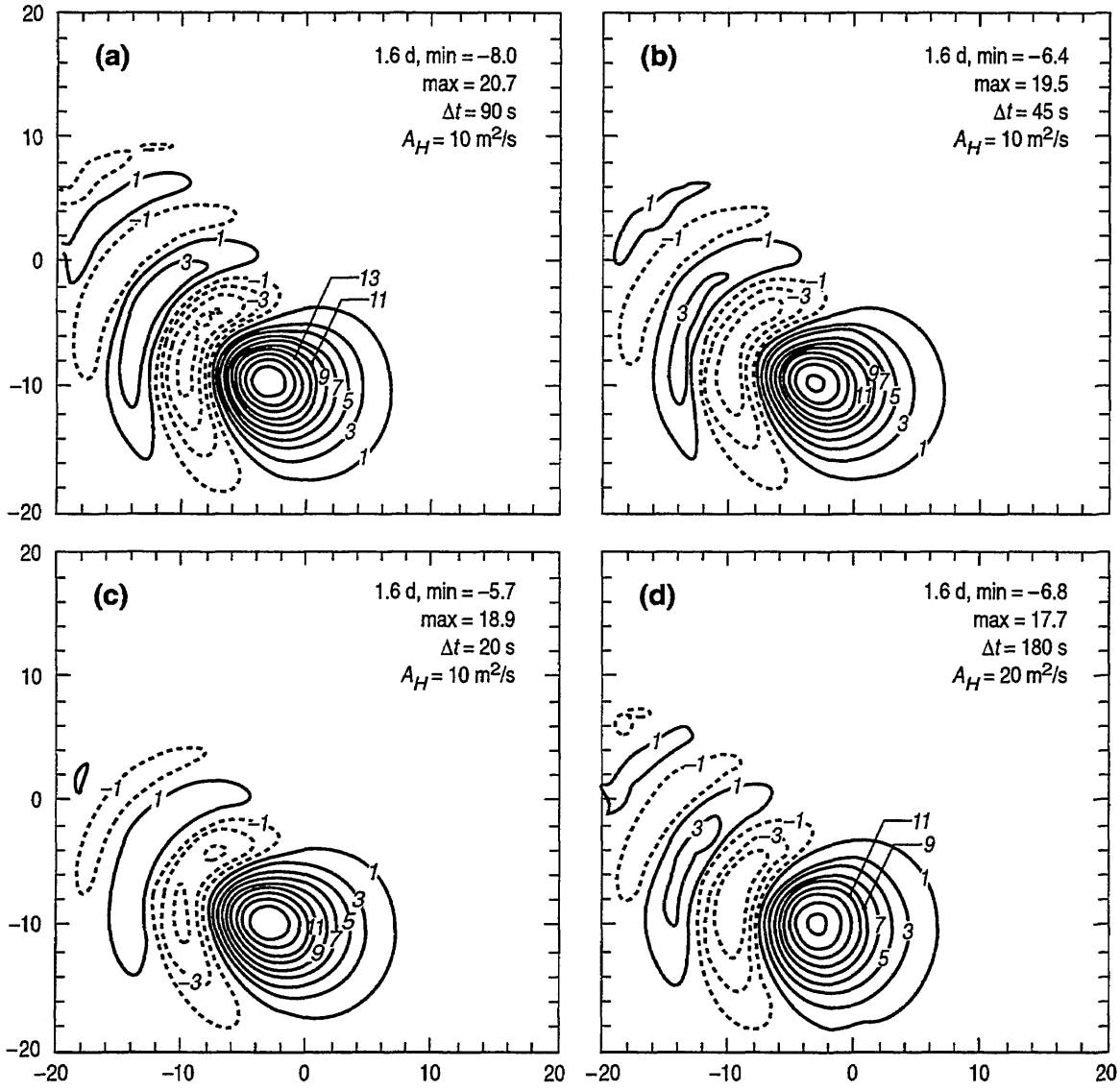

Fig. 5 — Results of rotating cone advection test after one revolution (1.6 d) with forward temporal scheme for different timestep and viscosity values

use of alternative advection schemes (Hecht et al. 1995)). The error of the advection schemes used in POM, SZM, and SCRUM is mostly due to spatial truncation error and the results are not very sensitive to the timestep as long as the timestep is small enough to keep C_u below the value required for numerical stability.

The forward advection scheme used by ECOM-si is well known to be highly dispersive. Unlike the leapfrog and AB3 schemes, the forward scheme is very sensitive to the timestep because of the significant temporal truncation error. As C_u is increased above a value of about 0.04, the dispersion of the forward scheme increases markedly. This dispersion can be reduced and numerical stability maintained by increasing the diffusivity or viscosity so that $\Delta t u^2/A_H$ remains below a value of about two. However, as the value of C_u increases above about 0.04, the values of A_H required to satisfy this criteria will result in increasingly diffusive flows.

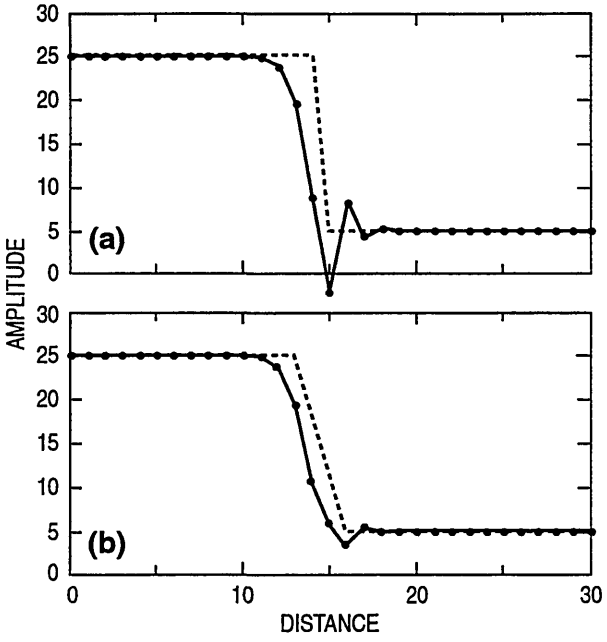

Fig. 6 — Results of advective overshoot experiment with second-order, centered advection scheme. The dashed line shows the initial temperature and the solid line shows the predicted temperature at the time of maximum overshoot. In (a), the initial temperature jump occurs between two gridpoints and in (b) it is distributed (linearly) over four gridpoints. The gridpoint locations are indicated by tick marks along the distance axis and also by dots at the predicted temperature values.

3.2 Advective Overshoot with Second-Order, Centered Advection Scheme

The second-order, centered advection scheme used in all the models being compared here is subject to an error sometimes referred to as "advective overshoot," when spatial changes in the field being advected are not adequately resolved. Figure 6 shows the results of the uniform advection of a field in which there is a sharp change (i.e., a sharp front) occurring between gridpoints. The field being advected could be any model variable. In this case, the advected variable is taken to be temperature.

In the case shown in Fig. 6, the grid spacing is 1 km, the timestep is 200 s, and the advection velocity is a constant 10 cm/s in a direction from right to left. The value of the horizontal diffusivity has been taken be to a constant 1 m^2/s to give a grid-cell Reynolds number of 100. The dashed line in the figure shows the initial value of the advected field and the solid line shows the field after 70 timesteps. In Fig. 6a, it can be seen that the value at the gridpoint on the upstream side of the front has decreased by about 7°C after 70 timesteps.

The reason for the temperature drop on the upstream side of the front is illustrated in Fig. 7. With the second-order, centered advection scheme, the value of the field advected through the face of a grid cell is the mean value of the field in the adjoining grid cells. Hence, the value of the temperature being advected out of the cold grid cell on the upstream side of the front in Fig. 7 is higher than the value being advected in on the other side, and the value within the grid-cell drops. For a jump in the advected field that occurs completely between two grid cells, the maximum drop at the upstream grid cell is about 1/3 the value of the initial jump. The size of this drop is not significantly affected by the timestep or the magnitude of the velocity. Nor is the size of the drop much affected by the horizontal diffusivity, as long as the diffusivity is sufficiently small that the grid-cell Reynolds number is fairly high (which is generally the case in these models to avoid excessive diffusion), e.g., if the horizontal diffusivity is increased by a factor of 10 to reduce the grid-cell Reynolds number to 10 (a fairly small value for an ocean model), the drop in the temperature at the gridpoint upstream of the front is still about 5°C. The results of several experiments in which the values of the parameters in this experiment were varied are summarized in Table 3.

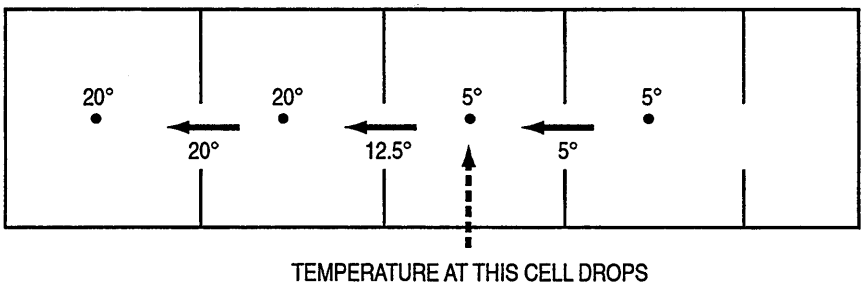

Fig. 7 — Schematic showing advection between grid cells at the location of a sharp front. The temperature flux at the interface between the grid cells is calculated based on the mean temperature of the adjoining cells. The temperature at the cold grid cell on the upwind side of the front drops because the advective flux leaving the cell is much warmer than the advective flux entering the cell.

Table 3 — Results of Experiments Conducted to Investigate Advective Overshoot at a Front with a Second-Order, Centered Advection Scheme. The Initial (20°C) Change in the Temperature Field Occurs Completely Between Two Grid Cells. The Temperature Drop Reported in the Table is the Maximum Temperature Drop that Occurs at the Cold Grid Cell on the Upstream Side of the Front.

GRID SPACING (km)	TIMESTEP (s)	VELOCITY (cm/s)	DIFFUSIVITY (m^2/s)	CELL RE	MAX TEMPERATURE DROP (°C)
1	200	100	10.0	100	7.2
1	200	10	1.0	100	7.2
1	200	1	0.1	100	7.2
1	200	10	10.0	10	4.9
1	20	10	1.0	100	7.2

The magnitude of the advective overshoot can be reduced by increasing the resolution of the front. Figure 6b shows the result of resolving the initial front by four gridpoints instead of two. The magnitude of the overshoot is reduced from 7.2 to 1.7°C.

Sharp temperature or salinity fronts between adjacent gridpoints can occur in model simulations with sigma coordinates when there is a sudden change in depth such that horizontally adjacent gridpoints in the bottom layers lie on different sides of a strong thermocline or halocline. Such a situation is illustrated in Fig. 8. In this case, in the bottom layer of the model, a grid cell in shallow water on the shelf is adjacent to a grid cell in much deeper water off the shelf at which the temperature is 20°C colder. If there is advection from the cold grid cell to the warm cell, the temperature within the cold cell will drop as illustrated in Fig. 6a. Such a situation occurred in simulations of the Gulf of Mexico circulation with POM and SZM (Martin 1998). The resulting advective overshoot caused the bottom-layer temperature in the area of the steep continental slope south of Cuba to become negative and the model simulations became unstable. The solution in these cases is to increase the horizontal resolution of steep bottom slopes, either by increasing the horizontal grid resolution or by reducing the slope itself, so that gradients in the model fields are better resolved. Note that this particular problem does not occur with z-level vertical coordinates, since the gradient between the near surface and deep water will be resolved by several vertical levels.

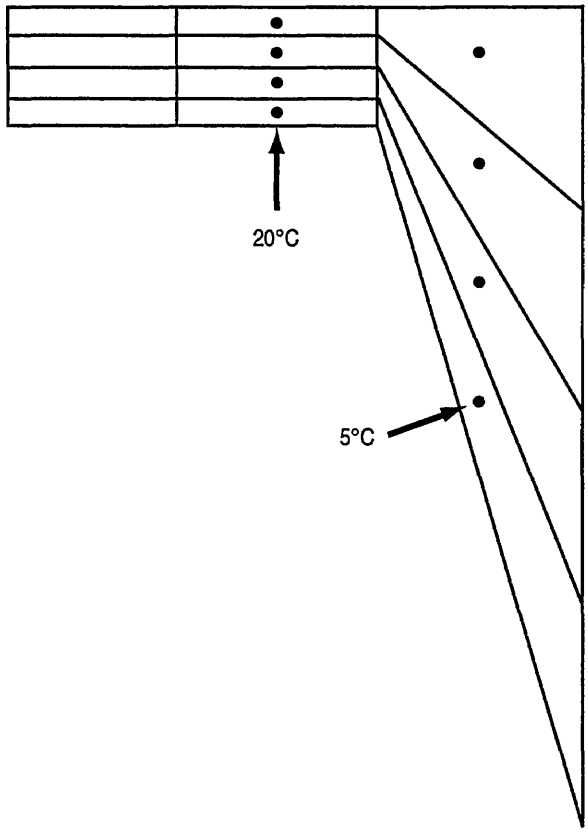

Fig. 8 — Schematic illustrating the large change in temperature that can occur between adjoining grid cells in the bottom layers of a sigma coordinate model if there is a large change in depth between the cells such that the cells lie on different sides of a strong thermocline

4.0 TESTS OF VERTICAL MIXING

Tests of vertical mixing were conducted to look at mixing within the surface and bottom mixed layers. In addition, an experiment involving the formation of a tidal mixing front was performed to investigate a situation where the surface and bottom mixed layers combine to mix the entire water column from top to bottom.

The POM, ECOM-si, and SZM models use a fully implicit scheme for vertical mixing. With this scheme, the vertical diffusion terms are evaluated using the newly calculated values of the field being mixed. For example, for the two-time-level scheme used by ECOM-si, fully implicit mixing of temperature would be written as

$$T^{(n+1)} = T^{(n)} + \Delta t \left(\frac{\partial}{\partial z} \left(K_H \frac{\partial T^{(n+1)}}{\partial z} \right) + \ldots \right). \tag{49}$$

Since the new $(n + 1)$ values of the field are not known at the beginning of a timestep, the implicit treatment of vertical diffusion couples the numerical equations in the vertical, which requires the solution of a tridiagonal set of equations at each horizontal point.

Although the fully implicit diffusion scheme suffers a loss of accuracy from temporal truncation error because it is not centered in time, it has the very desirable property for the treatment of vertical diffusion that it is always numerically stable and physically well-behaved. As a practical

matter, these latter properties have generally been considered to be more important for vertical diffusive processes in numerical ocean models than strict temporal accuracy. The implicit treatment of the vertical diffusion terms should be reasonably accurate when the diffusivities are small and the timescale of the mixing is long, and when the diffusivities become large, it could be argued that the precise values of the diffusive fluxes are not very well known anyway.

The version of SCRUM we received used the Crank-Nicolson temporal numerical scheme for vertical diffusion. With the Crank-Nicolson scheme, the vertical diffusion terms are calculated with the values of the field being diffused averaged between the (n) and $(n + 1)$ time levels, i.e.,

$$T^{(n+1)} = T^{(n)} + \Delta t \left(\frac{\partial}{\partial z} \left(K_H \frac{\partial \left(\left(T^n + T^{(n+1)} \right) / 2 \right)}{\partial z} \right) + \ldots \right) . \tag{50}$$

The Crank-Nicolson scheme is centered in time, which would appear to be an advantage over the fully implicit scheme that is not centered. However, although the Crank-Nicolson diffusion scheme is, like the fully implicit scheme, unconditionally numerically stable, it has the undesirable property that the gradient of the field being advected can be reversed if the eddy coefficients K are sufficiently large. This gradient reversal is caused by "overshoot" of the diffusive fluxes that can occur if the vertical diffusion number does not satisfy the constraint

$$\frac{2\Delta t K}{\Delta z^2} < 1.0 , \tag{51}$$

where Δz is the vertical grid spacing. With realistic surface atmospheric forcing, the K values can become very large and (51) can be easily violated. The resulting vertical mixing tends to be noisy and inaccurate. This is the reason most models use fully implicit vertical mixing. With fully implicit mixing, the diffusive flux is calculated only from the new values of the field being diffused, and diffusive overshoots cannot occur.

Vertical mixing tests conducted with SCRUM did indeed produce noisy and erratic results. This behavior was eliminated as the timestep was reduced to the point where the restriction defined by (51) was approximately obeyed. We note that the newer version of SCRUM, Version 3.0, has been converted to use fully implicit vertical mixing, as is used by the other models.

4.1 Surface Mixing

Some simple tests of surface-mixed-layer deepening were conducted to determine the amount of surface mixing provided by the models. The tests follow the idealized mixing experiments conducted by Martin (1985, 1986). One set of tests consists of the erosion of stable thermal stratification by a constant wind stress with zero surface buoyancy flux. Another set of tests consists of the shallowing of an initially deep mixed layer due to steady surface heating and a constant wind stress. A third set of tests looks at convective deepening due to surface cooling.

Since the surface mixing tests consider only local mixing, the setup of the model region is not especially critical as long as non-local effects (i.e., horizontal variations) in the central part of the

domain remain small during the period of model integration. However, since the models have been configured to allow the use of periodic boundaries in both the x and y directions, the models can be set up to behave exactly as a local, one-dimensional (1-D) model in which the horizontal variations are identically zero.

For the surface mixing tests, the models were set up with a 4×4 grid of horizontal points (6×6 for ECOM-si), with periodic boundaries in both horizontal directions. This setup gives a 2×2 horizontal grid of interior model points, which is the minimum number of horizontal points that the models can be run with without significant code modification. With periodic lateral boundaries in both directions and with horizontally uniform initial conditions and surface forcing, the ocean models behave exactly like local, 1-D, mixed-layer models.

A constant-spaced vertical grid was used with fairly high 1-m resolution to resolve the mixing accurately. The latitude of the model region was taken to be 29.91° N where the inertial period is 24 h (i.e., $f = 2\pi/(24\text{ h})$). The internal timestep Δt_i was taken to be 600 s. The background viscosity and diffusivity below the mixed layer were set to 0.1 cm^2/s for all the models.

For the wind-deepening experiment, the initial temperature was defined as $T(z) = 24 - 0.05\ z$, where the depth z is in meters and the salinity was set to a constant 35 psu. Three experiments were conducted with constant wind stress values of 1, 4, and 16 dynes/cm^2. The surface-mixed-layer depths (SMLD) after 1, 2, and 5 d are listed in Table 4 and hourly values of SMLD are plotted in

Table 4 — Depth of Surface Mixing for Deepening of the Surface Mixed Layer Due to a Constant Wind Stress and for the Shallowing of the Mixed Layer Due to a Constant (1 dyne/cm^2) Wind Stress and a Constant Surface Heat Flux. Two MLDs are Listed: the First is the Depth Where T is 0.2°C Less Than the SST, and the Second is the Depth Where the Vertical Diffusivity Drops Below 1 cm^2/s.

Wind Stress =	1	4	16	1	1	1	dynes/cm^2
Heat Flux =	0	0	0	600	1200	2400	ly/d
Model	Mixed-Layer Depth (m) After 24 h						
POM	16/15	31/31	57/61	12/15	5/11	2/7	
ECOM	16/15	30/31	55/58	10/11	4/9	2/6	
SZM	17/16	32/32	60/65	10/12	5/10	2/7	
Model	Mixed-Layer Depth (m) After 48 h						
POM	18/17	35/35	67/71	12/14	5/10	2/6	
ECOM	18/17	35/35	65/69	11/12	4/9	2/5	
SZM	19/18	36/36	69/73	12/13	4/9	2/7	
Model	Mixed-Layer Depth (m) After 120 h						
POM	21/20	41/41	81/83	11/13	4/9	2/5	
ECOM	21/20	41/41	81/83	11/11	4/9	2/5	
SZM	21/21	43/43	83/83	11/12	4/8	2/5	

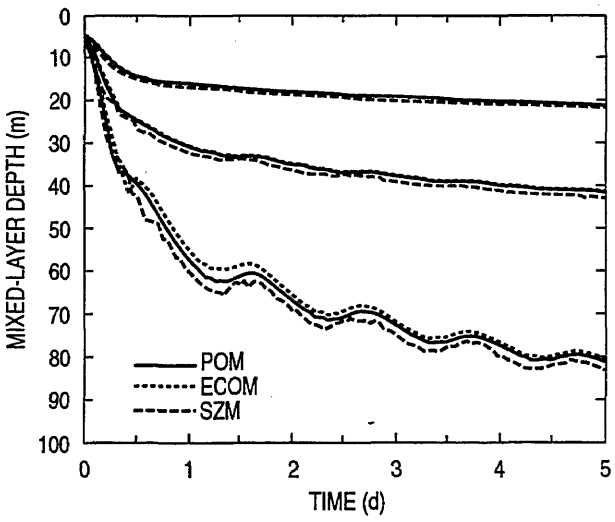

Fig. 9 — Surface mixed-layer depth vs. time for the models for a constant wind stress that is turned on at $t = 0$. Three cases are shown for wind stress values of 1, 4, and 16 dynes/cm^2. The initial condition was zero velocity, a constant salinity of 35 psu, and a linear temperature stratification of 5°C/100 m, with an SST of 24°C. The latitude is 29.91° N.

Fig. 9. Two different SMLDs are listed in Table 4. The first is the depth at which the temperature is 0.2°C less than the sea surface temperature (SST) (this is also the definition of the SMLD plotted in Fig. 9). The second is the depth at which the vertical diffusivity in the surface mixed layer (SML) decreases to less than 1.0 cm^2/s. For the wind-deepening experiments, these two depths tend to be quite similar.

For the shallowing experiment, the initial temperature and salinity were taken to be a constant 19°C and 35 psu, respectively, and the wind stress was taken to be a constant 1 dyne/cm^2. Three experiments were conducted with surface heat fluxes of 600, 1200, and 2400 ly/d. No penetration of the surface heat flux below the ocean surface (i.e., from solar radiation) was employed. The depths of surface mixing for the shallowing experiments after 1, 2, and 5 d are listed in Table 4. As for the wind-deepening experiments, two SMLDs are listed: the depth at which the temperature becomes 0.2°C less than the SST and the depth at which the vertical diffusivity decreases to less than 1 cm^2/s. In the case of strong surface heating, there can be quite a large temperature gradient within the SML; hence, the depth at which the temperature decreases to less than 0.2°C below the SST may significantly underestimate the actual depth to which surface mixing is occurring.

The SMLDs predicted by POM, ECOM-si, and SZM are generally quite similar for both the wind-deepening and shallowing experiments. POM and ECOM-si are set up with identical parameters for the MYL2.5 turbulence model; hence, the slight difference in MLD must be due to the differences in the numerical schemes. ECOM-si gave slightly greater SMLDs for the 16 dyne/cm^2 wind-deepening case when the timestep was reduced.

The SMLDs predicted by SZM are a little noisier than those predicted by POM and ECOM-si (Fig. 9). This is likely due to the fact that the MYL2 turbulence scheme does not use prognostic equations to predict the TKE and the turbulent length scale ℓ. The use of prognostic equations tends to provide a smoother evolution of the turbulence fields. It is notable, however, that the implementation of the MYL2 mixing scheme in SZM gives results similar to the MYL2.5 scheme in these tests.

For the tests of convective deepening of the SML due to surface cooling, conditions were as for the mixed-layer shallowing tests except that the initial temperature was taken to be a constant

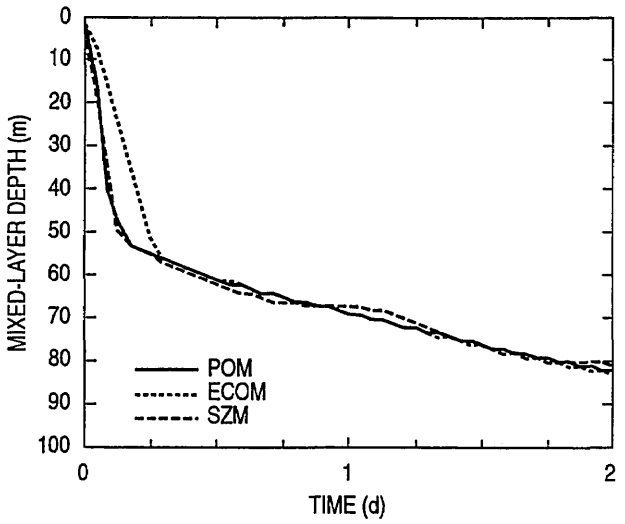

Fig. 10 — Surface mixed-layer depth vs. time for the models for convective deeping due to a surface cooling of –1000 ly/d. The initial temperature was a constant 19°C from the surface to 50 m, followed by a linear decrease to 18.5°C at 100 m. The surface wind stress was 1 dyne/cm^2.

19°C down to 50 m, followed by a small, linear decrease to 18.5°C at 100 m, and the surface heat flux was taken to be –1000 ly/d. As for the shallowing tests, the surface wind stress was 1 dyne/cm^2. For this test, the SMLD was defined as the depth at which the vertical diffusivity decreased below 1 cm^2/s.

The SMLDs from the convective deepening test are plotted in Fig. 10. After 24 h, the SMLDs predicted by POM, ECOM-si, and SZM were 69, 69, and 67 m, respectively, and after 48 h, the depths were 82, 83, and 81 m. We might expect that the TKE transport in the MYL2.5 turbulence model used by POM and ECOM-si would generate larger SMLDs in this convective case than the MYL2 turbulence model used by SZM, but as found by Martin (1985), the difference is small. Because of its formulation, the MYL2 turbulence model does not provide any convective penetration (i.e., erosion of the stable stratification at the base of the turbulent mixed layer). Based on the results here and previous tests (Yamada and Mellor 1975; Martin 1985), the MYL2.5 turbulence model provides only a small amount of convective penetration.

4.2 Mixing in the Bottom Boundary Layer

Local mixing of the bottom boundary layer (BBL) due to oscillatory tidal currents was simulated by setting up the models with doubly periodic boundary conditions as was done for the surface mixing cases in the previous section. A surface pressure gradient force was imposed to mimic forcing by the barotropic M2 tide, which has a period of 12.42 h.

The surface pressure gradient force was applied to the models through the term that would normally be used to define the local tidal potential. (The tidal potential is the effective force generated by the sun and the moon on the oceans to drive the barotropic ocean tides and is the equilibrium position that the ocean's surface would take for a particular tidal mode if there were no other influences.) The term for the tidal potential was added to all the models by subtracting the horizontal gradient of the tidal potential from the horizontal gradient of the surface elevation where the latter appear in the momentum equations.

From the horizontally homogeneous form of the momentum equations, it can be shown that the tidal currents generated by a forcing term equivalent to a sinusoidal surface elevation gradient in the x direction of the form

$$\frac{\partial \zeta_p}{\partial x} = A_p \sin(\omega t), \tag{52}$$

where ζ_p is the tidal potential, A_p is the amplitude of the surface elevation gradient, ω is the tidal frequency, and t is the time, will generate barotropic currents

$$\bar{u} = A_u \cos(\omega t) \tag{53}$$

and

$$\bar{v} = A_v \sin(\omega t), \tag{54}$$

where the current amplitudes, A_u and A_v, are

$$A_u = A_p \frac{g\omega}{\omega^2 - f^2} \tag{55}$$

and

$$A_v = A_p \frac{gf}{\omega^2 - f^2}. \tag{56}$$

This is the classic problem of the periodic forcing of a harmonic oscillator. It can be seen that, for this idealized problem, the amplitude of the current goes to infinity as the frequency of the forcing ω approaches the local inertial frequency f. For $\omega = 1.405 \times 10^{-4}$ s^{-1} (the frequency of the M2 tide), $f = 2\pi/(24\text{ h})$, and $A_p = 10^{-5}$, the amplitude of the currents are $A_u = 95$ cm/s and $A_v = 49$ cm/s. Note that this analysis has not included bottom drag, which will tend to modify the currents to some degree. The value of the bottom drag coefficient (calculated from (21) with $c_{b_{\min}} = 0.0025$ and $z_o = 0.3$ cm) is 0.0061.

Besides the amplitude of the tidal forcing, the depth of mixing will depend on the Coriolis parameter, the initial stratification, and the parameterization of bottom drag. The temperature and salinity were initialized as for the wind-deepening experiments in Sec. 4.1, i.e., the temperature was defined by an SST of 24°C with a linear gradient of 0.05°C/m, and S was taken to be a constant 35 psu. The total depth was taken to be 100 m, the vertical grid spacing was a uniform 1 m, f was set to $2\pi/(24\text{ h})$, and Δt was 600 s. Note that the total depth should not affect the depth of mixing in the BBL unless the mixing gets near the surface.

Figure 11 shows BBL depth (BBLD) versus time for the models, calculated for three different values of the tidal forcing amplitude A_p: 2.5×10^{-6}, 5×10^{-6}, and 1×10^{-5}. The values of the tidal current amplitude A_u from (55) for these three cases are 24, 48, and 95 cm/s.

The BBLD in Fig. 11 is defined as the depth at which the temperature becomes 0.2°C greater than the bottom-layer temperature. Note that with this definition, the BBLD for the initial stratification

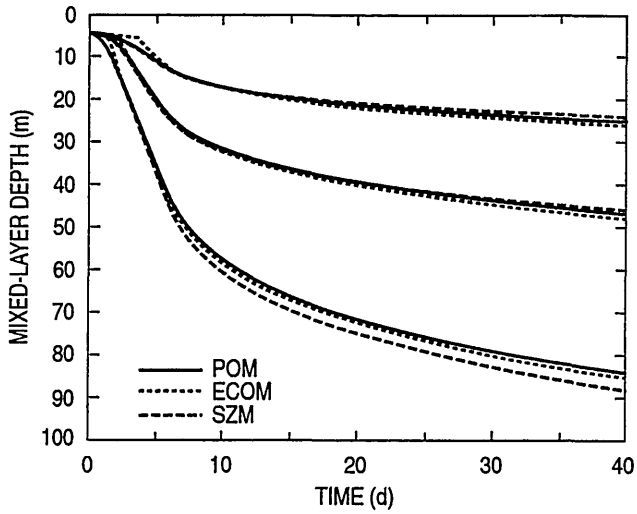

Fig. 11 — Bottom mixed-layer depth vs. time for the models for an oscillating tidal current with a period of 12.42 h. The tidal current is driven by an imposed surface pressure gradient. Three cases are shown with maximum amplitudes of the tidal current of 24, 48, and 95 cm/s. The initial condition was zero current, a constant salinity of 35 psu, and a temperature profile defined by a uniform stratification of 5°C/100 m and a bottom temperature of 19°C. The latitude is 29.91° N, where $f = 2\pi/(24\text{ h})$.

that was used is 4 m, as can be seen in Fig. 11. The BBLD defined by the temperature change of 0.2°C was generally within 2–3 m of the BBLD defined by the depth of significant turbulent mixing (defined as the depth where $K > 1$ cm^2/s).

The near-surface currents produced by the models in these simulations agreed very closely with the currents that were expected based on (53–56). Near the bottom, the currents are reduced by the bottom drag condition imposed by the quadratic drag law used in the models. It is, of course, the vertical current shear generated by the bottom drag that generates the mixing in the BBL in this problem. The turbulent mixing starts at the bottom and the depth of the BBL increases as the turbulence erodes the density stratification from below.

The BBLDs predicted by the models are quite similar and evolve similarly in time. The BBLDs predicted by SZM increase relative to the BBLDs predicted by POM and ECOM-si as the magnitude of the forcing is increased.

In the initial simulations of tidal mixing, a problem was encountered with the BBLDs predicted by POM. The BBLD was much larger than the values obtained with the other models, and the profiles of K_H were very noisy. Investigation of the problem showed that it was due to round-off error in calculating the density when using 32-bit floating point arithmetic. A comment within subroutine DENS of POM recommends that several variables be made double precision when using 32-bit arithmetic. When the recommended variables in DENS were converted to double precision, the mixing problems were eliminated.

Note that the density calculation used in POM differs from that used in the other models in that POM includes the effect of pressure on the density. This aspect of the density calculation appears to be especially sensitive to round-off error. If the model density includes the effect of pressure, this must be accounted for when calculating the buoyancy term in the TKE equation, which POM does. Otherwise, vertical turbulent mixing will be significantly (and incorrectly) retarded by the vertical gradient of density due to the pressure.

4.3 Formation of a Tidal Mixing Front with Stratification Generated by Surface Heating

The formation of a tidal mixing front along an infinite coast was simulated by setting up the models in what we call "pseudo 2-D" form. In this form, one of the horizontal directions (in this case, the y direction) is set up with the minimum number of interior gridpoints (two) and with periodic boundaries. With this setup, the models behave as if they were 2-D without the effort to actually convert the models to a true 2-D form (although, of course, such a pseudo 2-D model is not as computationally efficient as a true 2-D model would be). Note that while the pseudo 2-D setup does not allow any variability in the y direction, currents in the y direction can develop.

The bathymetry in the offshore direction consisted of a linear slope of 0.000571 from a depth of 20 m at the coast to a depth of 200 m at a distance of 315 km from the coast, followed by a constant depth of 200 m out to the open boundary at a distance of 406 km from the coast (Fig. 12). The horizontal grid spacing was 7 km. For the main set of simulations, 20 sigma layers were used in the vertical with a spacing in the deep water of 5 m at the surface and with a uniform stretching of the grid to the bottom. Simulations were also conducted with SZM with z-level grids of 20 and 50 levels.

Rather than impose an initial stratification, the thermal stratification was allowed to develop from an initially homogeneous condition under the influence of surface heating and mixing. The solar flux (Q_r) and the downward surface heat flux ($Q_b + Q_e + Q_s$) were taken to be 450 and –300 ly/d, respectively. These fluxes give a net surface heating of 150 ly/d. A two-band approximation of Jerlov Type IA seawater (Jerlov 1968) was used to describe the solar extinction

$$\gamma(z) = 0.38e^{z/(20\text{ m})} + 0.62e^{z/(0.35\text{ m})} . \tag{57}$$

This parameterization gives more solar penetration than usually occurs in coastal water, which tends to be more turbid than Type IA. However, this extinction, together with the surface heat fluxes, maintains an SMLD of about 12 m (due to convection driven by the solar penetration) without the need to employ a surface wind stress to provide mixing of the surface layer.

The M2 tide was forced at the open boundary by specifying a sinusoidally varying surface elevation with an amplitude of 1 m and a period of 12.42 h. Table 5 lists results from the simulations. The values listed in Table 5 include the internal mode (baroclinic) timestep Δt, the timestep for the free surface mode Δt_e, the amplitude of the surface elevation at the coast, the maximum tidal current that occurs within the model, and the depth of the water at the location of the front. The tidal elevation amplitude predicted by the models at the coast is about 3.5 m (the bathymetry is such that the tide amplifies significantly over the shelf), and the maximum tidal currents are about 70 cm/s.

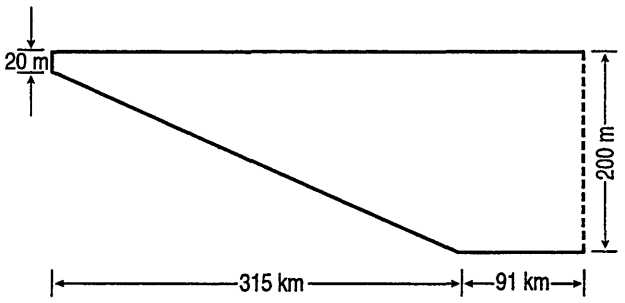

Fig. 12 — Schematic showing the model domain used for the problem of the formation of a tidal mixing front

Table 5 — Comparison of Model Results for the Formation of a Tidal Mixing Front. Tidal Amplitude at Open Boundary is 100 cm.

MODEL	VERTICAL GRID	NUMBER LAYERS	Δt (s)	Δt_e (s)	MAX AMP AT COAST (cm)	MAX CURRENT (cm/s)	DEPTH AT FRONT (m)
POM	sigma	20	900	30	351	70	88
ECOM	sigma	20	900	900	330	66	84
SZM	sigma	20	900	900	366	68	88
POM	sigma	20	200	10	356	71	88
ECOM	sigma	20	200	200	368	73	92
SZM	sigma	20	200	200	358	66	88
SZM	z-level	20	900	900	377	73	96
SZM	z-level	50	900	900	378	71	96

Figure 13 shows temperature sections at 30 d from the model simulations conducted with vertical grids of 20 sigma layers and with $\Delta t = 900$ s. The results of the models are similar. The surface heating builds up a vertical temperature differential of about 1.3°C in the offshore water.

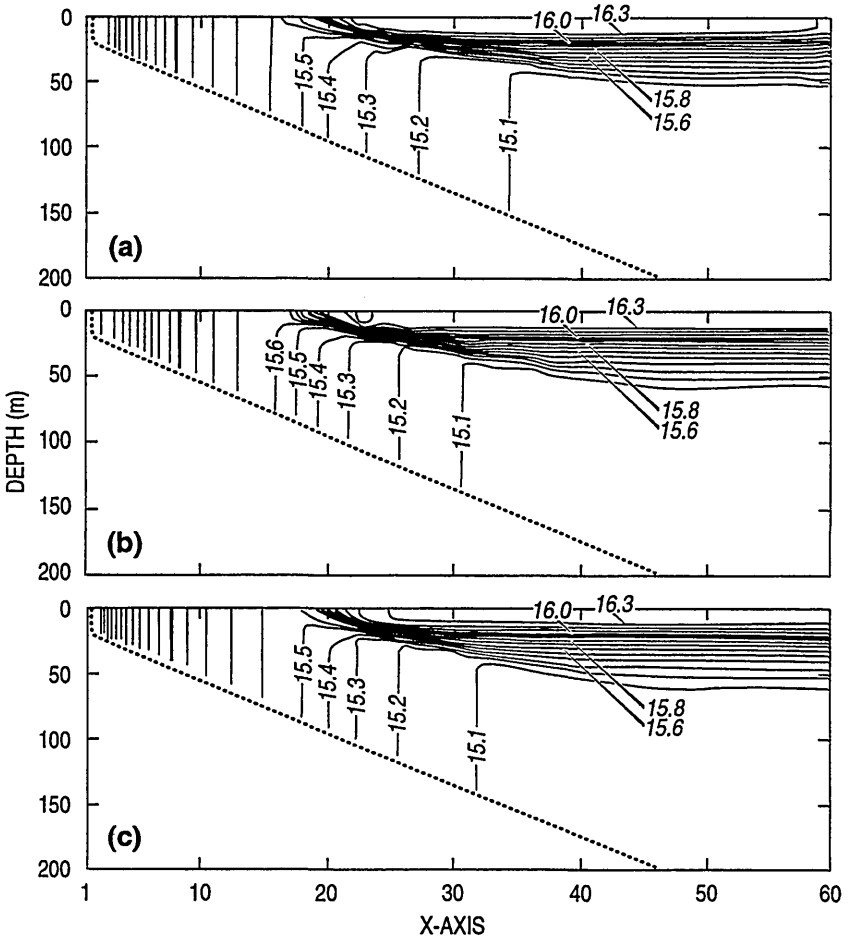

Fig. 13 — Temperature x-z sections at 30 d for the formation of a tidal mixing front for (a) POM, (b) ECOM-si, and (c) SZM. The tick marks along the horizontal axis denote the gridpoint locations. 20 sigma layers were used in the vertical, with an upper layer thickness of 5 m in deep water and a uniform stretching to the bottom.

Mixing near the bottom due to the tidal currents maintains a deep BBL. A tidal mixing front forms at a depth of about 90 m where the BBL merges with the SML. The SST differential across the front is about 0.7°C. The front is qualitatively similar to the observation of a tidal mixing front in the Irish Sea shown by Simpson and James (1986). Offshore of the front, the water is stratified, and inshore of the front the water is vertically mixed from the surface to the bottom. There is a cooling of the SST as the tidal mixing front is approached from its offshore side. However, there is a warming of the water toward the coast on the inshore side of the front that is caused by the fixed surface heat flux being mixed into a water column of decreasing depth.

Table 5 lists model results with baroclinic timesteps of both 900 and 200 s to give some idea of the sensitivity of the simulations to the timestep. Note that a timestep of 200 s is much smaller than would normally be needed to maintain numerical stability on a 7-km grid. ECOM-si showed the largest change due to the reduction of the timestep, a 10% increase in the tidal elevation and currents. This increase may be due to the damping of surface waves by ECOM-si's fully implicit treatment of the surface waves at larger timesteps, which is discussed in Sec. 5.0. SZM showed a decrease in tidal amplitude with the smaller timestep and POM showed a small increase.

Figure 14 shows a comparison of results from SZM for the tidal mixing front problem conducted with different vertical grids: (a) a sigma coordinate grid with 20 layers (this is the same result with SZM that appears in Fig. 13c), (b) a 20-layer primarily z-level grid with 18 z-levels and two sigma layers at the surface to take up surface elevation changes (this grid provides the same

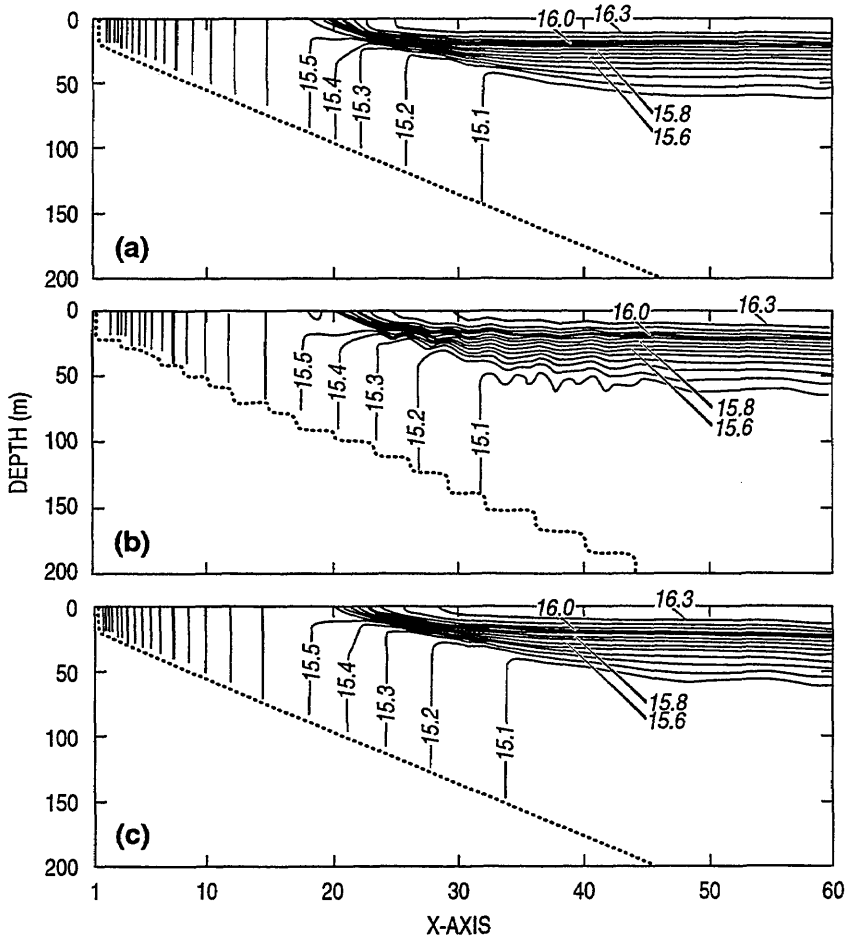

Fig. 14 — Temperature x-z sections at 30 d for the formation of a tidal mixing front using SZM with different vertical grids: (a) 20 sigma layers as in Fig. 13, (b) 20 layers with z-levels, except for two sigma layers at the surface, and (c) 50 layers with z-levels, except for two sigma layers at the surface. The 20-layer sigma and z-level grids in (a) and (b) have the same vertical spacing in deep water. The 50-layer z-level grid in (c) has a uniform 4-m vertical spacing and exactly resolves the shelf slope.

resolution as the 20-layer sigma coordinate grid in the deepest water), and (c) a uniform (unstretched) primarily z-level vertical grid with 50 total layers with the two top layers being sigma layers.

The results of the simulations with the different vertical grids in Fig. 14 are generally similar. However, one noticeable difference between the results is the wavy disturbance of the isotherms in Fig. 14b, the simulation with the grid of two sigma layers and 18 z-levels. In this simulation, the fitting of the bathymetry to the z-levels results in a step-like bottom, with several horizontal gridpoints along each step. A result of the steps is that the convergence of the onshore, barotropic tidal flow is concentrated at the faces of the steps. Hence, instead of the vertical flow varying uniformly in the horizontal, there is a vertical "jet" at the face of each of the steps that, since the flow is approximately barotropic, reaches all the way up through the water column. A schematic that illustrates this is shown in Fig. 15. As can be seen in Fig. 14b, the vertical jets displace the isotherms above each of the steps.

Better resolution of the bathymetry, which can be obtained by increasing the number of vertical levels, will reduce this effect. In Fig. 14c, the (primarily) z-level grid with uniform (4-m) spacing exactly resolves the bottom slope. Hence, the horizontal variation of the convergence of the onshore/offshore tidal flow and the vertical displacement of the isotherms occurs smoothly. Some z-level models employ truncation of the bottom grid cells to the actual bathymetry to better resolve the bathymetry (Wolff et al. 1996).

The two simulations with SZM that were conducted with z-level grids resulted in slightly (3%) stronger tides than the simulation with sigma coordinates (Table 5).

4.4 Checkerboard Mixing

A phenomenon that occurs with all the models in certain situations is differential vertical mixing at alternate horizontal gridpoints, a phenomenon that will be referred to here as "checkerboard mixing." This was observed to occur in the SML under conditions of surface heating and light winds.

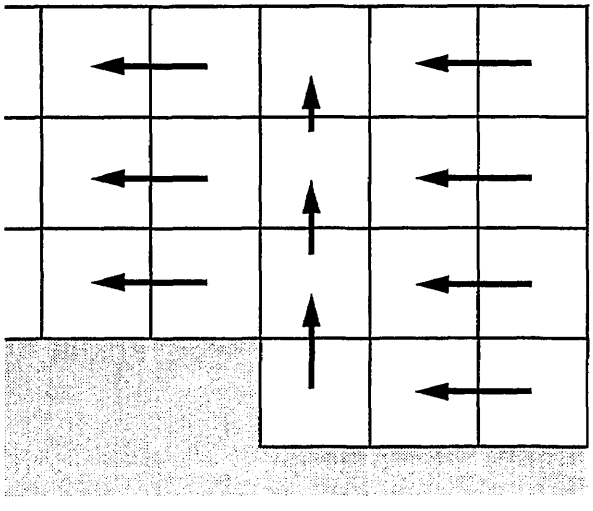

Fig. 15 — Schematic showing an x-z section for the horizontal convergence of a barotropic flow toward the coast for a model with a z-level vertical grid in which the bathymetry is rounded to the nearest z-level. The horizontal convergence is localized at the front of a step and generates a vertical jet at the front of the step.

An idealized experiment will be conducted here to illustrate how checkerboard mixing occurs. The experiment was conducted on a horizontal grid of 11 x 11 points with doubly periodic boundaries and with 20 layers in the vertical. The horizontal grid spacing was 5 km, the vertical grid spacing was 5 m, and the latitude was taken to be 29.91° N. The initial conditions were $T = 20°C$ and $S = 35$ psu with the ocean at rest. The forcing was a uniform wind stress of 0.5 dynes/cm^2 and a uniform surface heating of 150 ly/d (73 watts/m^2). The results presented here were obtained with POM; however, the other models show the same behavior.

Figure 16 shows contour plots of the SST and SMLD after 2 d. The tick marks along the axes show the gridpoint locations. What has happened is that the vertical mixing has mixed deeper at alternate gridpoints. The SST shows the checkerboarding pattern since the SST is warmer where the SMLD is shallower. The checkerboarding occurs because of the way vertical mixing is calculated by the models on a C grid. The staggered velocities (Fig. 17) are averaged to the grid-cell centers to calculate the vertical mixing coefficients. The vertical mixing of T and S occurs at the grid-cell centers where T and S are defined. However, the vertical mixing coefficients for momentum are averaged back to the staggered velocity points to calculate vertical mixing of u and v.

The checkerboarding pattern gets set up because slightly weaker mixing at a point relative to that at an adjoining point is reinforced on the next timestep. The weaker vertical mixing of T and S results in stronger stratification at that location, which inhibits mixing on the next timestep. The vertical shear of the horizontal velocity remains fairly uniform horizontally because of the horizontal averaging of the vertical eddy coefficients for momentum. Hence, the vertical stability is governed by the vertical mixing of T and S.

Figure 17 shows a schematic illustrating the checkerboarding situation. The vertical eddy coefficients at the grid-cell centers alternate in magnitude, and the strength of the vertical stratification alternates accordingly. When the vertical eddy coefficients are averaged to the staggered u velocity

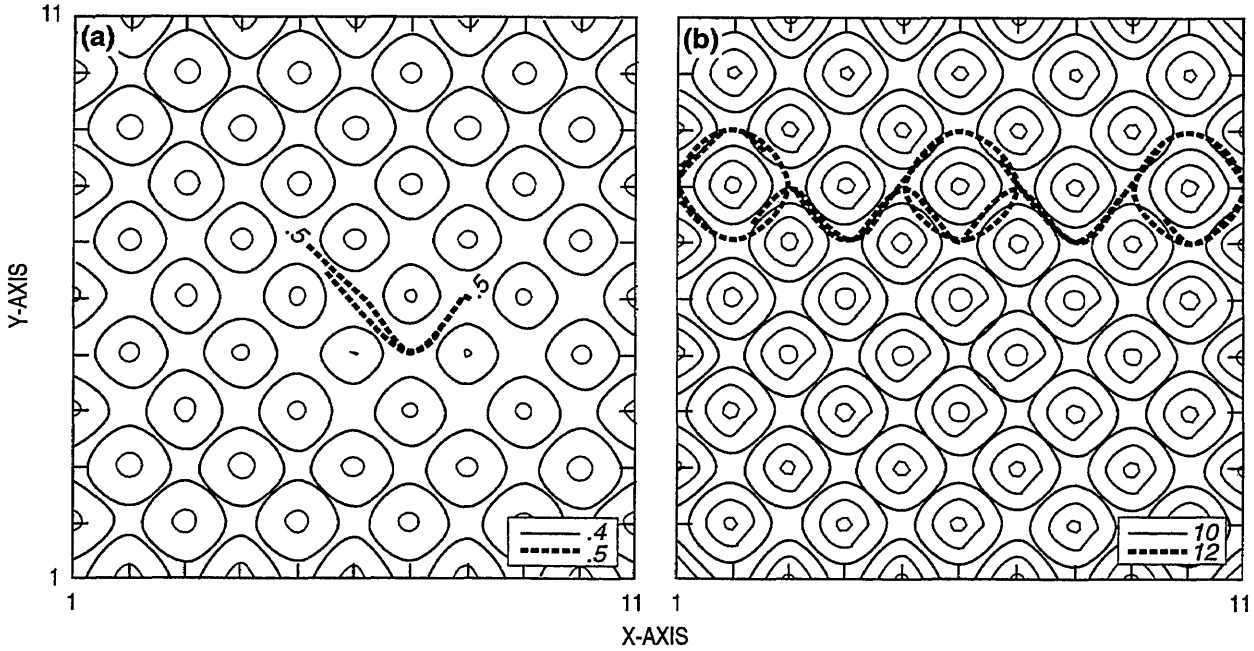

Fig. 16 — (a) SST and (b) SMLD at 2 d for the simulation of checkerboard mixing. The SMLD is defined as the depth at which the temperature is 0.2°C less than the SST. The contour interval is 0.1°C for the SST and 2 m for the SMLD.

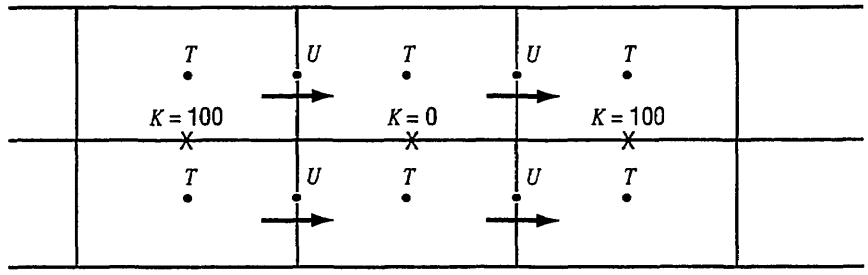

Fig. 17 — Schematic to help explain the cause of checkerboard mixing. The diagram shows an x-z section through the center of a row of grid cells.

points at the edges of the grid cells, the horizontal variations are averaged out. Hence, the vertical eddy coefficients for momentum, and as a result, the vertical velocity shears are fairly uniform in the horizontal. Once the checkerboarding pattern is initiated, it reinforces itself and becomes locked in.

If the conditions in the idealized problem discussed above are kept perfectly uniform in the horizontal, the response remains horizontally uniform with identical mixing at each horizontal point. However, any horizontal inhomogeneity introduced into the problem can trigger the checkerboard mixing. In the case shown in Fig. 16, the SST at the center gridpoint of the domain was increased by 0.01°C. With the introduction of this inhomogeneity, the checkerboarding initially spreads laterally in the direction of the applied windstress, and within 2 d covers the entire domain.

Checkerboard mixing patterns were observed in several different simulations that were conducted, including some preliminary simulations of the tidal mixing front problem in which a weak wind stress was applied and the solar penetration was turned off. However, discussions with other modelers indicate that it has not been widely noticed. Whether or not checkerboard mixing occurs depends on a number of factors including the applied surface fluxes, the degree of solar penetration, and the grid spacing. It seems less likely to occur or make itself known when realistic temporally and spatially varying atmospheric forcing is being used. Even when it does occur, it might be viewed primarily as an aesthetic problem. The discussion of checkerboard mixing was provided here mainly to acquaint the reader with the phenomenon in the event it should be encountered.

5.0 TEST SURFACE WAVE PROPAGATION

Wave propagation is an important aspect of the dynamics of coastal regions. The next three sections discuss tests of wave propagation in the models. These tests consider freely propagating surface waves, freely propagating internal waves, and coastal-trapped waves including surface and internal Kelvin waves and barotropic shelf waves.

Note that, for a particular application, the accuracy of propagation of a particular type of wave may or may not be significant. However, an ability to accurately simulate the propagation of surface, internal, and coastal-trapped waves is, in general, desirable for a model that is to be applied to a wide range of coastal processes.

For all the wave tests, the waves are defined to be propagating in the x-direction. Hence, the model domains are periodic in x, with the wavenumber in the x-direction chosen so as to fit an integral number of wavelengths.

The models are initialized from the linear, analytical solution for the waves, and the model errors are calculated by comparison of the model fields with the analytic solution. To optimize comparison of the model simulations with the linear, analytic solutions, the amplitudes of the waves are made small to minimize nonlinear effects, bottom drag is set to zero, the diffusion coefficients are kept small, and the lateral boundaries for the coastal trapped wave simulations are made free slip.

Three aspects of wave propagation by the models are investigated: (1) phase speed error, (2) damping, and (3) distortion of the wave form,

The phase speed error for the models is calculated by finding the phase speed that gives the best fit of the analytic solution to the model solution, i.e., the minimum root-mean-squared (RMS) difference or maximum correlation between the analytic and model solutions. Note that the other model errors are calculated with the phase of the analytical solution matched to that of the model solution.

The damping is calculated by finding the fractional damping factor D for the analytic solution that gives the minimum RMS error between the analytic and model fields (with the phase of the analytical solution matched to the phase of the model solution). Originally, the damping was calculated by comparing the magnitudes of the maximum and minimum values of the analytic and model fields; however, this calculation tended to underestimate the model damping if there was any noise in the model fields. The e-folding damping timescale t_d is computed from the elapsed time t and the amount of damping as $t_d = -t/ln(D)$.

The distortion of the waves is characterized by the correlation between the analytic and model fields (again, with the phases of the fields matched).

These three types of error can be considered to be independent. For example, if the wave propagates with a certain phase speed error, but maintains its original amplitude (corresponding to zero damping error), its damping timescale will be infinite. Similarly, if the wave propagates with a certain phase speed error and a certain amount of damping, but perfectly maintains its initial form, the correlation of the model solution with the analytic solution will be exactly one.

In addition to calculating the phase speed error, damping error, and correlation, the RMS difference between the analytic and model solutions is also reported. This RMS error is calculated with the phase of the analytic solution matched to that of the model solution, but without any damping applied to the analytic field, i.e., the RMS error will reflect both the damping and distortion of the model solution, but not the mean phase speed error.

5.1 Description of Surface Wave Tests

The propagation of plane parallel surface waves was tested using a doubly periodic (periodic in both x and y) model domain. With the waves propagating in the x direction, there is no variation of the fields in y, i.e., the problem is 2-D with variation only in x and z. Hence, the doubly periodic grid is used with the minimum dimension in y (two interior gridpoints) that can be used with the 3-D model codes (this was referred to earlier as a quasi 2-D model grid).

The waves were initialized in the models from the analytical solution for linear, shallow-water (i.e., with wavelength large relative to the depth), surface gravity waves propagating in the x-direction. The equations for these waves are

$$\frac{\partial u}{\partial t} = fv - g\frac{\partial \zeta}{\partial x}, \tag{58}$$

$$\frac{\partial v}{\partial t} = -fu, \tag{59}$$

$$\frac{\partial \zeta}{\partial t} = -H\frac{\partial u}{\partial x}. \tag{60}$$

The analytical solution for the waves is

$$\zeta = A\ \cos(kx - \omega t), \tag{61}$$

$$u = A\frac{\omega}{kH}\cos(kx - \omega t), \tag{62}$$

$$v = A\frac{f}{kH}\cos(kx - \omega t), \tag{63}$$

where A is the maximum amplitude of the surface displacement, k is the horizontal wavenumber, and ω is the frequency. Note that $k = 2\pi/L$, where L is the wavelength and $\omega = 2\pi/P$, where P is the wave period. The dispersion relation for these waves is

$$\omega^2 = c_o^2 k^2 + f^2, \tag{64}$$

where $c_o = (gH)^{\frac{1}{2}}$ and the phase speed is

$$c = \frac{\omega}{k} = \left(c_o^2 + \frac{f^2}{k^2}\right)^{\frac{1}{2}}. \tag{65}$$

For wavelengths less than about 100 km, the Earth's rotation does not have much effect on surface waves because the period of the waves is sufficiently short relative to the local inertial period ($2\pi/f$) that rotational effects do not have much time to act. The effect of the wave frequency on the phase speed is easier to see if the expression for the phase speed (65) is rewritten as

$$c = c_o\left(1 - \frac{f^2}{\omega^2}\right)^{-\frac{1}{2}}. \tag{66}$$

For the shorter waves, $c = c_o$ and the waves are approximately non-dispersive, i.e., the phase speed is independent of wavelength. For long wavelengths of order 1000 km, the phase speed depends on the wavelength and the waves are dispersive.

Tests were conducted both for short waves ($L < 100$ km) and for long waves ($L > 1000$ km) that are affected by rotation. The depth H of the model region was set to 40.81 m, which gives $c_o = 20$ m/s. T and S were set to constant values of 20°C and 35 psu, respectively. (Note that the particular (constant) values of T and S that are used do not affect the propagation of surface waves in the models.) Bottom drag was set to zero. Ten uniformly spaced layers were used in the vertical. Since the bottom drag is set to zero, there are no vertical variations in the flow and the number of vertical layers that is used is arbitrary. For the Asselin-filtered leapfrog schemes of POM and SZM, ν was set to 0.05, which is the value typically used in the models.

The internal timestep Δt for the explicit surface wave propagation scheme used by POM was (for most of the tests) set to a value commensurate with the need to (in more general circumstances) maintain stability for the internal wave propagation and horizontal advection terms for a maximum expected speed of about 2 m/s. This is greater than the maximum speed of internal waves and ocean currents in most coastal areas. The external timestep for POM Δt_e has to be made sufficiently small to maintain stability for the propagation of the surface waves. The restriction for POM's explicit scheme is that Δt_e must be sufficiently small that a surface wave cannot travel a distance Δx in a single timestep.

The models with an implicit treatment of the surface waves, ECOM-si and SZM, integrate all their terms with a single timestep. Since these models treat surface waves implicitly, their timestep is not restricted by stability considerations for the surface waves; hence, their timestep is limited by advection and internal wave propagation, as is the internal timestep of POM. Thus, the timestep for ECOM-si and SZM was generally set the same as the internal timestep used for POM. Some tests were conducted with ECOM-si and SZM with smaller timesteps to look at the effect of timestep on the accuracy of surface wave propagation for their implicit schemes.

5.2 Surface Wave Propagation without Rotation

The accuracy with which the models propagate surface waves depends on the numerical scheme and the temporal and spatial resolution used. A stability analysis of the numerical schemes used in the models for surface wave propagation with $f = 0$ is presented in App. A. The stability analysis predicts the damping and phase speed error to be expected for a particular numerical scheme, timestep, grid resolution, and wavelength. The errors predicted by the stability analysis agree well with the errors observed with the models.

The results of the tests of surface wave propagation are presented in Table 6, which lists the phase speed error, damping timescale, and the correlation and RMS error after 12 h for each of the models for different values of grid resolution, internal and external timestep, and wavelength. If values of the correlation are not listed in the table, it is because the waves became too damped at 12 h to calculate reliable values. Note that the RMS error asymptotes to 0.7071 cm as the model solution becomes completely damped.

The most notable result in Table 6 is how much more accurately the explicit scheme propagates surface waves, especially surface waves of short wavelength. The reason is the much smaller timestep used by the explicit scheme to resolve surface wave propagation. The relatively large timestep generally used with the implicit models cannot resolve the propagation of short surface waves.

Table 6 — Comparison of Model Errors for Propagation of Surface Gravity Waves for $f = 0$. Correlation and RMS Error are at 12 h.

MODEL	Δx (km)	Δt (s)	Δt_e (s)	$\frac{\Delta t_e C}{\Delta x}$	WAVELENGTH (km)	PTS PER WAVE	SPEED ERROR (%)	DAMP TIME (h)	COR	RMS ERROR (cm)
POM	1	200	10	0.20	256	256	–0.002	4440.0	0.99999	0.0033
POM	1	200	10	0.20	64	64	–0.037	277.0	0.99990	0.0313
POM	1	200	10	0.20	16	16	–0.60	17.0	0.99999	0.3522
POM	1	200	10	0.20	8	8	–2.38	4.5	0.99997	0.6585
POM	1	200	10	0.20	4	4	–9.4	1.3	0.99922	0.7070
ECOM	1	200	200	4.00	256	256	–0.41	11.6	0.99999	0.4560
ECOM	1	200	200	4.00	64	64	–4.7	0.78	0.99579	0.7070
ECOM	1	200	200	4.00	16	16	–36.2	0.09		0.7070
ECOM	1	200	200	4.00	8	8	–60.0	0.05		0.7070
ECOM	1	200	200	4.00	4	4	–77.8	0.03		0.7070
SZM	1	200	200	4.00	256	256	–0.31	221.0	0.99989	0.0373
SZM	1	200	200	4.00	64	64	–4.7	15.0	0.99989	0.3823
SZM	1	200	200	4.00	16	16	–36.1	2.3	0.99997	0.7031
SZM	1	200	200	4.00	8	8	–59.9	1.5	0.88246	0.7069
SZM	1	200	200	4.00	4	4	–77.7	1.2		0.7070
ECOM	1	10	10	0.20	16	16	–0.81	0.91	0.65799	0.7071
SZM	1	10	10	0.20	16	16	–0.84	17.0	0.99999	0.3533

The accuracy of surface wave propagation in the implicit models can be increased by reducing the timestep, as is shown in the lower part of Table 6. However, because both the external and internal modes of the implicit models are integrated with the same timestep, reducing the timestep significantly increases the computer time required to run these models.

For the propagation of surface waves without rotation, ECOM-si and SZM have equivalent phase speed errors, but ECOM-si has much greater damping because of its fully implicit treatment of the terms governing the surface wave propagation. Table 6 shows that even with a very small timestep (10 s), ECOM-si strongly damps short surface waves. The terms governing the surface waves in POM and SZM are centered in time, which in itself does not result in any damping. The damping of surface waves in POM and SZM is due to the Asselin filter (App. A).

5.3 Surface Wave Propagation for Long Waves Affected by Rotation

In this section, the propagation of surface waves is examined for $f = 0.7292 \times 10^{-4}$ s^{-1}, which corresponds to a latitude of 29.91° N. The depth is taken to be 40.81 m as in the previous section. The wavelength used in these tests is 1280 km. Equation (65) gives a phase speed for these waves of 24.89 m/s, and it can be seen that rotation has increased the phase speed of the waves over that (20 m/s) for the case without rotation. The period of the waves is 14.28 h, which is sufficiently long for rotational effects to significantly affect the waves.

Table 7 shows the damping and phase speed error calculated for the models for grid resolutions of 10–40 km and timesteps of 1800–7200 s. As was the case with $f = 0$, the implicit treatment of the surface waves is much more damping than an explicit treatment when the timestep for the implicit scheme is set by the typical stability limitations for horizontal advection and internal wave propagation.

The damping in both POM and SZM is due to the Asselin filter. The damping of POM is about 20 times smaller than that of SZM because of the smaller timestep used for the calculation of the surface waves with the explicit treatment of the external mode.

The damping of ECOM-si is about 10 times larger than that of SZM. The severe damping of ECOM-si in these results is due to the combination of the fully implicit scheme and the large timestep. Note that the results obtained for ECOM-si in Table 7 (as are all the results for ECOM-si in this report) are for the AB2 treatment of the Coriolis terms that was implemented to allow the use of large timesteps. The errors calculated with ECOM-si were somewhat noisy, and the damping and phase speed errors in Table 7 are averages of values taken over the first few timesteps. Calculations with the original lagged treatment of the Coriolis terms were, however, even more noisy and sometimes became unstable.

The phase speed error for these long wavelength waves is less than 1% for POM. For ECOM-si and SZM, the phase speed errors are small for the typical grid resolutions used in coastal modeling, though the errors become significant (1–10%) at the larger timesteps that might be used if these models were applied to large domains with a grid spacing of 20–40 km.

5.4 Tidal Propagation

The primary importance of surface wave propagation in coastal models is usually to provide an accurate simulation of tides and wind setup or storm surge. Since the tides generally have fairly

Table 7 — Comparison of Models for Propagation of Surface Gravity Waves for a Value of f Corresponding to 29.91° N. Correlation and RMS Error are at 48 h.

MODEL	Δx (km)	Δt (s)	Δt_e (s)	$\frac{\Delta t_e C}{\Delta x}$	WAVELENGTH (km)	PTS PER WAVE	SPEED ERROR (%)	DAMP TIME (h)	COR	RMS ERROR (cm)
POM	5	900	45	0.22	1280	256	–0.004	16000	1.0	0.0021
POM	10	1800	90	0.22	1280	128	–0.015	8100	1.0	0.0042
POM	20	3600	180	0.22	1280	64	–0.064	4100	1.0	0.0082
POM	40	7200	360	0.22	1280	32	–0.26	2100	1.0	0.0157
ECOM	5	900	900	4.48	1280	256	0.2	61	1.0	0.3844
ECOM	10	1800	1800	4.48	1280	128	0.3	36	1.0	0.5663
ECOM	20	3600	3600	4.48	1280	64	1.0	20	1.0	0.6766
ECOM	40	7200	7200	4.48	1280	32	10.0	16	1.0	0.6014
SZM	5	900	900	4.48	1280	256	–0.15	770	1.0	0.0423
SZM	10	1800	1800	4.48	1280	128	–0.70	380	1.0	0.0446
SZM	20	3600	3600	4.48	1280	64	–2.62	200	1.0	0.1505
SZM	40	7200	7200	4.48	1280	32	–8.5	122	1.0	0.3698

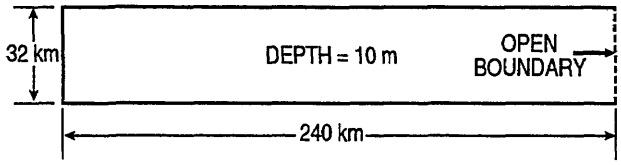

Fig. 18 — Model domain for the test problem of tides in a bay

long wavelengths, the tidal propagation by the models tends to follow the behavior obtained in the previous section for long surface waves with rotation.

In this section, a sample tidal calculation is used to illustrate the general effect of the temporal resolution of the models on tidal prediction accuracy. This calculation is presented as a single illustration. A thorough study of the accuracy of tidal prediction with the models would involve investigation of a number of variables including both temporal and spatial resolution, bathymetry variability, and nonlinear tidal generation.

The model domain for this test problem is a rectangular bay 240 km long and 32 km wide with a uniform depth of 10 m (Fig. 18). The domain is closed except for an open boundary on the east end. The tidal elevation is specified at the open boundary (i.e., a "clamped" elevation boundary condition) with a sinusoidal variation, an amplitude of 10 cm, and a period corresponding to the M2 tide (12.42 h). (A small amplitude is used to reduce nonlinear effects.) The horizontal grid resolution is 4 km and the vertical grid consists of 10 equally spaced sigma layers. T and S are taken to be constant. The Coriolis parameter is $f = 2\pi/(24\text{ h})$ and the bottom friction coefficient is 0.0061. Since the magnitude of the vertical mixing coefficients will affect the tidal calculation in these models, the vertical mixing coefficients were set to a constant 100 cm^2/s for all the models to provide a more consistent comparison.

Table 8 — Comparison of the Models for the Propagation of the Tide in a Bay. The Magnitude and Phase Listed in the Table is that for the Maximum Elevation at the West End of the Bay.

MODEL	Δt (s)	Δt_e (s)	MAXIMUM MAGNITUDE (cm)	ELEVATION PHASE (deg)
POM	50	2.5	9.63	188
	100	5	9.61	188
	200	10	9.58	188
	400	20	9.54	187
	800	40	9.49	186
	1600	80	9.56	182
	3200	160	9.85	181
ECOM-si	50	50	9.58	189
	100	100	9.53	188
	200	200	9.43	188
	400	400	9.25	187
	800	800	8.87	187
	1600	1600	8.00	186
	3200	3200	6.32	180
SZM	50	50	9.63	189
	100	100	9.63	189
	200	200	9.62	189
	400	400	9.61	190
	800	800	9.54	190
	1600	1600	9.92	185
	3200	3200	11.06	195

Table 8 lists the maximum tidal elevation and corresponding phase at the west end of the bay for POM, ECOM-si, and SZM for values of Δt ranging from 50 to 3200 s. The maximum elevation values from Table 8 are plotted in Fig. 19. Note that for POM, Δt_e has been taken to be equal to $\Delta t/20$.

For small values of Δt, the models predict a similar magnitude and phase for the elevation at the west end of the bay. For the fine grids usually used in coastal modeling ($\Delta x < 1$ km), the small timesteps that are required ($\Delta t < 200$ s) provide good resolution of the tidal

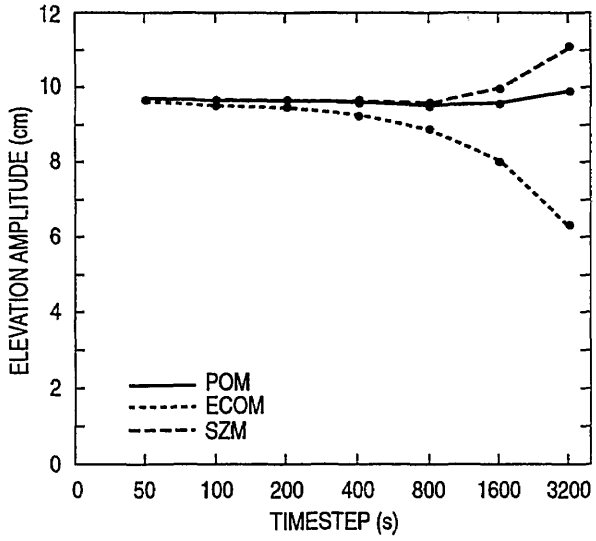

Fig. 19 — Maximum tidal elevation at west end of bay for POM, ECOM-si, and SZM for different values of the timestep. The tide was forced by specifying the elevation at the east end of the bay with an amplitude of 10 cm with a period corresponding to the M2 tide.

period and will generally produce fairly accurate tidal predictions, depending on the accuracy requirements and the particular aspects of the simulation.

The simulations with POM maintained the best accuracy for the tidal amplitude at the larger timesteps (Table 8, Fig. 19). SZM provides fairly good accuracy for this problem up to $\Delta t = 800$ s. For larger timesteps, there are significant increases in SZM's errors due to poor resolution of the tidal period. The tidal amplitude predicted by ECOM-si shows significant damping at the larger timesteps, which is consistent with the results of the other surface wave propagation tests.

As the grid spacing and timestep are increased, the implicit treatment of surface waves results in increasingly severe temporal truncation error for tidal simulation. In simple geometries, the temporal truncation error of the implicit schemes at large timesteps may dominate the tidal prediction error. However, in tidal simulations in realistic coastal environments, spatial truncation error will also become more severe as grid resolution is decreased because of poor representation of the bathymetry and the coastline. Consideration of spatial truncation error tends to limit the size of the grid spacing used in coastal tidal simulations.

6.0 TEST OF INTERNAL WAVE PROPAGATION

Internal wave propagation in the models was tested by comparing the model solutions to analytical solutions for small amplitude internal waves propagating in a flat-bottomed ocean with a linear vertical density gradient.

The linearized equations for hydrostatic (long) internal waves propagating in the x-direction in a salt-stratified ocean are

$$\frac{\partial u}{\partial t} = fv - \frac{1}{\rho_o}\frac{\partial p}{\partial x}, \tag{67}$$

$$\frac{\partial v}{\partial t} = -fu\,, \tag{68}$$

$$\frac{\partial p}{\partial z} = -\rho g\,, \tag{69}$$

$$\frac{\partial S}{\partial t} = \frac{N^2}{\beta g} w\,, \tag{70}$$

$$\frac{\partial u}{\partial x} + \frac{\partial w}{\partial z} = 0\,, \tag{71}$$

where ρ is the density, ρ_o is a reference density, S is the salinity, $N = (\beta g \partial S/\partial z)^{1/2}$ is the Brunt-Viasala frequency, and β is the coefficient of expansion for salinity. (Salt stratification, rather than thermal stratification, was used for this test because of the high linearity between salinity and density changes at constant temperature, i.e., β is fairly constant.) The key to linearizing the internal wave equations is taking the density stratification in the salinity equation to be fixed, which requires that the amplitude of the internal waves be relatively small so that the basic stratification is not significantly changed by the propagation of the waves.

The analytical solution to the above equations for freely propagating internal waves for a flat bottom (H = constant) and a linear density stratification (N = constant) is

$$u = A\frac{\omega m}{k}\cos(mz)\cos(kx - \omega t)\,, \tag{72}$$

$$v = A\frac{fm}{k}\cos(mz)\sin(kx - \omega t)\,, \tag{73}$$

$$w = Aw\ \sin(mz)\ \sin(kx - \omega t)\,, \tag{74}$$

$$S' = A\frac{N^2}{\beta g}\sin(mz)\cos(kx - \omega t)\,, \tag{75}$$

where A is the maximum amplitude of the vertical displacement, S' is the deviation of the salinity from the background stratification, $m = n\pi/H$ is the vertical wavenumber, and n is the vertical mode number. The dispersion relation for the internal waves is

$$\omega^2 = \frac{N^2 k^2}{m^2} + f^2\,. \tag{76}$$

Hence, the phase speed is

$$c = \frac{\omega}{k} = \left(\frac{N^2}{m^2} + \frac{f^2}{k^2}\right)^{\frac{1}{2}}\,. \tag{77}$$

Equations (76) and (77) indicate that rotational effects tend to increase the frequency and phase speed of internal waves.

If we have

$$\frac{f^2}{k^2} << \frac{N^2}{m^2}, \tag{78}$$

the Earth's rotation will not significantly affect the propagation of the internal waves and the waves will be nondispersive. For the long internal waves being considered here (L about 10 km), this condition may or may not be satisfied, depending on the particular values of the parameters in (77). Slower phase speeds and longer wavelengths both increase the period of internal waves and increase the time during which rotational effects can act to modify the waves. Equations (76) and (77) can be combined to give

$$c = \frac{N}{m}\left(1 - \frac{f^2}{\omega^2}\right)^{-\frac{1}{2}}, \tag{79}$$

which makes it clear that the influence of the Earth's rotation on the propagation of internal waves depends on the ratio of the inertial and internal wave frequencies.

For the tests of internal wave propagation conducted with the models, the depth H was taken to be 40 m, the temperature was taken to be a constant 20°C, and a linear salinity stratification was used with a surface salinity of 30 psu and a bottom salinity of 40 psu. With this stratification, $N = 0.0426\ s^{-1}$. The background vertical viscosity for momentum was set to 0.1 cm^2/s. The background vertical diffusivity for salt was set to a lower value of 0.001 cm^2/s so as not to significantly diffuse the ambient salinity stratification. Bottom drag was set to zero. Sixteen layers were used in the vertical with a uniform spacing.

Tests were conducted both with $f = 0$ and with $f = 2\pi/(24\ h)$. Table 9 lists the analytical phase speeds for the internal waves for various wavelengths and vertical modes for the constant stratification used in the tests. Phase speeds are given for $f = 0$ and $= 2\pi/(24\ h)$.

As a matter of interest, non-hydrostatic phase speeds are also listed in Table 9. These internal wave phase speeds are calculated without making the hydrostatic approximation, which is used by all the models being tested here. Table 9 illustrates that the hydrostatic phase speeds are the same as the non-hydrostatic phase speeds for the longer internal waves, and are only slightly in error for 1-km wavelength waves.

6.1 Test Internal Wave Propagation without Rotation

Tables 10 and 11 list the errors calculated for the propagation of first and fourth mode internal waves of various wavelengths with $f = 0$. The horizontal resolution of the waves ranges from 64 to 4 points per wavelength. Since there are a total of 16 vertical layers, the mode 1 waves have 16 points per mode in the vertical and the mode 4 waves have 4 points per mode.

The errors for POM and SZM are similar. Since these models use basically the same numerical scheme for the baroclinic part of the equations (leapfrog in time and second-order, centered spatial

Table 9 — Analytical Phase Speed for Hydrostatic and Non-Hydrostatic Internal Waves for a Depth of 40 m and a Linear Salinity Stratification with a Brunt-Vaisala Frequency of 0.0426 1/s

		PHASE SPEED (cm/s)			
		HYDROSTATIC WAVES		NONHYDROSTATIC WAVES	
MODE	WAVELENGTH (km)	$f = 0$	$f = \frac{2\pi}{24\,\mathrm{h}}$	$f = 0$	$f = \frac{2\pi}{24\,\mathrm{h}}$
1	64	54.25	91.82	54.25	91.82
	32		65.69		65.69
	16		57.33		57.32
	8		55.04		55.03
	4		54.45	54.24	54.44
	2		54.30	54.21	54.26
	1		54.26	54.08	54.09
2	64	27.13	78.88	27.13	78.88
	32		45.91		45.91
	16		32.84		32.84
	8		28.66		28.66
	4		27.52	27.12	27.52
	2		27.22		27.22
	1		27.15		27.13
4	64	13.56	75.30	13.56	75.30
	32		39.44		39.44
	16		22.95		22.95
	8		16.42		16.42
	4		14.33	13.56	14.33
	2		13.76		13.76
	1		13.61		13.61

differences), the errors would be expected to be similar. The magnitude of the errors increases as the spatial resolution of the waves is reduced.

The phase speed and damping errors for ECOM-si are similar to those for POM and SZM. The correlation errors for ECOM-si are also similar at the longer wavelengths, but become larger at the shorter, less well-resolved wavelengths, which indicates more distortion of the waveform. The spatial treatment of the baroclinic mode in ECOM-si is the same as that in POM and SZM. However, the temporal treatment is different since ECOM-si lags the horizontal pressure gradient and advection terms in time. Even though the internal waves are fairly well resolved in time by the 200-s timestep, ECOM-si appears to suffer some effects of temporal truncation error when the internal waves are less well-resolved by the grid.

Figures 20 and 21 show plots of the initial salinity anomaly S' and the anomaly from the models at 48 h for the mode 1 internal waves for the 64- and 8-km wavelength tests. The anomalies for POM and SZM in Fig. 20 for the 64-km waves show good symmetry both horizontally and

Table 10 — Comparison of Model Errors for Propagation of First Mode Internal Gravity Waves for $f = 0$. Correlation and RMS Error are at 48 h. The RMS Error Asymptotes to 0.1768 psu as the Waves Become Fully Damped.

MODEL	Δx (km)	Δt (s)	Δt_e (s)	$\frac{\Delta t C}{\Delta x}$	WAVELENGTH (km)	PTS PER WAVE	SPEED ERROR (%)	DAMP TIME (h)	COR	RMS ERROR (cm)
POM	1	200	10	0.11	64	64	–0.3	5400	0.99998	0.0013
POM	1	200	10	0.11	32	32	–0.4	2300	0.99998	0.0027
POM	1	200	10	0.11	16	16	–0.9	645	0.99966	0.0103
POM	1	200	10	0.11	8	8	–2.7	110	0.99985	0.0416
POM	1	200	10	0.11	4	4	–9.7	34	0.98248	0.0946
ECOM	1	200	200	0.11	64	64	–0.3	9000	0.99994	0.0008
ECOM	1	200	200	0.11	32	32	–0.4	4000	0.99992	0.0020
ECOM	1	200	200	0.11	16	16	–0.8	650	0.99890	0.0104
ECOM	1	200	200	0.11	8	8	–2.5	120	0.98340	0.0477
ECOM	1	200	200	0.11	4	4	–9.7	30	0.82254	0.1002
SZM	1	200	200	0.11	64	64	–0.4	4500	0.99992	0.0021
SZM	1	200	200	0.11	32	32	–0.6	2050	0.99992	0.0034
SZM	1	200	200	0.11	16	16	–1.0	645	0.99990	0.0089
SZM	1	200	200	0.11	8	8	–2.8	185	0.99983	0.0153
SZM	1	200	200	0.11	4	4	–9.9	54	0.99948	0.0732
POM	1	50	2.5	0.027	64	64	–0.3	7100	0.99995	0.0009
POM	1	50	2.5	0.027	8	8	–2.7	160	0.99988	0.0323
ECOM	1	50	50.0	0.027	64	64	–0.3	7500	0.99997	0.0008
ECOM	1	50	50.0	0.027	8	8	–2.7	100	0.99791	0.0466
SZM	1	50	50.0	0.027	64	64	–0.4	7000	0.99933	0.0046
SZM	1	50	50.0	0.027	8	8	–2.9	330	0.99916	0.0173

Table 11 — Comparison of Model Errors for Propagation of Mode 4 Internal Gravity Waves for $f = 0$. Correlation and RMS Error are at 48 h. The RMS Error Asymptotes to 0.1768 psu as the Waves Become Fully Damped.

MODEL	Δx (km)	Δt (s)	Δt_e (s)	$\frac{\Delta t C}{\Delta x}$	WAVELENGTH (km)	PTS PER WAVE	SPEED ERROR (%)	DAMP TIME (h)	COR	RMS ERROR (cm)
POM	1	200	10	0.025	64	64	–6.5	450	0.99922	0.01272
POM	1	200	10	0.025	16	16	–5.7	350	0.99923	0.01557
POM	1	200	10	0.025	8	8	–7.5	130	0.99909	0.03612
POM	1	200	10	0.025	4	4	–14.2	44	0.98813	0.08370
ECOM	1	200	200	0.025	64	64	–5.7	500	0.97978	0.02568
ECOM	1	200	200	0.025	16	16	–5.4	300	0.99736	0.01963
ECOM	1	200	200	0.025	8	8	–7.2	90	0.99443	0.05177
ECOM	1	200	200	0.025	4	4	–13.9	45	0.93125	0.09932
SZM	1	200	200	0.025	64	64	–6.5	550	0.99912	0.01279
SZM	1	200	200	0.025	16	16	–5.8	420	0.99917	0.01428
SZM	1	200	200	0.025	8	8	–7.6	250	0.99977	0.02172
SZM	1	200	200	0.025	4	4	–14.5	100	0.99963	0.04602

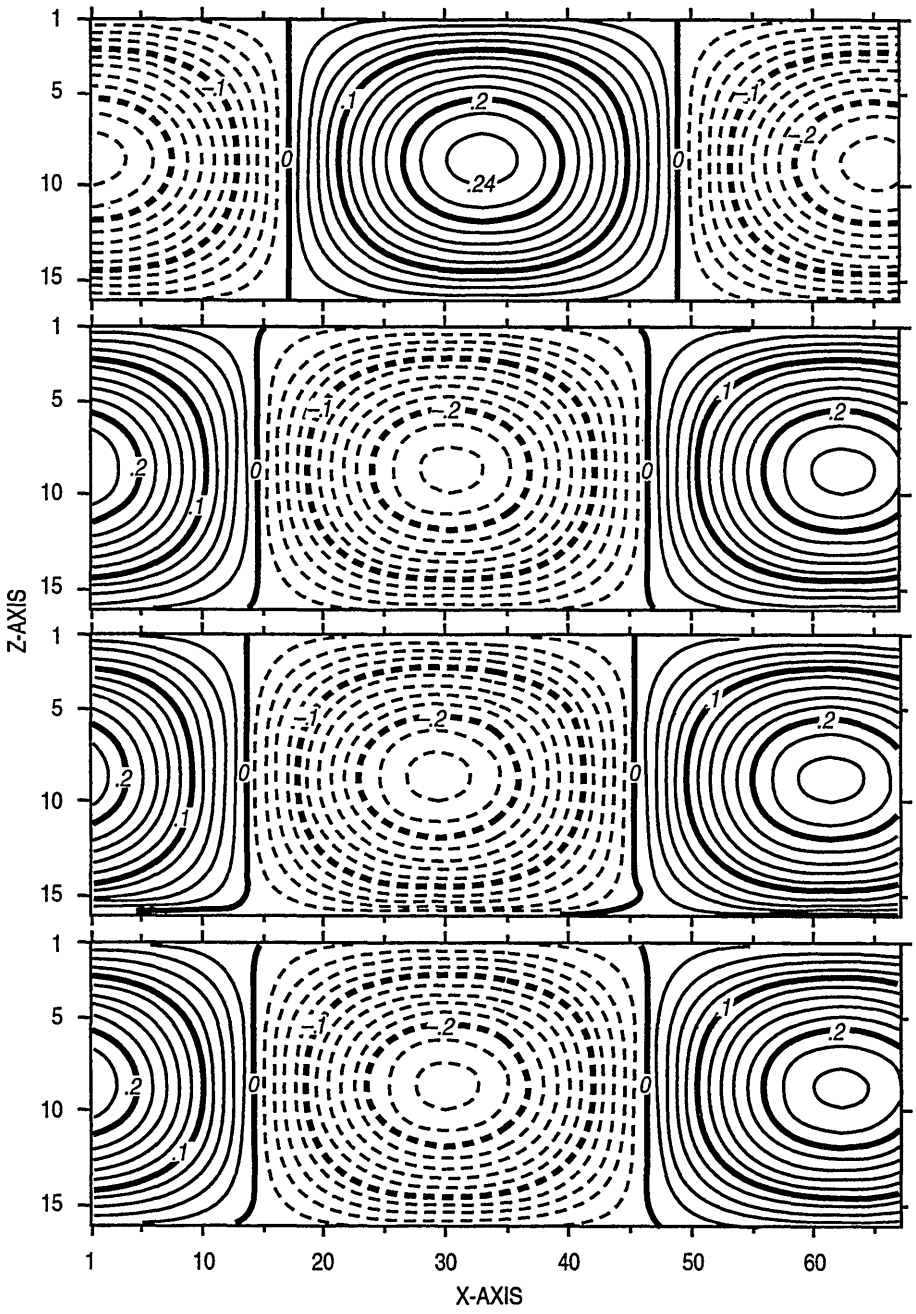

Fig. 20 — Salinity anomaly S' for propagation of internal waves of 64-km wavelength. The uppermost plot shows the initial condition, and the other plots show results after 48 h for POM, ECOM-si, and SZM. The internal wave amplitude was 100 cm and the timestep was 200 s.

vertically. However, there is a bit of distortion in the plot for ECOM-si, which is seen as a slight asymmetry between the isohalines in the top and bottom halves of the domain. This distortion is more apparent in Fig. 21 for the 8-km waves and is due to a slight decrease in the background salinity in the upper half of the domain and an increase in the bottom half (the salinity anomalies are computed based on the original background salinity stratification).

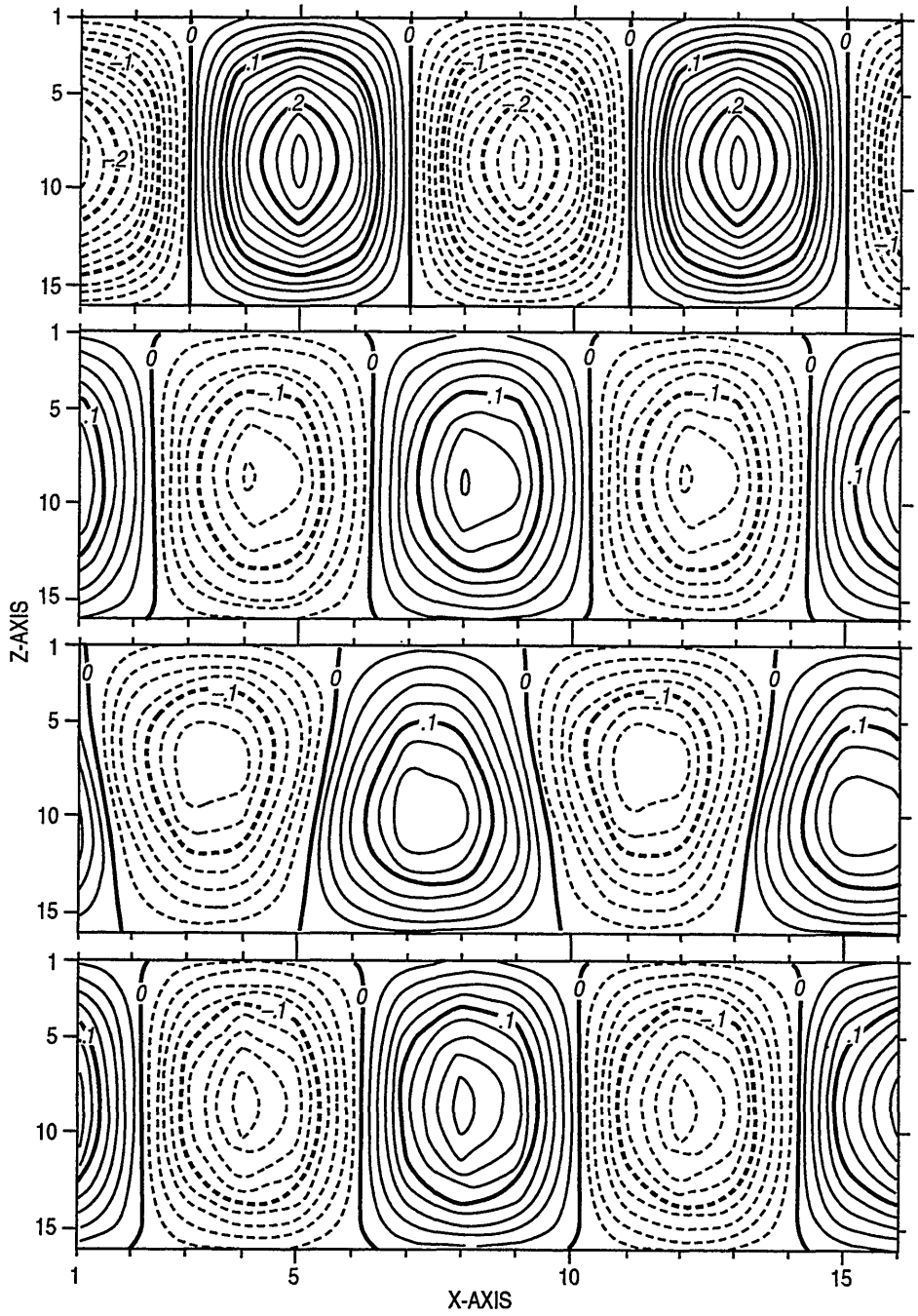

Fig. 21 — Salinity anomaly S' for propagation of internal waves of 8-km wavelength. The uppermost plot shows the initial condition and the other plots show results after 48 h for POM, ECOM-si, and SZM. The internal wave amplitude was 100 cm and the timestep was 200 s.

The modification of the background salinity by ECOM-si during internal wave propagation is the result of a numerical truncation error caused by a phase difference between the velocity and salinity values in the salinity advection term. An investigation of this error is presented in App. B. The magnitude of the truncation error is approximately proportional to the timestep and the square of the wave amplitude. For large timesteps and wave amplitudes, the modification of the background stratification by internal wave propagation in ECOM-si can be significant.

Figure 22 shows a plot of S' at 48 h from experiments with ECOM-si similar to those shown in Figs. 20 and 21, but with the timestep reduced from 200 to 50 s. These plots show better symmetry and the modification of the ambient stratification is reduced. Table 10 lists the errors for this experiment that show the reduction of the correlation and RMS errors brought about by the reduced timestep.

The bottom of Table 10 also shows errors for the propagation of mode 1 internal waves with POM and SZM with Δt reduced to 50 s. The errors are not much different from those obtained with the larger timestep except that the damping is reduced.

6.2 Test Internal Wave Propagation with Rotation

Table 12 lists the errors computed for the propagation of first-mode internal waves with a wavelength of 32 km for $f = 2\pi/(24\text{ h})$. The period of these waves, 13.53 h, is sufficiently long for the Earth's rotation to accelerate motions normal to the direction of the waves and to modify the

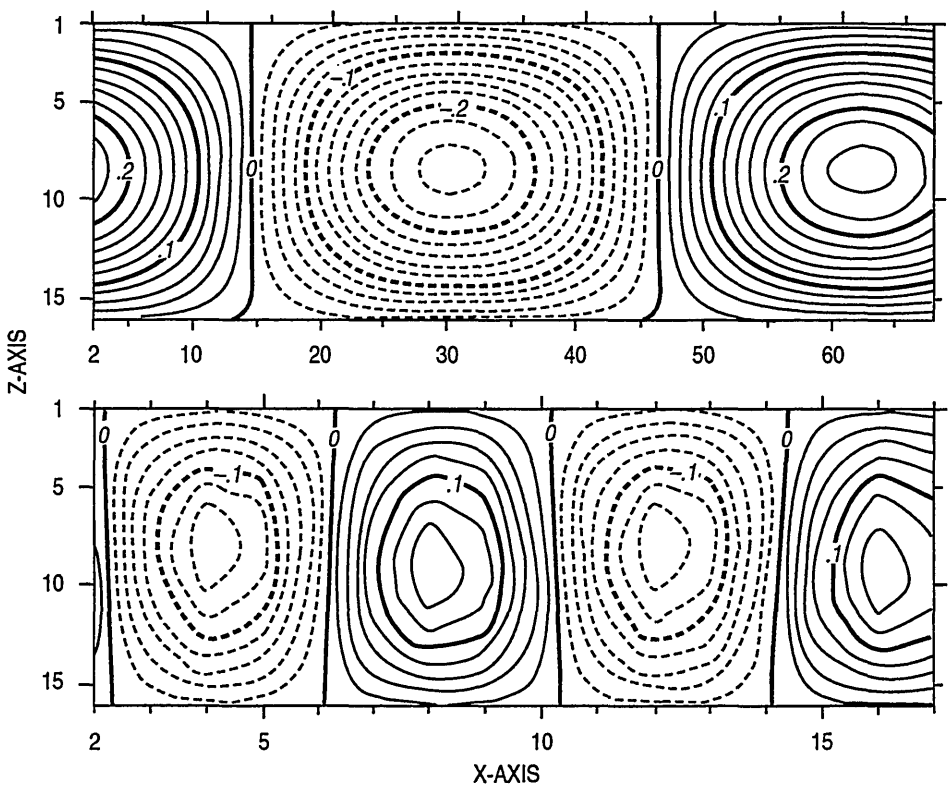

Fig. 22 — Salinity anomaly S' for propagation of internal waves of 64- and 8-km wavelengths with ECOM-si with a timestep of 50 s. The internal wave amplitude was 100 cm.

Table 12 — Comparison of Errors in the Salinity Anomaly Field S' for the Propagation of First-Mode Internal Gravity Waves for a Value of f Corresponding to 29.91° N. The Correlation and RMS Error are at 48 h. The RMS Error is 0.177 psu for a Fully Damped Model Solution.

MODEL	Δx (km)	Δt (s)	Δt_e (s)	$\frac{\Delta t C}{\Delta x}$	WAVELENGTH (km)	PTS PER WAVE	SPEED ERROR (%)	DAMP TIME (h)	COR	RMS ERROR (cm)
POM	1	200	10	0.11	32	32	−0.6	1500	0.99997	0.0019
POM	4	800	40	0.11	32	8	−4.5	400	0.99995	0.0145
POM	8	1600	80	0.11	32	4	−15.5	200	0.99985	0.0370
ECOM	1	200	200	0.11	32	32	−0.6	2000	0.99956	0.0046
ECOM	4	800	800	0.11	32	8	−4.0	350	0.99787	0.0179
ECOM	8	1600	1600	0.11	32	4	−15.2	200	0.99181	0.0486
SZM	1	200	200	0.11	32	32	−0.7	1500	0.99990	0.0042
SZM	4	800	800	0.11	32	8	−4.3	600	0.99995	0.0067
SZM	8	1600	1600	0.11	32	4	−15.4	340	0.99996	0.0157

wave propagation. The phase speed of the waves is 65.69 cm/s, about 20% larger than the phase speed of 54.25 cm/s for the case with $f = 0$. The horizontal resolution of the waves ranges from 32 to 4 points per wavelength. Since there are a total of 16 vertical layers, the waves have 16 points per mode in the vertical.

The phase speed, damping, and RMS errors for the waves are similar. ECOM-si has the highest correlation errors, and slightly higher RMS errors than POM and SZM. Some of ECOM-si's correlation and RMS error may be due to the modification of the ambient stratification caused by internal wave propagation, which was discussed in the previous section.

7.0 TEST PROPAGATION OF COASTAL-TRAPPED WAVES

Coastal-trapped waves are an important part of the dynamics of coastal regions. In this section, the accuracy with which the models propagate several types of coastal-trapped waves is examined. The types of waves considered are (1) barotropic Kelvin waves, (2) baroclinic Kelvin waves, and (3) barotropic shelf waves. The basic question is how well the models propagate these kinds of waves with a particular temporal and spatial resolution.

In all of these experiments, the models are configured in a periodic channel with boundaries at $y = 0$ and $y = L_y$. The along-channel wavenumber k is chosen so as to fit a single wavelength in the along-channel direction. As with the surface and internal waves, we look at three aspects of the wave propagation: phase speed error, damping, and distortion of the waveform. The wave propagation errors are calculated in the same way as the errors for the surface and internal waves.

7.1 Barotropic Kelvin Waves

The equations governing linear, barotropic Kelvin waves propagating in the x-direction along a coast are

$$\frac{\partial u}{\partial t} = fv - g\frac{\partial \zeta}{\partial x}, \tag{80}$$

$$\frac{\partial v}{\partial t} = -fu - g\frac{\partial \zeta}{\partial y}, \tag{81}$$

$$\frac{\partial \zeta}{\partial t} = -H\left(\frac{\partial u}{\partial x} + \frac{\partial v}{\partial y}\right). \tag{82}$$

The ocean depth H is taken to be constant. A boundary condition required for Kelvin waves is that the cross-shore velocity v is zero at the coast.

The solution of this set of equations for a barotropic Kelvin wave is

$$\zeta = Ae^{-y/r}\cos(kx - \omega t), \tag{83}$$

$$u = A\frac{\omega}{kH}e^{-y/r}\cos(kx - \omega t), \tag{84}$$

$$v = 0\,, \tag{85}$$

where A is the maximum amplitude of the surface displacement at the coast and $r = c/f$. The dispersion relation for the surface Kelvin waves is

$$\omega = c_o k\,, \tag{86}$$

where $c_o = (gH)^{\frac{1}{2}}$. Hence, the phase speed of the surface Kelvin waves is

$$c = \frac{\omega}{k} = c_o\,. \tag{87}$$

Some notable aspects of the Kelvin wave solutions are: (a) the cross-shore velocity v is zero everywhere (in the equation for v, the Coriolis term is exactly balanced by the cross-shore pressure gradient), (b) the amplitude of the Kelvin wave decays exponentially away from the coast with an e-folding scale r, which is referred to as the Rossby radius of deformation, (c) the cross-shore scale of the waves r is relatively large, i.e., for water depths exceeding 30 m, $r > 100$ km, (d) the speed of the waves is that for long surface gravity waves in the absence of rotation and does not depend on f, (e) the waves are nondispersive, and (f) the waves propagate only in one direction along the coast, with the coast on the right in the Northern Hemisphere and on the left in the Southern Hemisphere.

For the tests of surface Kelvin wave propagation in the models, the latitude was taken to be 29.91° N and the depth was taken to be 40.81 m. These values give $c = 20$ m/s and an offshore scale for the waves of $r = 275$ km. The along-channel wavelength of the waves was taken to be 1280 km. The along-channel wavelength was taken to be relatively large to reduce the effect of spatial truncation error in the along-channel direction. The width of the channel was taken to be 640 km, which is about 2.3 Rossby radii (the Kelvin wave propagation by the models is not sensitive to the width of the channel).

The results of the tests of surface Kelvin wave propagation by the models are presented in Table 13. Three main cases were run with horizontal grid resolutions of 10, 20, and 40 km and corresponding values of Δt of 1800, 3600, and 7200 s. Figure 23 shows the analytical solution for the surface elevation and velocity vectors at 48 h and Fig. 24 shows the surface elevation from the models at 48 h for the case with $\Delta x = 10$ km and $\Delta t = 1800$ s.

The relative results of the models are similar to those obtained for the propagation of surface gravity waves in Sec. 5.1. The phase speed errors for POM and SZM are similar to those in Table 7 for surface wave propagation in a rotating system (with the same parameter values). The damping timescale of the Kelvin waves for POM and SZM is about 50% longer than that of the corresponding freely propagating surface waves in Table 7. POM's explicit treatment of surface waves propagates the surface Kelvin wave very accurately with little phase speed error and only weak to moderate damping.

The large timestep used with the implicit schemes of ECOM-si and SZM results in strong damping of the Kelvin waves, with ECOM-si's damping by its fully implicit treatment of the free surface being especially strong. Figure 24 shows that the amplitude of the Kelvin wave propagated by ECOM-si (with $\Delta t = 1800$ s) is almost completely damped at 48 h. The damping in SZM, as in

Table 13 — Comparison of Errors in the Surface Elevation for the Propagation of Surface Kelvin Waves for a Value of f Corresponding to 29.91° N. The Correlation and RMS Error are at 48 h. The RMS Error is About 0.26 cm for a Fully Damped Model Solution.

MODEL	Δx (km)	Δt (s)	Δt_e (s)	$\frac{\Delta t_e C}{\Delta x}$	WAVELENGTH (km)	PTS PER WAVE	SPEED ERROR (%)	DAMP TIME (h)	COR	RMS ERROR (cm)
POM	10	1800	90	0.22	1280	128	–0.01	12300	1.0	0.0014
POM	20	3600	180	0.22	1280	64	–0.04	6200	1.0	0.0026
POM	40	7200	360	0.22	1280	32	–0.15	3100	1.0	0.0051
ECOM	10	1800	1800	4.48	1280	128	–1.5	32	0.99813	0.2474
ECOM	20	3600	3600	4.48	1280	64	–3.3	17	0.97005	0.3018
ECOM	40	7200	7200	4.48	1280	32	–9.7	9	0.76352	0.3134
SZM	10	1800	1800	4.48	1280	128	–1.0	630	0.99992	0.0241
SZM	20	3600	3600	4.48	1280	64	–3.8	330	0.99891	0.0458
SZM	40	7200	7200	4.48	1280	32	–12.8	200	0.99618	0.0716
ECOM	40	360	360	0.22	1280	32	–0.2	160	0.99994	0.0833
SZM	40	360	360	0.22	1280	32	–0.2	3100	1.0	0.0051

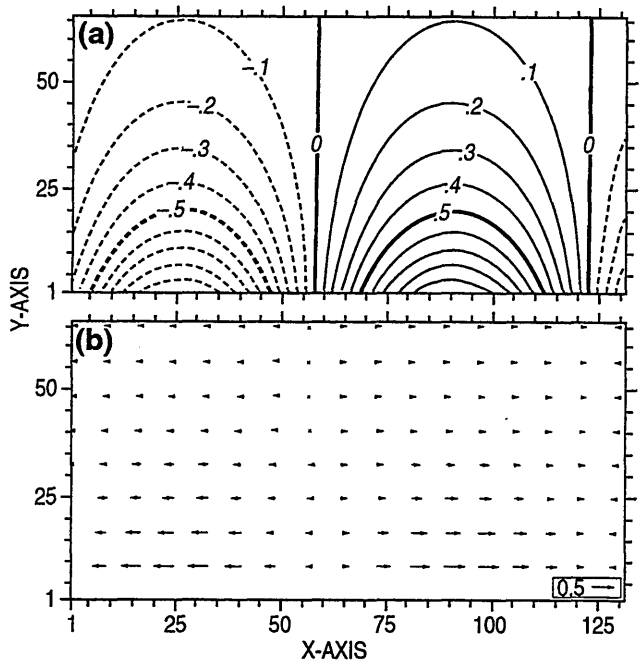

Fig. 23 — Analytical solution for a surface Kelvin wave at 48 h: (a) surface elevation in centimeters and (b) horizontal velocity vectors. The scaling arrow in the velocity vector plot indicates a speed of 0.5 cm/s.

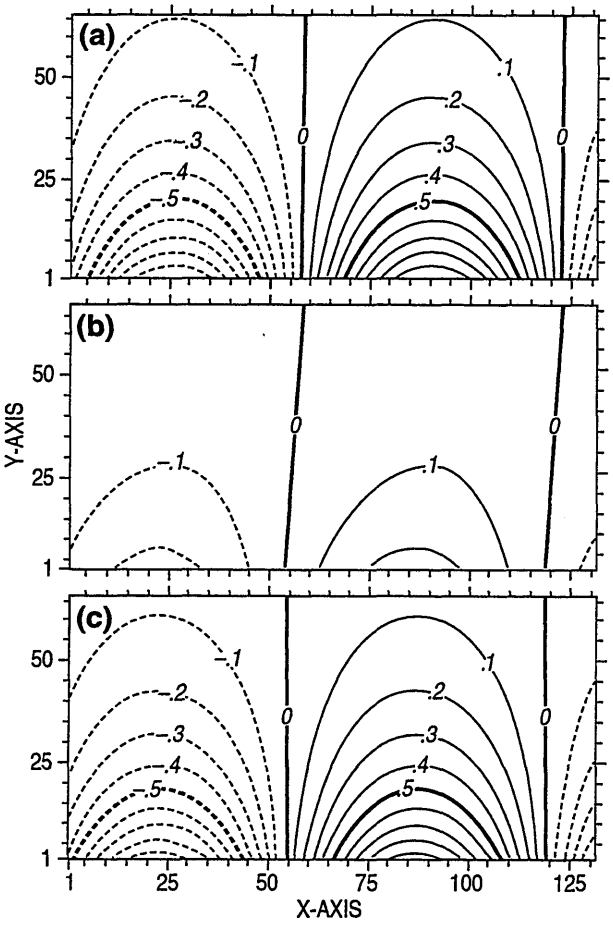

Fig. 24 — Comparison of surface elevation (cm) from the models at 48 h for the propagation of a surface Kelvin wave: (a) POM, (b) ECOM-si, and (c) SZM. The horizontal grid spacing was 10 km and the baroclinic timestep was 1800 s.

POM, is due to the Asselin filter, but is much larger with SZM than POM with the same filter coefficient ($\nu = 0.05$) because of SZM's much larger barotropic timestep.

The implicit schemes also have significant phase speed errors. We note that SZM's phase speed error in Table 13 takes a large jump when the timestep is increased from 3600 to 7200 s. This is due to poor resolution of the inertial period with $\Delta t = 7200$ s, which adds to the gravity-wave propagation error. Since SZM uses leapfrog and ECOM-si uses a two-time-level temporal scheme, SZM's timestep is effectively twice as large as ECOM-si's for the same value of Δt, which means that SZM feels the effect of poor resolution of the inertial period sooner than ECOM-si as Δt is increased.

The bottom of Table 13 shows errors from additional runs made with ECOM-si and SZM for the case $\Delta x = 40$ km, with Δt reduced from 7200 s to 360 s, i.e., to the value of Δt_e used by POM. With this large reduction of the timestep, the errors are significantly reduced, as expected. With $\Delta t = 360$ s, SZM's errors are about the same as POM's. With $\Delta t = 360$ s, ECOM-si's phase speed error is small, but the damping by the fully implicit treatment of the surface waves is still high.

From these results, it can be summarized that error in propagating long-wavelength surface Kelvin waves with these models on coarse grids will be due mainly to temporal truncation error.

7.2 Internal Kelvin Waves

The linearized equations for long (hydrostatic), internal Kelvin waves propagating along a coast in the x-direction in a linearly salt-stratified sea (with temperature constant) are

$$\frac{\partial u}{\partial t} = fv - \frac{1}{\rho_o}\frac{\partial p}{\partial x}, \tag{88}$$

$$\frac{\partial v}{\partial t} = -fu - \frac{1}{\rho_o}\frac{\partial p}{\partial y}, \tag{89}$$

$$\frac{\partial p}{\partial z} = -\rho g, \tag{90}$$

$$\frac{\partial S}{\partial t} = \frac{N^2}{\beta g} w, \tag{91}$$

$$\frac{\partial u}{\partial x} + \frac{\partial v}{\partial y} + \frac{\partial w}{\partial z} = 0. \tag{92}$$

The analytical solution of these equations is

$$u = A\frac{\omega m}{k} e^{-y/r} \cos(mz) \cos(kx - \omega t), \tag{93}$$

$$v = 0, \tag{94}$$

$$w = A\omega e^{-y/r} \sin(mz) \sin(kx - \omega t), \tag{95}$$

$$S' = A\frac{N^2}{\beta g} e^{-y/r} \sin(mz) \cos(kx - \omega t), \tag{96}$$

where A is the maximum amplitude of the vertical displacement and S' is the deviation of the salinity from the background stratification. The dispersion relation for the Kelvin waves is

$$\omega = \frac{Nk}{m}, \tag{97}$$

where $m = n\pi/H$ is the vertical wavenumber and n is the vertical mode number. Hence, the phase speed is

$$c = \frac{\omega}{k} = \frac{N}{m} = \frac{NH}{n\pi}. \tag{98}$$

The properties of internal Kelvin waves are similar to the properties of surface Kelvin waves: (a) the cross-shore component of the velocity is zero, (b) the amplitude of the waves decreases exponentially away from the coastal boundary, (c) the phase speed of internal Kelvin waves is the same as for freely propagating internal waves in the absence of rotation and does not depend on f, (d) the waves for a particular vertical mode are nondispersive, and (e) the waves propagate only in one direction, with the coast on the right in the Northern Hemisphere and on the left in the Southern Hemisphere.

The cross-shore scale of the internal Kelvin waves, which derives from the need to balance the Coriolis term and the cross-shore pressure gradient in the v-equation, is

$$r = \frac{\omega}{kf} = \frac{c}{f}. \tag{99}$$

For internal waves, the distance r is referred to as the internal Rossby radius of deformation. Since the phase speed of internal waves is much smaller than the phase speed of surface waves, the cross-shore length scale of the internal Kelvin waves is much smaller than that for surface Kelvin waves.

For the model tests of internal Kelvin wave propagation, the parameters used were the same as those used in the internal wave tests, i.e., the depth H was 40 m, temperature was a constant 20°C, and a linear salinity stratification was imposed with a surface salinity of 30 psu and a bottom salinity of 40 psu. The latitude was 29.91° N. With these values, $N = 0.0426$ 1/s, $c = 54.3$ cm/s, and $r = 7.46$ km. The along-channel wavelength of the waves was taken to be 64 km. The amplitude A of the Kelvin waves, which is the maximum vertical displacement of the isohalines at the coast, was initialized to a value of 1 m.

With the above parameters, the phase speed of the internal Kelvin waves is 54.25 cm/s. This is the same as the phase speed of freely propagating internal waves in the absence of rotation, and is 20% slower than the speed of freely propagating internal waves with $f = 2/\pi/(24\text{ h})$ (Table 9).

Table 14 shows errors for the propagation of internal Kelvin waves with the models for various values of horizontal grid resolution and timestep. These errors can be compared with those in

Table 14 — Comparison of Errors in the Salinity Anomaly Field S' for the Propagation of First-Mode Internal Kelvin Waves for a Value of f Corresponding to 29.91° N. The Correlation and RMS Error are at 48 h. The Errors are Calculated Only Over the Part of the S' Field Out to Two Rossby Radii from the Southern Boundary.

MODEL	Δx (km)	Δt (s)	Δt_e (s)	$\frac{\Delta t C}{\Delta x}$	WAVELENGTH (km)	PTS PER WAVE	SPEED ERROR (%)	DAMP TIME (h)	COR	RMS ERROR (cm)
POM	1	200	10	0.11	32	32	–0.6	1800	0.99994	0.0017
POM	4	800	40	0.11	32	8	–3.0	500	0.99975	0.0059
POM	8	1600	80	0.11	32	4	–10.0	300	0.99410	0.0112
ECOM	1	200	200	0.11	32	32	–0.4	3500	0.99986	0.0013
ECOM	4	800	800	0.11	32	8	–2.6	500	0.99948	0.0064
ECOM	8	1600	1600	0.11	32	4	–9.9	250	0.99309	0.0124
SZM	1	200	200	0.11	32	32	–0.5	1800	0.99948	0.0025
SZM	4	800	800	0.11	32	8	–2.8	600	0.99975	0.0047
SZM	8	1600	1600	0.11	32	4	–9.9	360	0.99421	0.0086
ECOM	1	800	800	0.43	32	32	–0.3	3500	0.99764	0.0042
SZM	1	800	800	0.43	32	32			unstable	

Table 12 for freely propagating internal waves, which were run with the same parameter values. For all the models, the phase speed error and damping are slightly lower for the Kelvin waves than for the freely propagating internal waves.

It must be noted that the internal Kelvin waves propagate quite well, even with very coarse resolution of the cross-channel structure. For example, the case with $\Delta x = 8$ km provides only one point within the first Rossby radius ($r = 7.46$ km) of the southern boundary of the channel.

Figure 25 shows plots of velocity vectors and S' from the analytical solution for the internal Kelvin waves at 48 h. The plot of u is for the surface layer (1.25-m depth) and the plot of S' is for the middle of layer 8 (18.75-m depth). These plots illustrate the horizontal and vertical structure of a mode 1 internal Kelvin wave.

Figure 26 shows S' from the models at 48 h for the case with $\Delta x = 4$ km and $\Delta t = 800$ s. It can be seen that the results from the models are very similar and agree well with the analytical solution (Fig. 25c), except for a slight phase lag and a small amount of damping.

7.3 Barotropic Shelf Waves

Barotropic shelf waves are also referred to as topographic waves or topographic Rossby waves. Their propagation depends on the Earth's rotation and the change in the absolute vorticity of the water column as the bottom depth changes. Hence, rotation and changes in bottom depth are both required for their existence. A distinction between these waves and planetary Rossby waves is that the existence of planetary Rossby waves depends on the latitudinal variation of the Coriolis parameter rather than changes in depth.

The linearized equations for barotropic shelf waves propagating in the x-direction along a straight coast are similar to those for surface Kelvin waves, except the depth H must vary with y. Also, to simplify the analytic solution, the time derivative of the surface elevation is scaled out of the continuity equation. This is permissible because this term is small and is not essential to the physics of small-amplitude, topographic waves. The equations are then

$$\frac{\partial u}{\partial t} = fv - g\frac{\partial \zeta}{\partial x}, \tag{100}$$

$$\frac{\partial v}{\partial t} = -fu - g\frac{\partial \zeta}{\partial y}, \tag{101}$$

$$0 = -H\frac{\partial u}{\partial x} - \frac{\partial Hv}{\partial y}. \tag{102}$$

The analytical solution of this set of equations is simplified for certain choices of the function $H(y)$. One possible choice is the function

$$H(y) = H_o e^{2\alpha y}, \tag{103}$$

where H_o is the depth at the coast and α defines the cross-channel scale of the change in water depth. With the bathymetry given by (103), the analytic solution of (100–102) is (LeBlond and Mysak 1978)

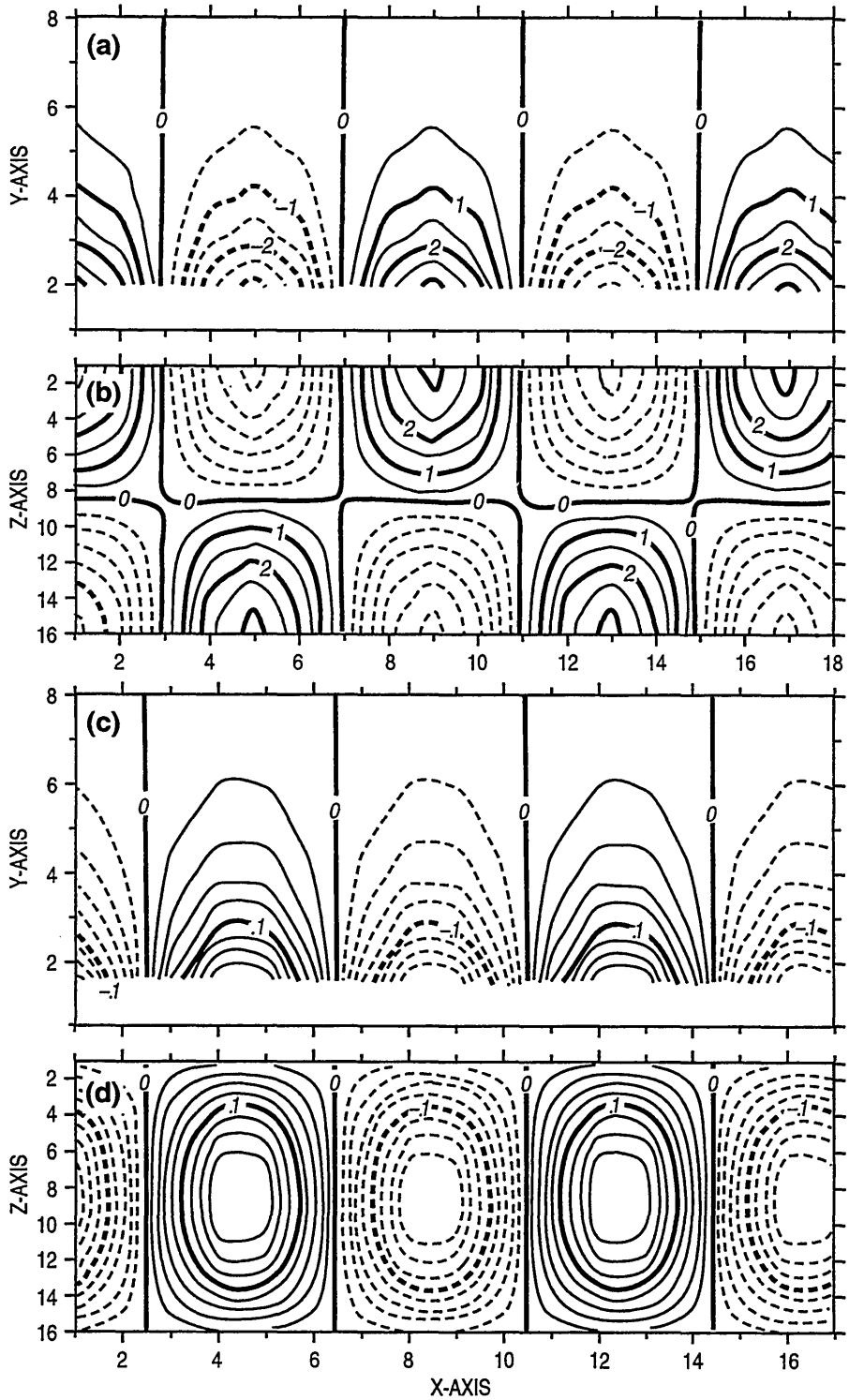

Fig. 25 — Analytical solution for an internal Kelvin wave at 48 h: (a) horizontal section of along-channel velocity u at 1.25-m depth, (b) x-z section of u at 4 km from southern boundary, (c) horizontal section of salinity anomaly S' at depth of 18.75 m, and (d) x-z section of S' at 4 km from southern boundary. Contour interval is 1.0 cm/s for u and 0.02 psu for S'.

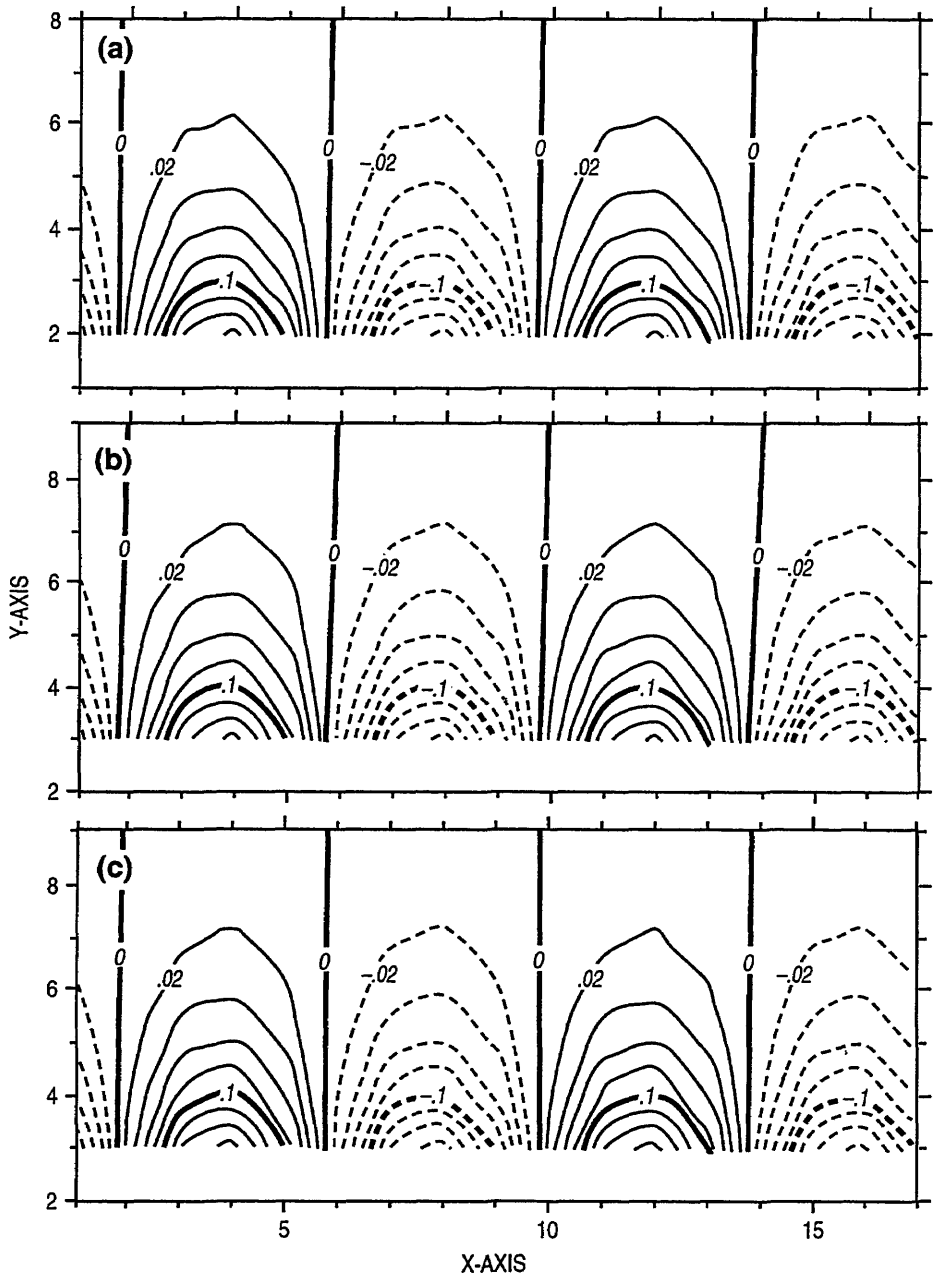

Fig. 26 — Comparison of horizontal section of salinity anomaly S' from models at 48 h for propagation of internal Kelvin wave for case with 4-km grid spacing and 800-s timestep: (a) POM, (b) ECOM-si, and (c) SZM. The horizontal section is at the center of the eighth model layer at a depth of 18.75 m. Contour interval is 0.02 psu.

$$\zeta = \frac{A}{gk} e^{-\alpha y} ((\omega\alpha - fk) \sin(ly) + \omega l \cos(ly) \cos(kx - \omega t)) , \tag{104}$$

$$u = Ae^{-\alpha y} (\alpha \sin(ly) + l \cos(ly)) \cos(kx - \omega t) , \tag{105}$$

$$v = Ake^{-\alpha y} \sin(ly) \sin(kx - \omega t) , \tag{106}$$

where A scales the amplitude of the waves. The dispersion relation for the shelf waves is

$$\omega = \frac{2\alpha kf}{k^2 + l^2 + \alpha^2} . \tag{107}$$

The cross-shore wavenumber l is restricted to the values $l = n\pi/L_y$ (where $n = 1, 2, 3,...$ is the cross-channel mode number) so as to satisfy the condition of zero flow normal to the walls of the channel. The phase speed is then

$$c = \frac{\omega}{k} = \frac{2\alpha f}{k^2 + l^2 + \alpha^2} . \tag{108}$$

There is a lot of freedom in defining parameters for shelf waves. The bathymetry, channel width, and along-shore wavelength can all be specified independently, and for each set of these values, there is an infinite number of modes in the cross-channel direction.

For the model tests, the depth at the coast H_o was taken to be 20 m and the cross-channel e-folding scale of the bathymetry was taken to be $(2\alpha)^{-1} = 40$ km. The width of the channel L_y was taken to be 64 km. Hence, the depth in the channel varies from 20 m at the coastal boundary to 99 m at the offshore boundary.

The models were initialized from the analytic solution (104–106) for a single mode in the cross-channel direction, and for an along-channel wavelength of 128 km. These parameters give a phase speed for the shelf wave of 36.54 cm/s. The amplitude A of the wave was taken to be 100 m^2/s, which gives a maximum amplitude of the surface elevation of about 0.05 cm and maximum velocities of about 0.5 cm/s. With these small amplitudes, the linear shelf wave can be propagated quite accurately by the models.

Table 15 shows the error in the cross-channel velocity from the models for horizontal grid resolutions ranging from 2 to 16 km. These grid resolutions provide from 64 to 8 points per wavelength in the along-channel direction and from 32 to 4 points in the cross-channel direction. The surface elevation and velocity calculated from the analytical solution at 48 h are shown in Fig. 27, and a comparison of the cross-channel velocity fields from the models at 48 h for the case with $\Delta x = 8$ km is shown in Fig. 28. The cross-channel velocity from the models can be compared with the analytically calculated cross-channel velocity shown in Fig. 27.

The errors in Table 15 increase as the resolution of the wave decreases, as expected. With 64 points per wavelength, the shelf wave is propagated very accurately with little phase error and a damping timescale that exceeds 2 y. With 8 points per wavelength and only 4 points in the cross-channel direction, the wave is still propagated fairly well, except that the phase speed has a large error.

Table 15 — Comparison of Errors in the Cross-Channel Velocity for the Propagation of Barotropic Shelf Waves for a Value of f Corresponding to 29.91° N. The Correlation and RMS Error are at 48 h. The RMS Error is About 0.39 cm/s when the Model Solution is Fully Damped.

MODEL	Δx (km)	Δt (s)	Δt_e (s)	$\frac{\Delta t_e C}{\Delta x}$	WAVELENGTH (km)	PTS PER WAVE	SPEED ERROR (%)	DAMP TIME (h)	COR	RMS ERROR (cm)
POM	2	400	20	0.004	128	64	–0.76	41000	0.99995	0.0017
POM	4	800	40	0.004	128	32	–2.4	60000	0.99998	0.0010
POM	8	1600	80	0.004	128	16	–9.1	30000	0.99998	0.0013
POM	16	3200	160	0.004	128	8	–33.4	15000	0.99996	0.0021
ECOM	2	400	400	0.07	128	64	0.4	56000	0.99998	0.0022
ECOM	4	800	800	0.07	128	32	0.1	80000	0.99999	0.0043
ECOM	8	1600	1600	0.07	128	16	–4.2	22000	0.99999	0.0084
ECOM	16	3200	3200	0.07	128	8	–25.8	8000	0.99999	0.0164
SZM	2	400	400	0.07	128	64	–0.77	18000	0.99999	0.0010
SZM	4	800	800	0.07	128	32	–2.5	9000	0.99999	0.0012
SZM	8	1600	1600	0.07	128	16	–9.1	4000	0.99999	0.0020
SZM	16	3200	3200	0.07	128	8	–33.2	2000	0.99999	0.0040

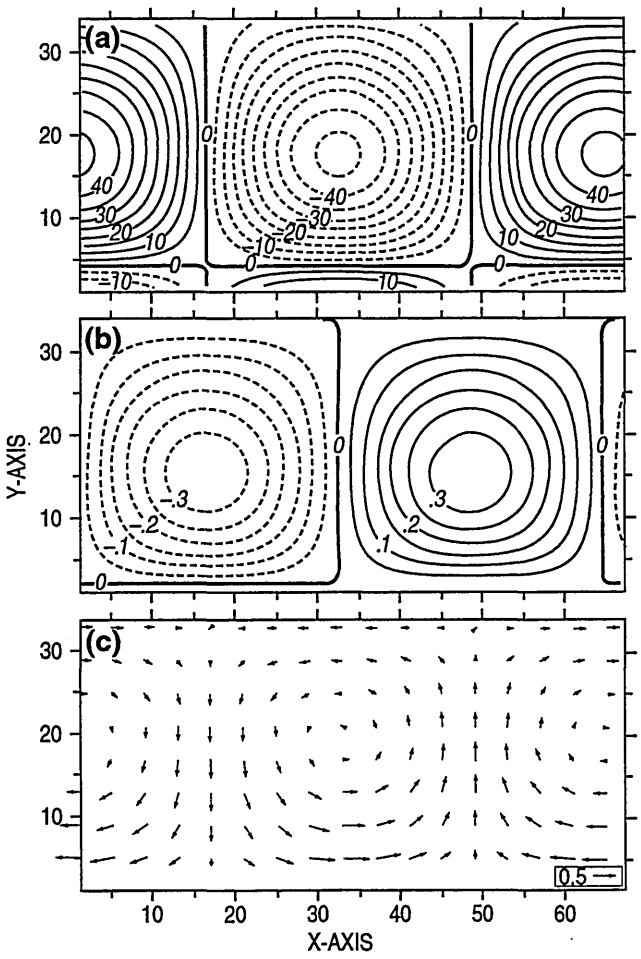

Fig. 27 — Analytical solution for a barotropic shelf wave at 48 h: (a) surface elevation, (b) cross-channel velocity, and (c) horizontal velocity vectors. The contour interval for the surface elevation is 0.005 cm and for the cross-channel velocity is 0.05 cm/s. The scaling arrow in the velocity vector plot indicates a speed of 0.5 cm/s.

With ECOM-si, the cross-channel velocity field increased in amplitude at the beginning of the shelf wave simulations and then decreased slowly. The initial increase ranged from 1.3% for $\Delta x = 2$ km to 10% for $\Delta x = 16$ km. The cause of the increase was not determined. The amount of the initial increase was not affected by the timestep and the initial fields used were checked against those used for the other models. Note that the damping timescale in Table 15 reflects only the decrease in the wave amplitude after the initial increase. The RMS error for ECOM-si in Table 15 does, however, reflect the initial increase, and this is the reason it is larger than the RMS error for the other models.

Simulation of the shelf waves with ECOM-si with the original, lagged treatment of the Coriolis terms was also tried. With this treatment of the Coriolis terms, the amplitude of the shelf waves increased steadily with time. The increase at 48 h was 2.5% with $\Delta x = 2$ km and Δt=400 s and was 9.2% with $\Delta x = 8$ km and $\Delta t = 1600$ s.

All the simulations of the barotropic shelf waves discussed so far have used sigma vertical coordinates. Some additional simulations were conducted with SZM to investigate the propagation of the barotropic shelf wave using z-levels. Figure 29 shows results at 48 h using SZM with $\Delta x = 2$ km (64 points per wavelength) and 10 uniformly spaced z-levels ($\Delta z = 10$ m). The results look quite noisy compared with the analytical solution in Fig. 27 and with the sigma coordinate simulations in Fig. 28 with significantly less horizontal and temporal resolution. A problem here is that with the bathymetry truncated to the nearest model level in SZM, the specified bathymetry (103) is not very well resolved.

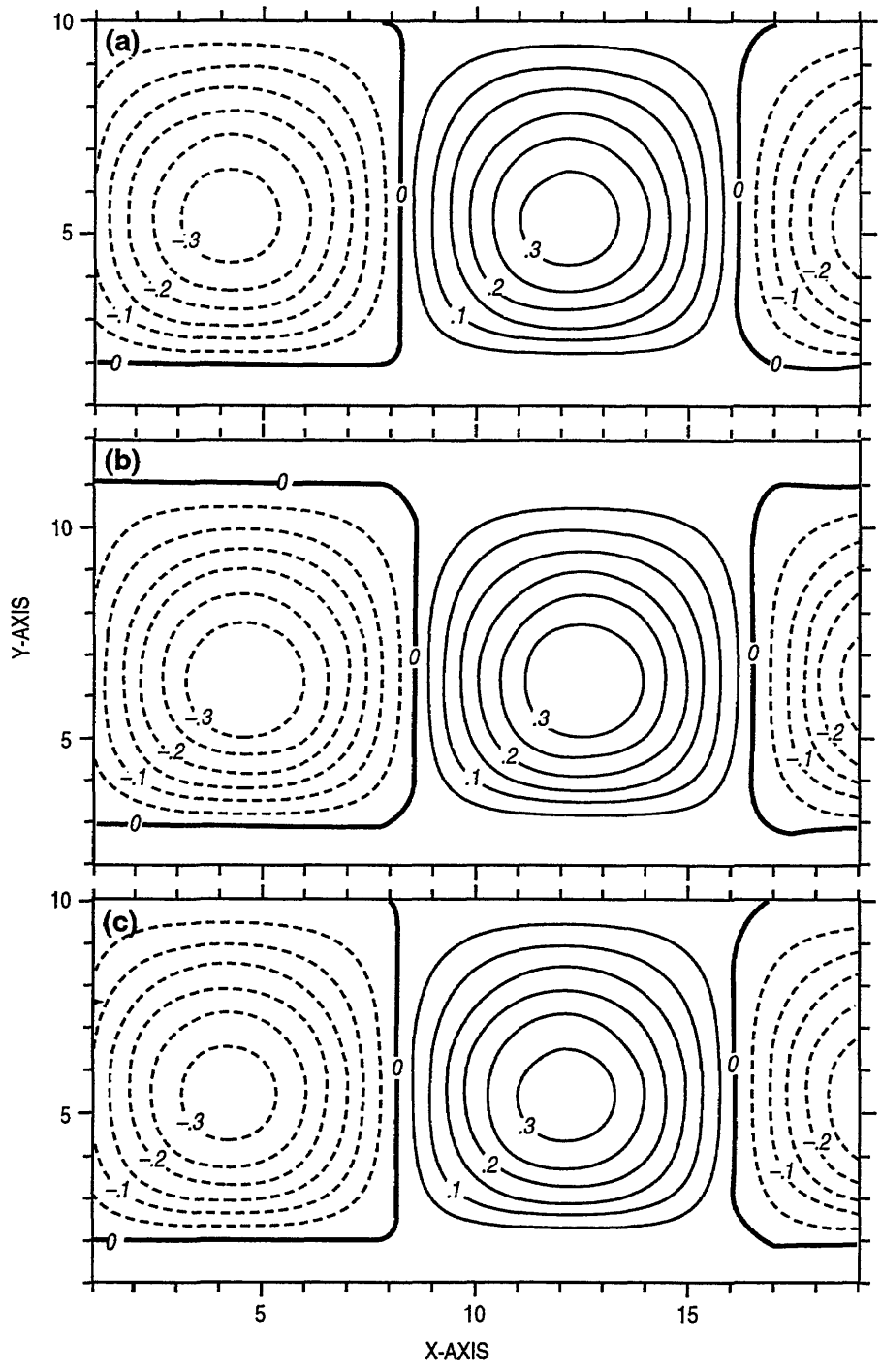

Fig. 28 — Comparison of the cross-channel velocity fields at 48 h from the models for the propagation of a barotropic shelf wave: (a) POM, (b) ECOM-si, (c) SZM. The horizontal grid spacing for the models is 8 km, and the barotropic timestep is 80 s for POM and 1600 s for ECOM-si and SZM. The contour interval is 0.05 cm/s.

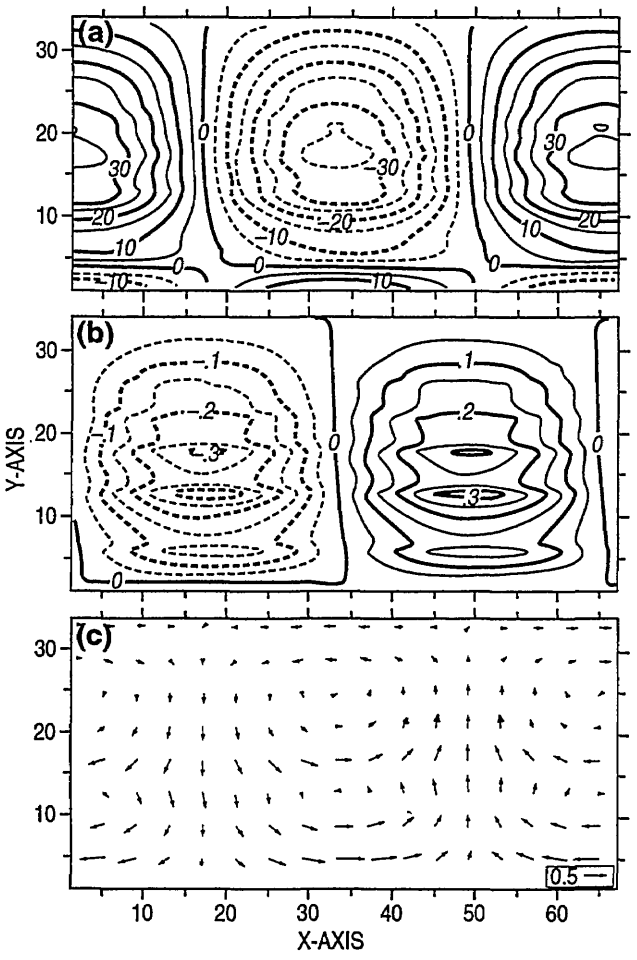

Fig. 29 — (a) Surface elevation, (b) cross-channel velocity, and (c) horizontal velocity vectors at 48 h for a shelf wave simulated by SZM with a z-level vertical grid with $\Delta z = 10$ m. The horizontal grid spacing is 2 km and the timestep is 400 s. The contour interval is 0.005 cm for the surface elevation and 0.05 cm/s for the cross-channel velocity. The representative scaling arrow in the velocity vector plot indicates a speed of 0.5 cm/s.

What SZM does (approximately) is propagate the shelf wave that is consistent with the step-wise bathymetry that is used with the model rather than the shelf wave derived for the smooth, exponentially varying bathymetry that was used to calculate the analytical solution. Figure 30 shows the analytical solution (see App C for the derivation) for the cross-shelf velocity for the step-wise bathymetry used in the SZM model simulation in Fig. 29. The analytical solution for the step-wise bathymetry looks much like the model solution for the step-wise bathymetry.

Figure 31 shows results for the cross-channel velocity at 48 h for simulations conducted with SZM with z-levels with finer vertical grid resolution, i.e., with (a) 30 uniformly spaced z-levels ($\Delta z = 3.33$ m), (b) 60 uniformly spaced z-levels ($\Delta z = 1.67$ m), and (c) 51 z-levels with a vertical stretching of the grid employed so as to exactly resolve the bathymetry represented by (103). Errors for these simulations are reported in Table 16. From Fig. 31 and Table 16, it can be seen that the shelf wave propagated on the z-level grid becomes more like the analytical solution for the smoothly varying bathymetry when the true bathymetry is more accurately represented.

The best solution with the z-level grids is obtained with the stretched grid of 51 points that was set up to exactly resolve the bathymetry. However, the errors for this case (Table 16) are still larger than the errors obtained for the simulations with sigma coordinates, and the damping is significantly greater than the damping for the simulations with sigma coordinates (Table 15). A problem with the z-level grid, besides difficulty in resolving the bathymetry, is interaction of the horizontal

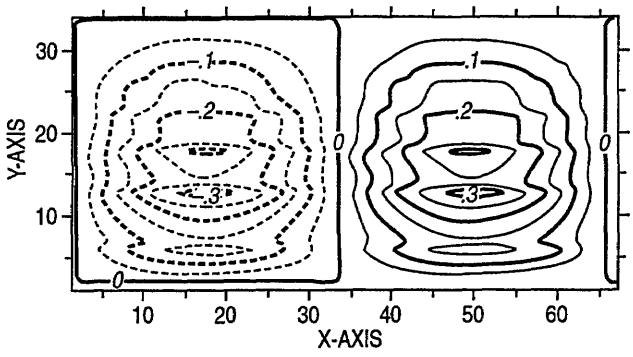

Fig. 30 — Analytically calculated cross-channel velocity field for a barotropic shelf wave propagating along step-wise bathymetry. The step-wise bathymetry is the same as that used by the SZM shelf-wave simulation with a z-level grid with $\Delta z = 10$ m.

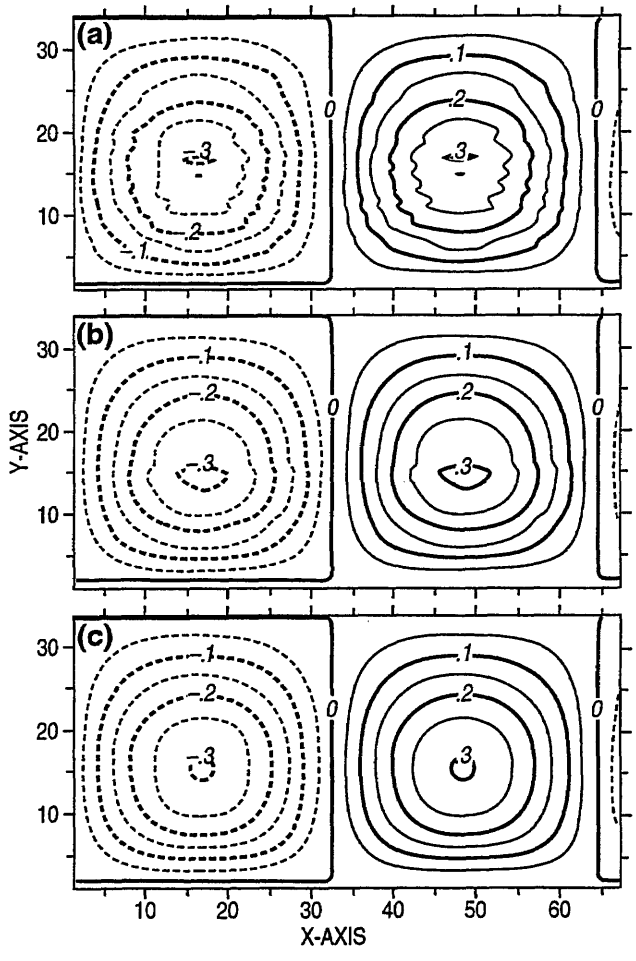

Fig. 31 — Cross-channel velocity fields at 48 h for the propagation of a barotropic shelf wave with SZM for different z-level vertical grids: (a) 30 uniformly spaced z-levels, (b) 60 uniformly spaced z-levels, and (c) 51 z-levels with variable spacing so as to exactly resolve the exponentially varying bathymetry. The horizontal grid spacing for these results is 2 km and the timestep is 400 s.

Table 16 — Errors in the Cross-Channel Velocity for the Propagation of Barotropic Shelf Waves Using SZM with Different z-Level Vertical Grids. The Grid with 51 z-Levels is Stretched so as to Match the Exponentially Varying Bathymetry Exactly. Horizontal Resolution for all the Runs is 64 Points Per Wave with $\Delta x = 2$ km, $\Delta t = 400$ s.

VERTICAL GRID	Δz (m)	SPEED ERROR (%)	DAMP TIME (h)	COR	RMS ERROR (cm/s)
10 Uniform z-Levels	10.00	1.6	200	0.95540	0.0548
30 Uniform z-Levels	3.33	–1.0	300	0.98777	0.0339
60 Uniform z-Levels	1.67	0.5	330	0.99862	0.0240
51 Stretched z-Levels	variable	–0.5	330	0.99998	0.0225

currents with the bathymetry steps near the bottom. Two consequences of this interaction, relative to the sigma coordinate simulations, are that the damping is greater and the horizontal currents are not barotropic near the bottom.

8.0 TEST FORMATION OF UPWELLING/DOWNWELLING FRONTS

The models were compared for the formation of upwelling and downwelling fronts using a 2-D model domain with idealized geometry. Similar upwelling and downwelling problems have recently been investigated by Allen et al. (1995) and Allen and Newberger (1996) with POM.

Figure 32 shows the model domain, which consists of a symmetric, 2-D basin with gently sloping shelves on both the east and west sides out to 100 km, steeper slope regions from 100 km out to 200 km, and an interior of depth 1000 m. The depth at the shelf break is 100 m and the total width of the basin is 604 km. To avoid "drying" of the shallowest points near the coast, the minimum static bottom depth was set to 5 m. The gradients of the bottom slope along the shelf and slope regions are 0.001 and 0.009, respectively.

The models were run in "pseudo 2-D" mode for this problem, with periodic boundary conditions and two interior points in the along-shore (y) direction.

The initial condition consists of a horizontally uniform thermal stratification (Fig. 32) with the ocean at rest. The initial SST is 20°C and most of the thermal stratification lies between 50- and 100-m depth. Salinity is set to a constant 35 psu. The forcing consists of a uniform, along-shore, northward-directed surface wind stress of 2 dynes/cm^2. The wind stress is ramped up linearly in time over 24 h. Surface heat fluxes are zero. All the results presented are at 40 d.

The models were run at two different grid resolutions. One set of simulations was conducted with a 2-km horizontal grid and 50 vertical layers/levels with a 5-m-thick layer at the surface in the deep water and uniform stretching to the bottom. For the second set of simulations, the horizontal resolution was reduced to 10 km and the vertical grid was reduced to 20 layers/levels with a surface layer thickness in the deep water of 10 m and a uniform stretching to the bottom.

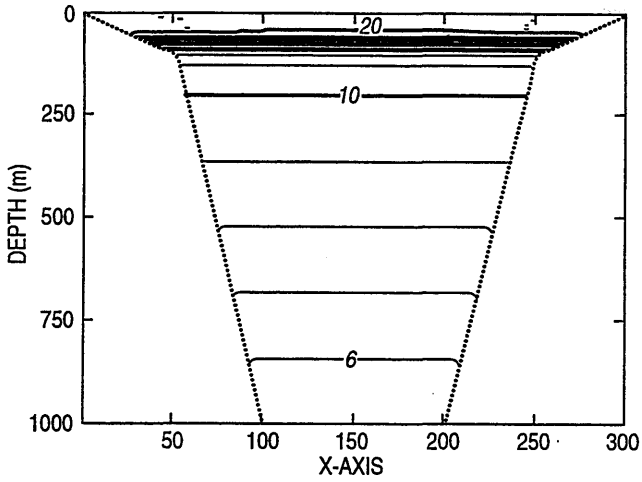

Fig. 32 — Model domain and initial temperature field for upwelling/downwelling simulations

Figure 33 shows temperature and along-shore velocity at 40 d for the model simulations with the 2-km grid and 50 vertical sigma layers. Table 17 lists the minimum SST on the upwelling side, the maximum SST on the downwelling side, and the maximum along-shore currents. The northward wind stress induces upwelling on the west side of the domain and downwelling on the east side. Strong along-shore currents develop that are in approximate geostrophic balance with the cross-shore pressure gradients. The temperature sections show good general agreement. A curious feature that appears in the simulations is a sharp rise in the isotherms just seaward of the shelf break on the downwelling side. This is caused by vertical mixing, which is enhanced at this location by the strong shears in the along-shore current.

The velocity sections show maximum along-shore currents of 130–140 cm/s on the upwelling side and 190–200 cm/s on the downwelling side (Fig. 33, Table 17). The maximum currents are located just seaward of the shelf break. As in the experiments of Allen (1995, 1996), the along-shore current on the upwelling side is a maximum at the surface and decreases with depth, whereas on the downwelling side, the maximum current extends quite deep. The along-shore currents for the models agree quite well.

Figure 34 shows temperature and along-shore velocity for the simulations with the 10-km grid. The accuracy of the 10-km simulations can be judged based on the 2-km results. The upwelling front is more diffuse and the along-shore currents are weaker for the 10-km simulations because of the reduced grid resolution and the resulting stronger horizontal mixing. The weakest currents in the 10-km simulations are for ECOM-si. The 10-km simulation with ECOM-si was rerun with the timestep reduced from 1200 to 200 s to see how much difference might be due to temporal truncation error. However, with the smaller timestep, the currents were only slightly higher (Table 17).

A notable occurrence in all the sigma coordinate simulations is the warming of the near-surface water above the initial SST of 20°C on the outer part of the shelf on the downwelling side. This warming cannot really be ascertained in Figs. 33 and 34 because of the shortage of contour labels. However, the warming can be seen in Fig. 35a, which shows an expanded view of the temperature field in the downwelling area from the 10-km simulation with POM. Also, the maximum SST values at 40 d for all the runs are reported in Table 17.

Since there is no explicit heating in these simulations, we should expect that the temperatures at 40 d would not exceed the initial maximum temperature of 20°C. However, the maximum

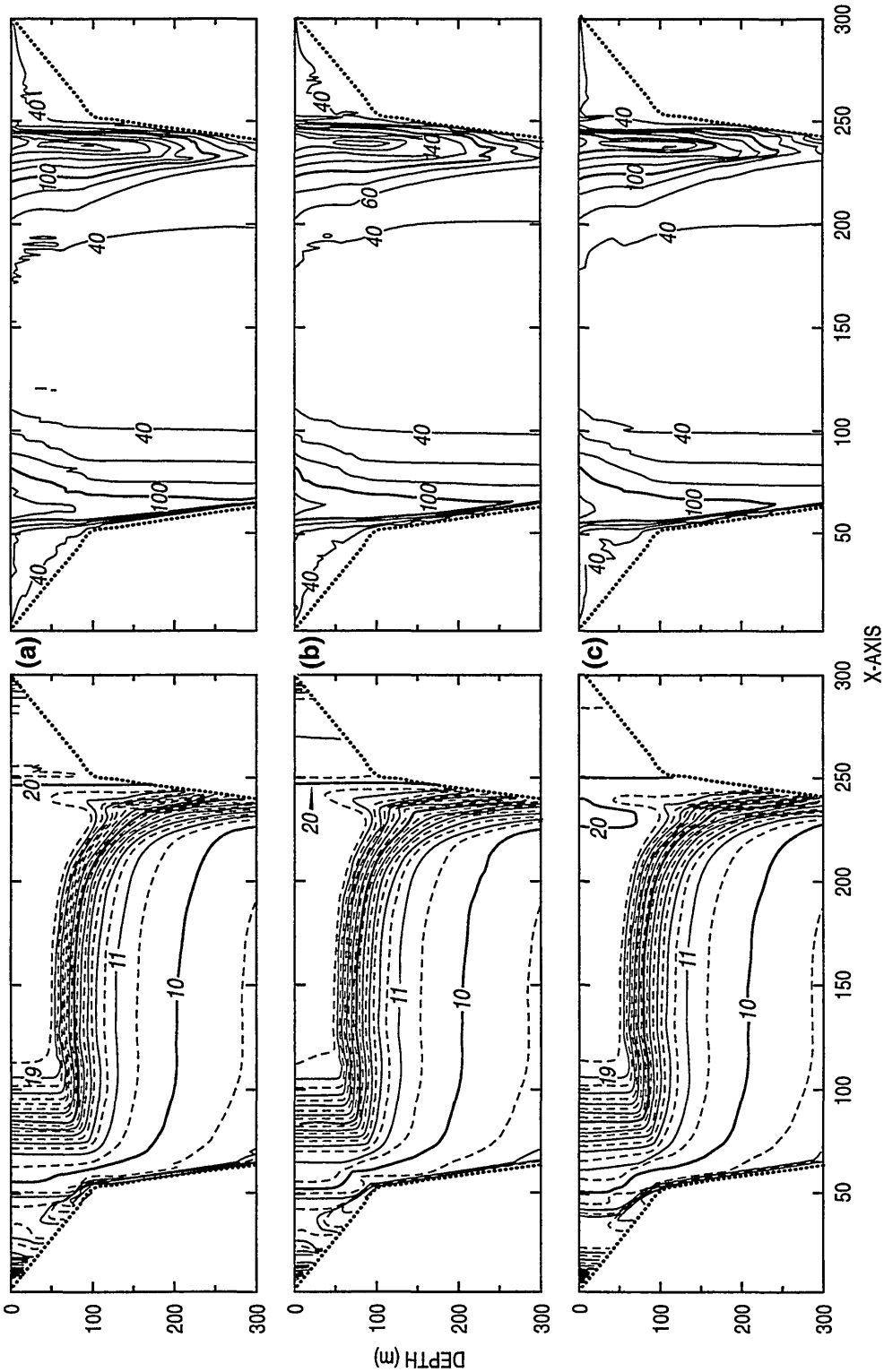

Fig. 33 — Temperature and along-channel velocity at 40 d for the formation of upwelling and downwelling fronts with (a) POM, (b) ECOM-si, and (c) SZM with a horizontal grid resolution of 2 km. 50 sigma layers are used in the vertical.

Table 17 — Results from Upwelling Downwelling Experiments at 40 d

			UPWELLING SIDE		DOWNWELLING SIDE	
MODEL	Δx (km)	Δt (s)	MIN SST (°C)	MAX V (cm/s)	MAX SST (°C)	MAX V (cm/s)
Results with Sigma Coordinate Grid						
POM	2	200	8.4	138	20.5	202
ECOM	2	200	8.3	135	20.9	190
SZM	2	200	7.8	131	20.5	202
POM	10	1200	8.9	108	22.2	170
ECOM	10	1200	9.4	94	22.4	143
SZM	10	1200	8.4	103	22.0	162
ECOM	10	200	9.7	96	22.3	146
Results with z-Level Grid						
SZM	2	1200	8.4	132	20.0	200
SZM	10	1200	10.2	86	20.2	156

temperature on the downwelling shelf at 40 d is 20.5–20.9°C for the 2-km simulations and 22.0–22.4°C for the 10-km simulations (Table 17). This spurious heating is caused by the procedure that was used for horizontal diffusion of T and S in which the horizontal mean profile is subtracted from the T and S fields when performing horizontal diffusion in sigma coordinates (this is discussed in Sec. 2.9). The anomaly from the horizontal mean temperature profile in the downwelling area is shown in Fig. 35b and is a maximum of 7–8°C at the outer edge of the shelf. This large, positive anomaly diffuses heat in all directions and the diffusion toward the shelf causes the warming of the water on the shelf. The spurious warming is reduced as the horizontal grid resolution is increased because the horizontal diffusion coefficients are reduced.

This illustrates a pitfall of subtracting the horizontal mean profile from a field when performing horizontal diffusion in sigma coordinates. It might be preferable, instead, to subtract a smooth but horizontally varying field that would be able to account for large departures from the basin horizontal mean. Such a field would have to be recomputed periodically if it changes significantly in time. This procedure was not tried here, but has been used by other sigma-coordinate modelers. It is noted that in POM, the arrays used to hold the smoothed values of T and S that are subtracted from the T and S fields when performing horizontal diffusion are most recently referred to as "climate fields" (Mellor 1996), which suggests fields that have 3-D structure, but are spatially smooth. A general concern with such methods would be to avoid spurious development of the field that might be caused by "steering" the field via the diffusion term towards some computed "mean" structure, especially if that mean is recomputed periodically from the evolving fields.

The upwelling/downwelling simulations with 2- and 10-km horizontal resolution were repeated with SZM with a z-level vertical coordinate. The z-level grids were set up to have the same vertical resolution in the deep water as the sigma coordinate grids. Figure 36 shows plots of temperature and along-shore velocity with SZM with the z-level grids, and Table 17 lists the maximum and minimum SST and the maximum along-shore currents. With 2-km horizontal resolution and 50 vertical

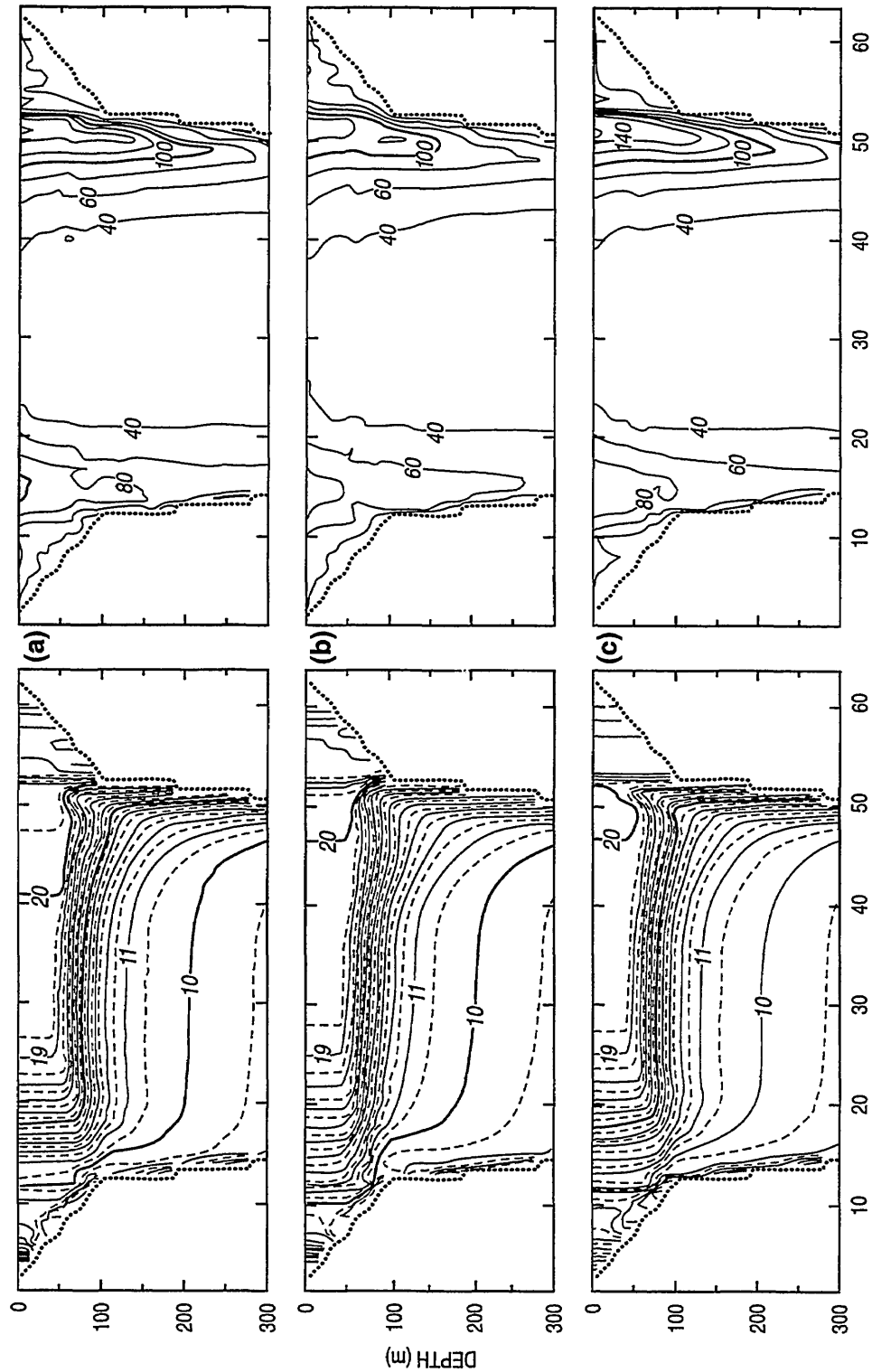

Fig. 34 — Temperature and along-channel velocity at 40 d for the formation of upwelling and downwelling fronts with (a) POM, (b) ECOM-si, and (c) SZM with a horizontal grid resolution of 10 km. 20 sigma layers are used in the vertical.

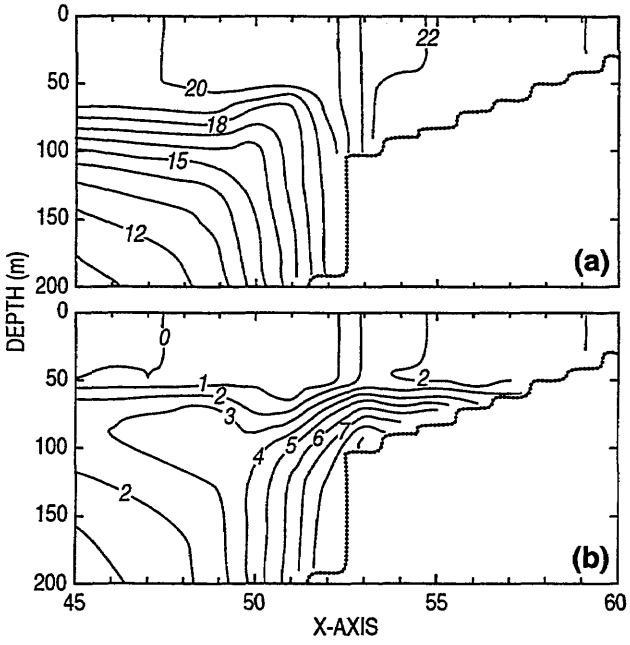

Fig. 35 — An expanded view of the temperature field in the downwelling area at 40 d from the 10-km simulation with POM. The temperature values are shown in (a) and the anomaly from the initial temperature profile is shown in (b).

layers, the results with SZM with z-level and sigma coordinates are fairly similar. The maximum along-shore currents are about the same (Table 17). The minimum SST on the upwelling side with z-levels (8.4°C) is greater than was obtained with SZM with sigma coordinates (7.8°C), though it is similar to the values obtained with POM and ECOM-si.

With 10-km horizontal resolution and 20 vertical layers, the differences between the SZM z-level and sigma coordinate results are larger, e.g., the along-shore current and cooling on the upwelling side show larger differences (Table 17). Some of the differences are due to reduced vertical resolution with the z-level grid in shallower water, which provides reduced resolution of both the model fields and the bathymetry. However, an experiment conducted with a 10-km grid with higher vertical resolution showed that some differences remained, i.e., some of the differences are due to other factors.

It can be noted that the spurious warming of the near-surface temperature that occurs on the downwelling shelf with sigma coordinates does not occur when z-levels are used. The maximum SST of 20.2°C that occurs in the 10-km simulation with z-levels is probably due to a small numerical advective "overshoot" that can occur at fronts with the second-order, centered advection schemes used in these models (Sec. 3.2).

The trends seen in these results illustrate what we might expect, that as grid resolution is increased, differences between simulations conducted with sigma and z-level coordinates tend to be reduced. At coarse resolution, the sigma and z-level coordinates each have particular advantages and disadvantages.

9.0 SUMMARY

Several ocean models that are being used for coastal ocean simulation and prediction, POM, ECOM-si, SZM, and SCRUM (Version 2.1) were tested for their ability to simulate physical processes

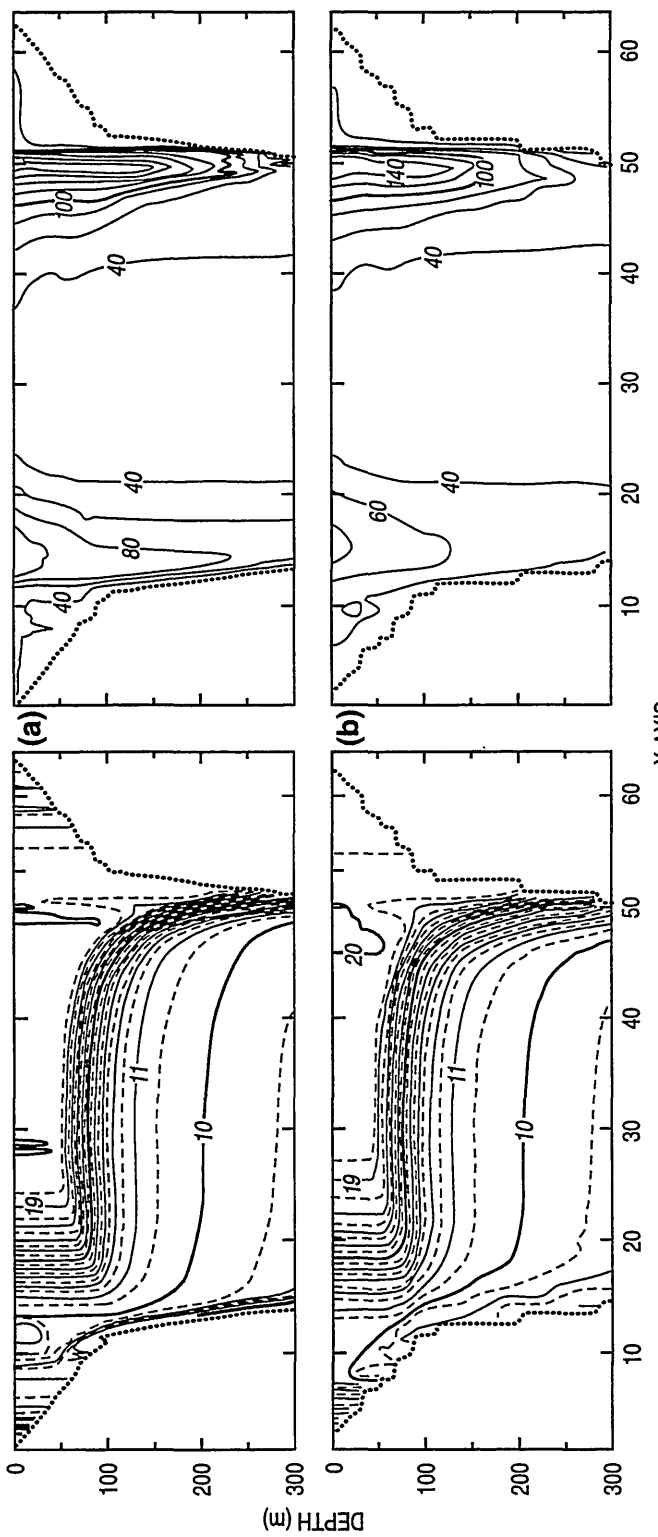

Fig. 36 — Temperature and along-channel velocity at 40 d for the formation of upwelling and downwelling fronts with SZM with a z-level vertical grid (a) $\Delta x = 2$ km and 50 layers and (b) $\Delta x = 10$ km and 20 layers. (Note that the two layers at the surface are sigma layers that are needed to accommodate surface elevation changes.)

of importance in the coastal ocean. The basic processes for which the models were tested included advection, vertical mixing, propagation of surface, internal, and coastal-trapped waves, and the formation of upwelling and downwelling fronts.

Because of some developmental problems with the version of SCRUM that we initially obtained, and the later release of an extensively modified SCRUM code (Version 3.0) by Rutgers, SCRUM was not included in many of the model tests that were conducted.

The model tests revealed some particular problems with the individual models, which will be briefly summarized here. In many cases, these are limitations that occur in certain situations. These problems and limitations should be kept in mind when applying the models or when selecting a model for a particular application.

The forward time-differencing scheme used by ECOM-si suffers from significantly higher temporal truncation error than the leapfrog and Adams-Bashforth schemes used by the other models. The forward treatment of the advection terms by ECOM-si is quite dispersive. The forward treatment of the Coriolis term is unstable in that it tends to cause the growth of inertial oscillations. This error is small and generally not noticeable with the small timesteps typically used in high-resolution coastal modeling, but can become significant when the timestep exceeds about 200 s. (The Coriolis term was converted to an Adams-Bashforth treatment to avoid this timestep limitation.) The forward time-differencing scheme in ECOM-si can also cause a modification of the ambient stratification during internal wave propagation. This is caused by numerical diffusion due to a phase (timing) error between the vertical velocity and the temperature and salinity values in the vertical advection terms of the temperature and salinity conservation equations.

The implicit treatment of the free surface in ECOM-si and SZM is much less accurate for the propagation of surface waves than the split-explicit scheme used by POM in terms of phase speed error and damping. The phase speed errors for ECOM-si and SZM are similar, but ECOM-si's fully implicit treatment of surface waves is significantly more damping than SZM's partially implicit treatment. We note, however, that with the high temporal and spatial grid resolution typically used in coastal modeling, ECOM-si and SZM generally simulate the tides fairly accurately since the long wavelength and period of the tides are well resolved. If coarse grids and large timesteps are used, the accuracy of tidal prediction with the implicit treatment of the free surface may be a concern.

Sigma vertical coordinates can suffer from problems with their horizontal advection, diffusion, and pressure gradient terms in regions of steep bathymetry. One problem that can occur is overshoot of the spatially centered advection term in the bottom layers at a steep bottom slope. This is due to the sharp change (i.e., "front") that can occur in the bottom sigma layers when a shallow point is right next to a deep point. Advection between the shallow point and the deep point can result in severe advective overshoot due to the large change in the advected field between the two points.

The practice of subtracting a spatially averaged profile from the temperature and salinity fields when calculating horizontal diffusion in sigma coordinates can result in significant spurious diffusion if the local temperature or salinity structure is much different from the mean profile that is subtracted. In a downwelling problem, the positive temperature anomaly in the downwelling region, relative to the mean temperature profile in the model domain, resulted in a spurious warming of the water shoreward of the downwelling area due to diffusion of heat from the downwelling area toward the shore.

Z-level grids also have particular shortcomings. If the bathymetry is truncated to the nearest *z*-level, as is done with a number of *z*-level models besides the SZM model that is included in this

study, the problem that the model actually solves is that for the stair-step bathymetry being used in the model, and not the problem for the true bathymetry that the stair-step bathymetry is approximating. (This may seem obvious, but there is a tendency to think in terms of the bathymetry one is modeling, rather than in terms of the bathymetry that is actually in the model.)

On-shore and offshore barotropic flows can be noticeably distorted by the stair-step approximation of a z-level grid. The horizontal convergence of the flow is focused at the faces of the stair-steps rather than being spread out over the region of decreasing depth, i.e., the flow in the model is the flow that would result if the step were actually present. In a problem with an on-shore, barotropic tidal flow, the isotherms were distorted by the vertical "jets" that occurred at the faces of the steps. In the real ocean, internal waves are generated by such tidal flows in regions where there are sharp bathymetric changes, but this should not happen in a region where the bathymetry is changing gradually. Topographic shelf waves, which depend on changes in bottom depth for their existence, can be quite distorted by a stair-step approximation to a smoothly varying bathymetry. The best solution to these problems with z-level vertical coordinates may be to truncate the bottom grid cell of the z-level grid to the bathymetry, rather than rounding the bottom depth to the nearest model level. This adds complication, but is being done in some z-level models.

The Crank-Nicolson scheme used for vertical mixing in SCRUM 2.1, where the values being diffused are evenly weighted at the old and new time levels, causes diffusive overshooting if the vertical diffusion coefficients are large, which they frequently are in realistic mixing situations. The result is that vertical gradients in the field being diffused (temperature, salinity, or velocity) can be reversed (or distorted) between adjacent vertical points. The computation does not blow up, but the resulting mixing can be noisy and inaccurate. All the other models use fully implicit vertical mixing, with the field being diffused weighted fully at the new time level, to avoid this problem.

Checkerboard mixing, where a fluctuation in the mixed-layer depth sets up at alternate gridpoints, was found to occur with the models under certain conditions of light to moderate winds and surface heating (or a positive surface buoyancy flux). The checkerboard mixing occurs because of the horizontal averaging that is used when computing vertical mixing on a C grid, where the velocity and the temperature-salinity points are at different locations. As a practical matter, checkerboard mixing is not usually seen in realistic simulations because of the temporal and spatial changes in the surface forcing that tend to suppress or mask the phenomenon.

10.0 ACKNOWLEDGMENTS

This work was supported by the Office of Naval Research through the Model Performance and Evaluation Task of the Naval Ocean Modeling and Prediction Program (Program Element 602435N), managed by Tom Curtin.

11.0 REFERENCES

Allen, J. S., P. A. Newberger, and J. Federiuk, "Upwelling Circulation on the Oregon Continental Shelf, Part I: Response to Idealized Forcing," *J. Phys. Oceanog.* **25**, 1843–1866 (1995).

Allen, J. S. and P. A. Newberger, "Downwelling Circulation on the Oregon Continental Shelf, Part 1: Response to Idealized Forcing," *J. Phys. Oceanog.* **26**, 2011–2033 (1996).

Anderson, D. and B. Gattahi, "A Comparison of Numerical Solutions of the Advective Equation," *J. Atm. Sci.* **31**, 1500–1506 (1974).

Arango, H., pers. comm.

Asselin, R., "Frequency Filter for Time Integrations," *Mon. Wea. Rev.* **100**, 487–490 (1972).

Blumberg, A. F. and G. L. Mellor, "A Description of a Three-Dimensional Coastal Ocean Circulation Model," in *Three-Dimensional Coastal Ocean Models*, N. Heaps (ed.), American Geophysical Union, New York, NY, 1987, 208 pp.

Blumberg, A. F., *A Primer for ECOM-si* (HydroQual, Inc., Mahwah, NJ, 1992), 64 pp.

Cantekin, M. E. and J. J. Westerink, "Non-Diffusive N+2 Degree Petrov-Galerkin Methods for Two-Dimensional Transient Transport Computations," *Int. J. Numer. Methods. Eng.* **30**, 397–418 (1990).

Casulli, V. and R. T. Cheng, "Solutions of Primitive Equations for Three-Dimensional Tidal Circulation," Estuarine and Coastal Modeling III, Proceedings of the 3rd International Conference, ASCE, New York, NY, 1993, pp. 396–406.

Clancy, R. M., "A Note on Finite Differencing of the Advection-Diffusion Equation," *Mon. Wea. Rev.* **109**, 1807–1809 (1981).

Crowder, H. J. and C. Dalton, "Errors in the Use of Non-Uniform Mesh Systems," *J. Comp. Phys.* **7**, 32–45 (1971).

Crowley, W. P., "Numerical Advection Experiments," *Mon. Wea. Rev.* **96**, 1–11 (1968).

Dietrich, D. E., D. S. Ko, and L. A. Yeske, "On the Application and Evaluation of the Relocatable DieCAST Ocean Circulation Model in Coastal and Semi-Enclosed Seas," Technical Report 93-1, Mississippi State University Center for Air Sea Technology, 1993, 79 pp.

Dietrich, D. E. and D. S. Ko, "A Semi-Collocated Ocean Model Based on the SOMS Approach," *International J. Num. Methods in Fluids* **19**, 1103–1113 (1994).

Dietrich, D. E. and A. Mehra, "A Semi-Implicit Free Surface Formulation for the Semi-Collocated Grid DieCAST Ocean Model," Technical Report 03-98, Mississippi State University, Center for Air Sea Technology, 1998, 13 pp.

Dukowicz, J. K. and R. D. Smith, "Implicit Free-Surface Method for the Bryan-Cox-Semtner Ocean Model," *J. Geophys. Res.* **99**, 7991–8014 (1994).

Haidvogel, D., J. Wilkin, and R. Young, "A Semi-Spectral Primitive Equation Ocean Circulation Model Using Sigma Vertical and Orthogonal Curvilinear Horizontal Coordinates," *J. Comp. Phys.* **94**, 151–184 (1991).

Haney, R. L., "On the Pressure Gradient Force Over Steep Topography in Sigma Coordinate Ocean Models," *J. Phy. Oceanog.* **21**, 610–619 (1991).

Hecht, M. W., W. R. Holland, and P. J. Rasch, "Upwind-Weighted Advection Schemes for Ocean Tracer Transport: An Evaluation in a Passive Tracer Context," *J. Geophys. Res.* **100**, 20,763–20,778 (1995).

Jerlov, N. G., *Marine Optics* (Elsevier Publishing Co., New York, NY, 1968), 231 pp.

Johnson, B. H., R. E. Heath, B. B. Hsieh, K. W. Kim, and H. L. Butler, "User's Guide for a Three-Dimensional, Numerical, Hydrodynamic, Salinity and Temperature Model of Chesapeake Bay," Technical Report HL-91-20, U.S. Army Corps of Engineers Waterways Experiment Station, Vicksburg, MS, 1991.

Killworth, P. D., D. Stainforth, D. J. Webb, and S. M. Paterson, "The Development of a Free-Surface Bryan-Cox-Semtner Ocean Model," *J. Phys. Oceanog.* **21**, 1333–1348 (1991).

Ko, D. S., pers. comm.

LeBlond, P. H. and L. A. Mysak, *Waves in the Ocean* (Elsevier Publishing Co., New York, NY, 1978), 602 pp.

Long, P. E. and D. W. Pepper, "An Examination of Some Simple Numerical Schemes for Calculating Scalar Advection," *J. Appl. Met.* **20**, 146–156 (1981).

Lynch, D. R. and F. E. Werner, "Three-Dimensional Hydrodynamics on Finite Elements, Part II: Non-Linear Time-Stepping Model," *Int. J. Numer. Methods Fluids* **12**, 507–534 (1991).

Martin, P. J., "Simulation of the Mixed Layer at OWS N and P with Several Models," *J. Geophys. Res.* **90**, 903–916 (1985).

Martin, P. J., "Testing and Comparison of Several Mixed-Layer Models," NORDA Report 143, Naval Research Laboratory, Stennis Space Center, MS, 1986.

Martin, P. J., "An Ocean Model with a Combined Sigma and z-Level Vertical Coordinate System," Naval Research Laboratory, Stennis Space Center, MS (in prep.).

McRae, G. J., W. R. Goodin, and J. H. Seinfeld, "Numerical Solution of the Atmospheric Diffusion Equation for Chemically Reacting Flows," *J. Comp. Phys.* **45**, 1–42 (1982).

Mellor, G. L. and T. Yamada, "A Hierarchy of Turbulence Closure Models for Planetary Boundary Layers," *J. Atmos. Sci.* **31**, 1791–1806 (1974).

Mellor, G. L. and T. Yamada, "Development of a Turbulence Closure Model for Geophysical Fluid Problems," *Geophys. and Space Phys.* **20**, 851–875 (1982).

Mellor, G. L. and P. A. Durbin, "The Structure and Dynamics of the Ocean Surface Mixed Layer," *J. Phys. Oceanog.* **5**, 718–728 (1975).

Mellor, G. L. and A. F. Blumberg, "Modeling Vertical and Horizontal Diffusivities with the Sigma Coordinate System," *Mon. Wea. Rev.* **113**, 1379–1383 (1985).

Mellor, G. L., *User's Guide for a Three-Dimensional, Primitive-Equation, Numerical Ocean Model*, (Princeton University, Princeton, NJ, 1996), 39 pp.

Mesinger, F. and A. Arakawa, "Numerical Methods Used in Atmospheric Models, Volume I," Global Atmospheric Research Program (GARP) Publications Series No. 17, 1976, 64 pp.

Molenkamp, C. R., "Accuracy of Finite-Difference Methods Applied to the Advection Equation," *J. Appl. Met.* **7**, 160–167 (1968).

Naimie, C. E., J. W. Loder, and D. R. Lynch, "Seasonal Variation of the Three-Dimensional Residual Circulation on Georges Bank," *J. Geophs. Res.* **99**, 15,967–15,989 (1994).

Orszag, S. A., "Numerical Simulation of Incompressible Flows Within Simple Boundaries: Accuracy," *J. Fluid. Mech.* **49**, 75–112 (1971).

Paul, J. F., "Observations Related to the use of the Sigma Coordinate Transformation for Estuarine and Coastal Modeling Studies," in Estuarine and Coastal Modeling III, Proceedings of the 3rd International Conference, M. Spaulding, K. Bedford, A. Blumberg, R. Cheng, and C. Swanson (eds.), American Society of Civil Engineers, New York, NY, 1994, 682 pp.

Purnell, D. K., "Solution of the Advective Equation by Upstream Interpolation with a Cubic Spline," *Mon. Wea. Rev.* **104**, 42–48 (1976).

Rivas, E. K., "On the Use of Nonuniform Grids in Finite-Difference Equations," *J. Comp. Phys.* **10**, 202–210 (1972).

Roache, P. J., *Computational Fluid Dynamics* (Hermosa Publishers, Albuquerque, NM, 1976), 446 pp.

Shannon, J. D., "A Gaussian Moment-Conservation Diffusion Model," *J. Appl. Met.* **18**, 1406–1414 (1979).

Simpson, J. H. and I. D. James, "Coastal and Estuarine Fronts," in *Baroclinic Processes on Continental Shelves*, C. N. K. Mooers (ed.), (American Geophysical Union, Washington, D.C., 1986), 130 pp.

Smagorinsky, J., "General Circulation Experiments with the Primitive Equations. I: The Basic Experiment," *Mon. Wea. Rev.* **91**, 99–164 (1963).

Song, Y. and D. Haidvogel, "A Semi-Implicit Ocean Circulation Model Using a Generalized Topography-Following Coordinate System," *J. Comp. Phys.* **115**, 2428–2441 (1994).

Smolarkiweicz, P. K. and W. W. Grabowski, "The Multidimensional Positive Definite Advection Transport Algorithm: Nonoscillatory Option," *J. Comp. Phys.* **86**, 355–375 (1990).

Stocker, T. and K. Hutter, *Topographic Waves in Channels and Lakes on the f-Plane, Lecture Notes on Coastal and Estuarine Studies* (Springer-Verlag, New York, NY, 1987), 176 pp.

Yamada, T. and G. L. Mellor, "A Simulation of the Wangara Atmospheric Boundary Layer Data," *J. Atmos. Sci.* **32**, 2309–2329 (1975).

Wolff, J., E. Maier-Riemer, and S. Legutke, "The Hamburg Ocean Primitive Equation Model (HOPE)," Technical Report No. 13, ISSN 0940-9327, Max-Planck Institute for Meteorology, Hamburg, Germany, 1996, 103 pp.

Appendix A

STABILITY ANALYSIS FOR SURFACE WAVE PROPAGATION

The properties of a numerical scheme can be determined by performing a stability analysis of the scheme. Here we will analyze the propagation of surface waves in the models using a procedure referred to as a von Neumann stability analysis. This analysis can provide information about the stability and damping properties of the scheme and about the dispersion or phase speed error. A good discussion of the von Neumann stability analysis can be found in Mesinger and Arakawa (1976), and a discussion of the analysis of the Asselin filter can be found in Asselin (1972). We will look at the propagation of surface waves for the case where $f = 0$, which significantly simplifies the analysis of the numerical schemes.

The general procedure is to substitute a solution of the form

$$\zeta(x,\ t) = Z(t)e^{ikx} \tag{A1}$$

into the linearized numerical equations, where Z is the time-dependent part of the solution and k is the horizontal wavenumber. This allows the determination of the behavior of a single Fourier spatial mode of wavelength $L = 2\pi/k$. One then solves for the amplification factor $\lambda = Z^{(n+1)}/Z^{(n)}$, which is, in general, complex. The magnitude or modulus of λ denotes the stability and damping properties of the scheme, i.e., how the magnitude of the solution changes on successive timesteps. From the phase change of λ each timestep, the propagation speed of the waves in the numerical solution can be computed.

The linearized equations for the propagation of surface gravity waves in the x-direction for $f = 0$ are

$$\frac{\partial u}{\partial t} = -g\frac{\partial \zeta}{\partial x}, \tag{A2}$$

$$\frac{\partial \zeta}{\partial t} = -H\frac{\partial u}{\partial x}. \tag{A3}$$

A1. STABILITY ANALYSIS FOR SURFACE WAVES IN POM

For POM, the numerical scheme for the propagation of surface waves is an explicit leapfrog scheme with an Asselin temporal filter. The finite difference forms of (A2) and (A3) for this numerical scheme are

$$u^{(n+1)} = A[u^{(n-1)}] - 2\Delta t g\frac{\zeta^{(n)}_{i+\frac{1}{2}} - \zeta^{(n)}_{i-\frac{1}{2}}}{\Delta x}, \tag{A4}$$

$$\zeta^{(n+1)} = A[\zeta^{(n-1)}] - 2\Delta t H \frac{u^{(n)}_{i+\frac{1}{2}} - u^{(n)}_{i-\frac{1}{2}}}{\Delta x} . \tag{A5}$$

A [ ] denotes application of the Asselin filter, which is defined as

$$A[u^{(n)}] = u^{(n)} + \nu(u^{(n-1)} - 2u^{(n)} + u^{(n+1)}) , \tag{A6}$$

where ν is the filter coefficient.

Substitution of the solution form (A1) into the numerical equations (A4)–(A6) and solving for λ gives

$$\lambda = (iq + \nu) \pm ((1-\nu)^2 - q^2)^{\frac{1}{2}} , \tag{A7}$$

where

$$q = (gH)^{\frac{1}{2}} \frac{2\Delta t}{\Delta x} \sin\left(\frac{k\Delta x}{2}\right) . \tag{A8}$$

Hence, the amplification each timestep is

$$|\lambda| = ((1-\nu)^2 + \nu^2 + 2\nu\,((1-\nu)^2 - q^2)^{\frac{1}{2}})^{\frac{1}{2}} \tag{A9}$$

and the phase change each timestep is

$$\omega\Delta t = \tan^{-1}\,(q/((1-\nu)^2 - q^2)^{\frac{1}{2}} + \nu) , \tag{A10}$$

where ω is the frequency. The phase speed is then given by

$$c = \frac{\omega}{k} = \frac{1}{\Delta t k}\tan^{-1}(q/(((1-\nu)^2 - q^2)^{\frac{1}{2}} + \nu)) . \tag{A11}$$

Note that for $\nu = 0$ we get $|\lambda| = 1$, i.e., there is no damping of the basic leapfrog scheme without the Asselin filter. The damping is due entirely to the filter.

A2. STABILITY ANALYSIS FOR SURFACE WAVES IN ECOM-SI

For ECOM-si, the numerical scheme for the propagation of surface waves is a two-time-level, fully implicit scheme, i.e.,

$$u^{(n+1)} = u^{(n)} - \Delta t g \frac{\zeta^{(n+1)}_{i+\frac{1}{2}} - \zeta^{(n+1)}_{i-\frac{1}{2}}}{\Delta x} , \tag{A12}$$

$$\zeta^{(n+1)} = \zeta^{(n)} - \Delta t H \frac{u^{(n+1)}_{i+\frac{1}{2}} - u^{(n+1)}_{i-\frac{1}{2}}}{\Delta x} . \tag{A13}$$

Again, substitution of the solution form (A1) into the numerical equations (A12)–(A13) and solving for λ gives

$$\lambda = \frac{1 \pm iq}{1+q^2} . \tag{A14}$$

Hence, the amplification each timestep is

$$|\lambda| = (1+q^2)^{-\frac{1}{2}} \tag{A15}$$

and the phase change each timestep is

$$\omega \Delta t = \tan^{-1}(q) . \tag{A16}$$

The phase speed is then given by

$$c = \frac{\omega}{k} = \frac{1}{\Delta t k} \tan^{-1}(q) . \tag{A17}$$

Note that the amplification factor is always less than 1, i.e., the scheme is always stable.

A.3 STABILITY ANALYSIS FOR SURFACE WAVES FOR SZM

For SZM, the numerical scheme used in this report for the propagation of surface waves is a trapezoidal implicit, leapfrog scheme with an Asselin temporal filter. The finite difference form of (A4)–(A5) for this scheme is

$$u^{(n+1)} = A[u^{(n-1)}] - \Delta t g \frac{\zeta^{(n+1)}_{i+\frac{1}{2}} - \zeta^{(n+1)}_{i-\frac{1}{2}}}{\Delta x} - \Delta t g \frac{A[\zeta^{(n-1)}_{i+\frac{1}{2}}] - A[\zeta^{(n-1)}_{i-\frac{1}{2}}]}{\Delta x} , \tag{A18}$$

$$\zeta^{(n+1)} = A[\zeta^{(n-1)}] - \Delta t H \frac{u^{(n+1)}_{i+\frac{1}{2}} - u^{(n+1)}_{i-\frac{1}{2}}}{\Delta x} - \Delta t H \frac{A[u^{(n-1)}_{i+\frac{1}{2}}] - A[u^{(n-1)}_{i-\frac{1}{2}}]}{\Delta x} . \tag{A19}$$

Substitution of the solution form (A1) into the numerical equations (A18), (A19), and (A6) (for the Asselin filter) and solving for λ gives

$$\lambda = (\nu \pm ((1-\nu)^2 + q^2(1-2\nu))^{\frac{1}{2}}) \frac{1+iq}{1+q^2} . \tag{A20}$$

Hence, the amplification each timestep is

$$|\lambda| = (\nu + ((1-\nu)^2 + q^2(1-2\nu))^{\frac{1}{2}})(1+q^2)^{-\frac{1}{2}} \tag{A21}$$

and the phase change each timestep is

$$\omega\Delta t = \tan^{-1}(q)\,, \tag{A22}$$

where ω is the frequency. The phase speed is then given by

$$c = \frac{\omega}{k} = \frac{1}{\Delta t k}\tan^{-1}(q)\,. \tag{A23}$$

The amplification is always less than or equal to 1 and the scheme is always stable. When $\nu = 0$, we get $|\lambda| = 1$, i.e., there is no damping of the waves. Hence, like POM, the damping of the waves is due entirely to the Asselin filter. The phase speed error is the same as for ECOM-si, and is not affected by the value of ν.

Figures 37–39 show plots of the phase speed error and damping of the numerical schemes as a function of the Courant Number $C_u = (gH)^{1/2}\,\Delta t/\Delta x$ and the number of gridpoints per wavelength that are used to resolve the wave. The phase speed error is expressed as the percent error relative to the analytically determined phase speed for the wave, and the damping is expressed as the percent damping per wave period based on the analytically calculated wave period. The damping

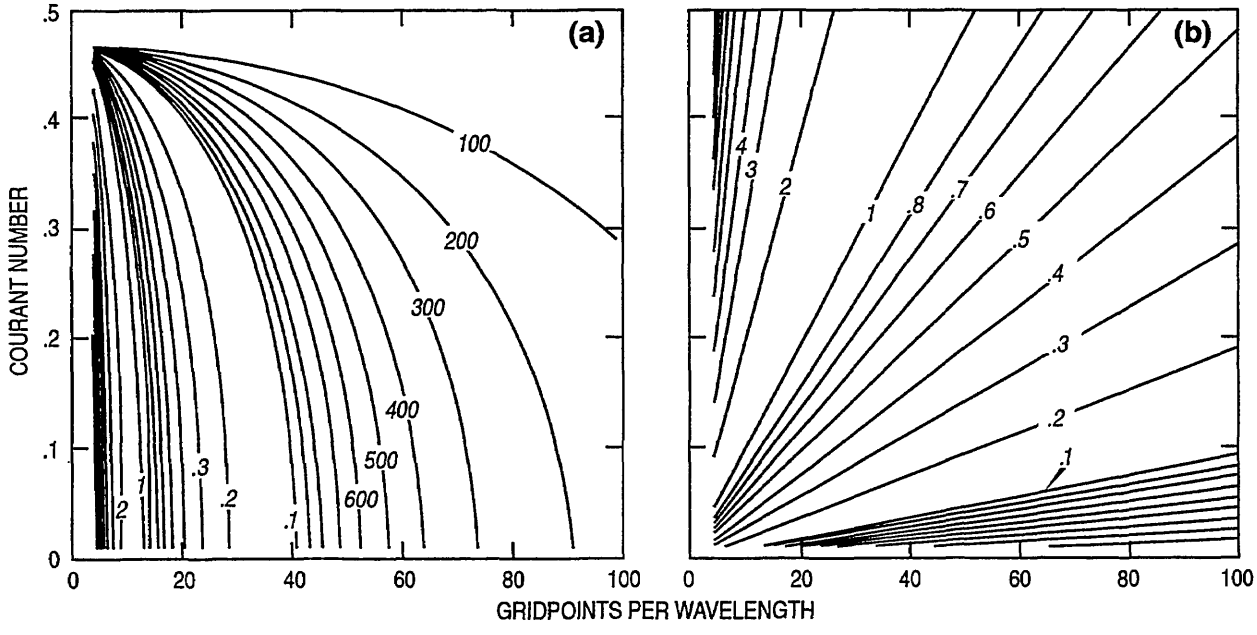

Fig. 37 — (a) Phase speed error and (b) damping for the numerical scheme used by POM for the free surface mode. The phase speed error is expressed as the percent error relative to the analytically calculated phase speed. The damping is expressed as the percent damping per wave period based on the analytically calculated wave period. The Asselin filter coefficient for this calculation is set to 0.05. Contour labels less than 0.1 are multiplied by 10,000.

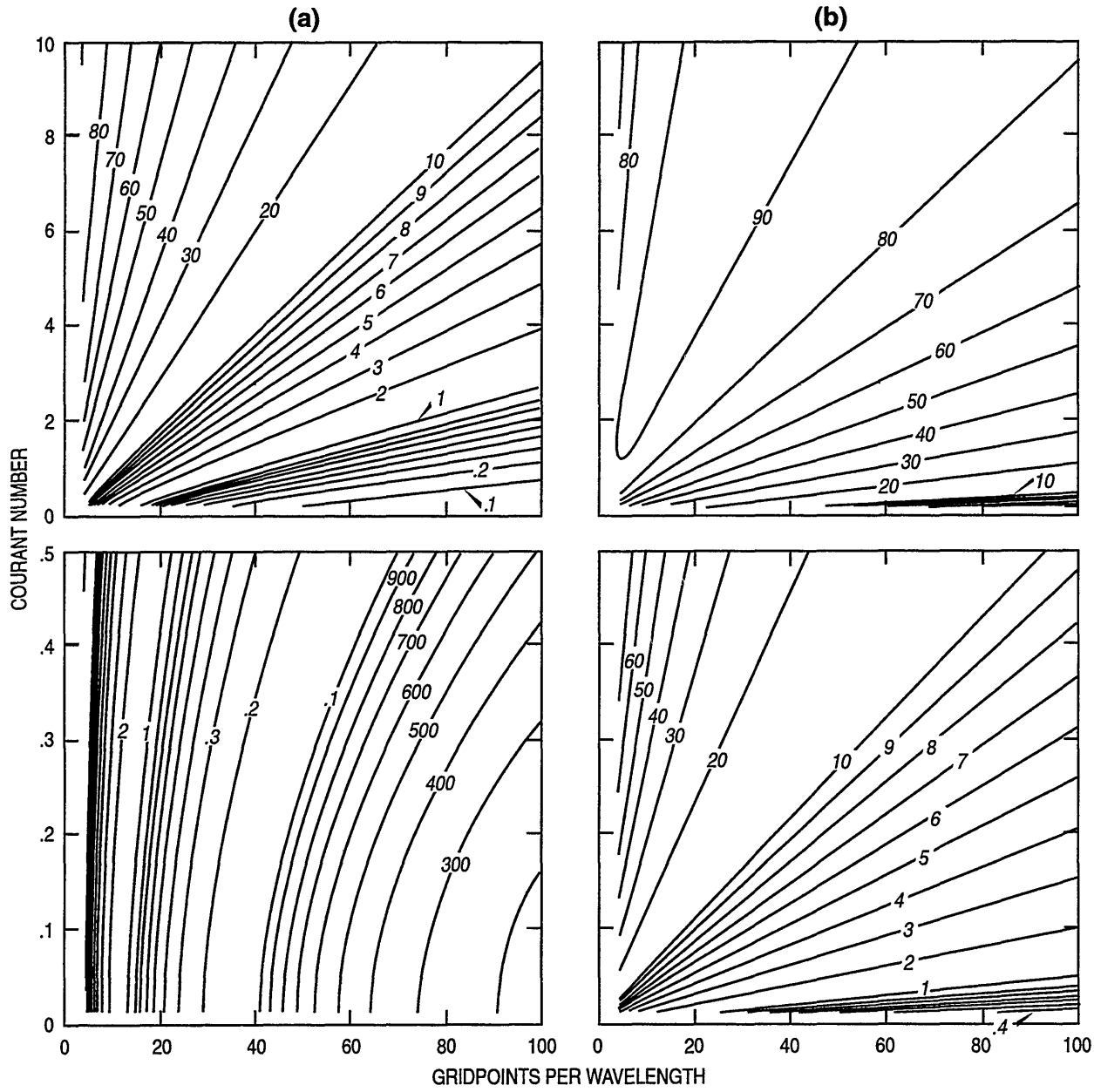

Fig. 38 — Same as Fig. 37, but for ECOM-si

error for POM and SZM depends on the value of the Asselin filter coefficient ν. For the plots in Figs. 37 and 39, ν was set to the typically used value of 0.05. Values are shown for POM only for values of C_u less than 0.5, since POM's explicit scheme is unstable for $C_u > 0.5$.

The phase speed error for all three schemes is the same at very low values of C_u, but whereas the phase speed error for POM decreases as C_u increases (up to the point at which POM's explicit scheme becomes unstable at $C_u = 0.5$), the phase speed error for ECOM-si and SZM (which is the same) increases. The damping for POM and SZM is similar for $C_u < 0.5$ and is much less than

the damping of ECOM-si at the same value of C_u. Of course, it must be remembered that ECOM-si and SZM will typically be using much larger values of C_u for surface waves than POM because of the small, barotropic timestep used by POM.

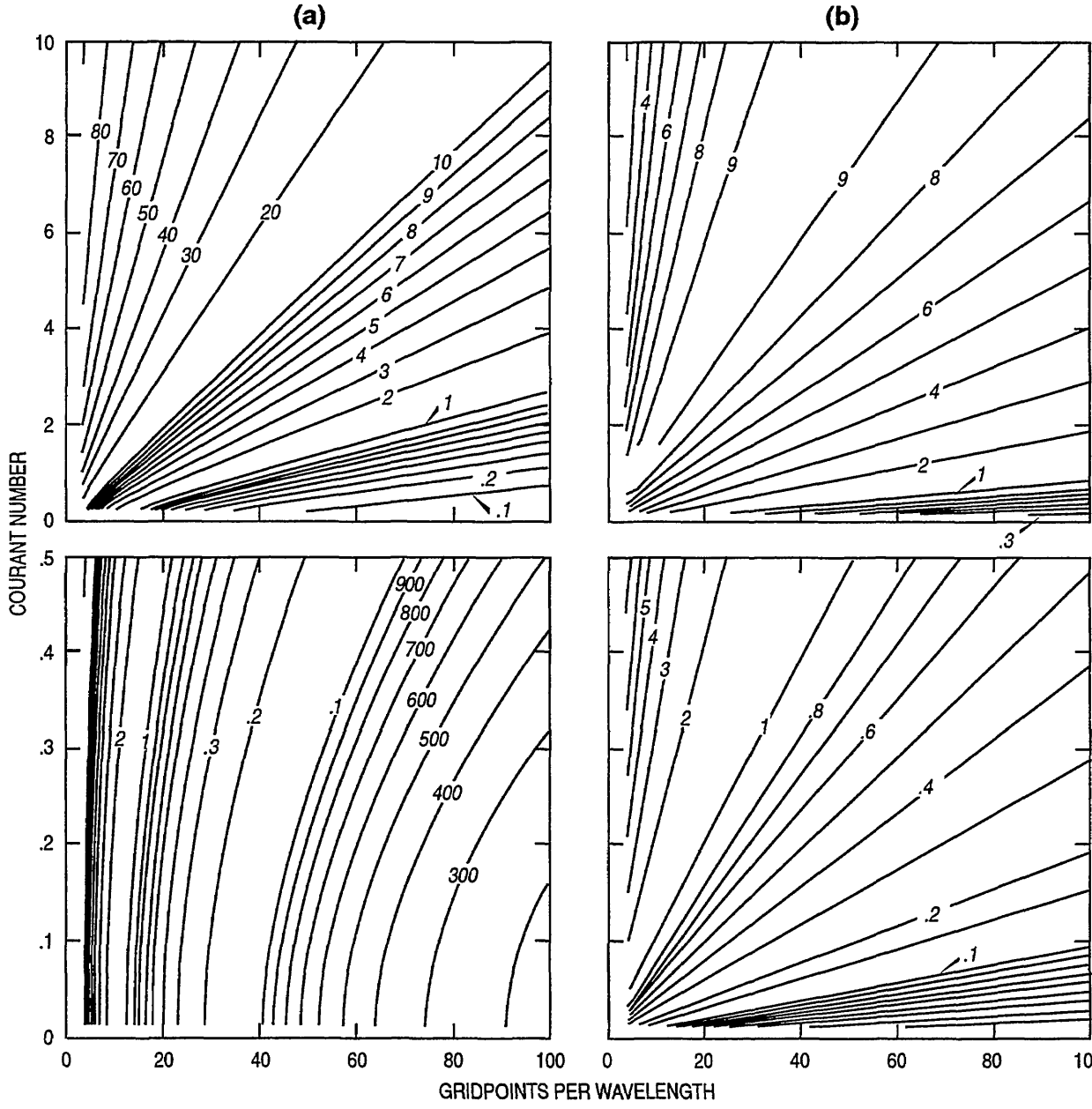

Fig. 39 — Same as Fig. 37, but for SZM. The Asselin filter coefficient for this calculation is set to 0.05.

Appendix B

INTERNAL WAVE PROPAGATION ERROR WITH ECOM-SI

The propagation of internal gravity waves with ECOM-si resulted in some modification of the ambient stratification. An analysis of internal gravity wave propagation with ECOM-si's forward time-differencing scheme led to the conclusion that this is primarily due to numerical diffusion of the ambient stratification caused by a phase (timing) error between the salinity and velocity terms in the salinity equation's vertical advection term.

The main terms governing the propagation of internal waves are the horizontal baroclinic pressure gradient and the vertical advection of density. For internal wave propagation as described in Sec. 6.0, i.e., for propagation in the x-direction with the vertical density gradient being due to salinity stratification, and with $f = 0$, the relevant momentum and salinity equations are

$$\frac{\partial u}{\partial t} = -\frac{1}{\rho_o}\frac{\partial p}{\partial x}, \tag{B1}$$

$$\frac{\partial S}{\partial t} = -\frac{\partial (wS)}{\partial z}. \tag{B2}$$

The salinity field can be split into two parts, one part S_o that describes the ambient stratification, which, for the problem being considered here, depends only on depth, and another part S' that describes the changes in the ambient salinity field due to the propagating wave, i.e.,

$$S(x,\ z,\ t) = S_o(z) + S'\ (x, z, t). \tag{B3}$$

Hence, the salinity equation can be written as

$$\frac{\partial S}{\partial t} = -\frac{\partial (wS_o)}{\partial z} - \frac{\partial (wS')}{\partial z}. \tag{B4}$$

For small amplitude waves, the main contribution to the vertical advection of salinity is due to the vertical advection of the ambient stratification S_o. The contribution from the vertical advection of S' is small.

With the two-time-level numerical scheme used by ECOM-si, the momentum is first updated using the horizontal pressure gradient that has been calculated using the old temperature and salinity values

$$u^{(n+1)} = u^{(n)} - \frac{\Delta t}{\rho_o} \frac{\partial p^{(n)}}{\partial x}, \tag{B5}$$

and then the new salinity is calculated using the newly calculated velocities for the advection term

$$S^{(n+1)} = S^{(n)} - \Delta t \frac{\partial (w^{(n+1)} S^{(n)})}{\partial z}. \tag{B6}$$

This calculation sequence can be conceptualized as a leapfrogging of the momentum and density terms in time (Fig. 40), even though the model is not explicitly written as if this were the case. With this leapfrogging, the velocity and salinity fields are offset from each other by half a timestep and the main terms describing the internal wave propagation are accurately centered in time, i.e., the salinity used for the calculation of the horizontal pressure gradient is located between the old and new values of u, and the velocity used for advection of salinity is located between the old and new values of S.

A quantity, however, that is not centered in time is the value of S used in the advection term. The value that is used is the old value $S^{(n)}$, which effectively lags $w^{(n+1)}$ by half a timestep. Since most of the contribution to the salinity advection is from the ambient salinity stratification S_o, only a secondary contribution to the salinity advection suffers from a phase lag error. However, it is this phase lag of S in the advection term that results in the modification of the ambient salinity stratification.

If (B4) is horizontally averaged over one wavelength, we get an expression for the rate of change with time of the horizontally averaged salinity $\overline{S(z,t)}$

$$\frac{\partial \bar{S}}{\partial t} = -\frac{\partial \overline{(wS_o)}}{\partial z} - \frac{\partial \overline{(wS')}}{\partial z}, \tag{B7}$$

where the overbar indicates a horizontal average. The first term on the right side of (B7) is zero, since S_o has no horizontal variation and $\overline{w} = 0$. The second term on the right side of (B7) describes the time

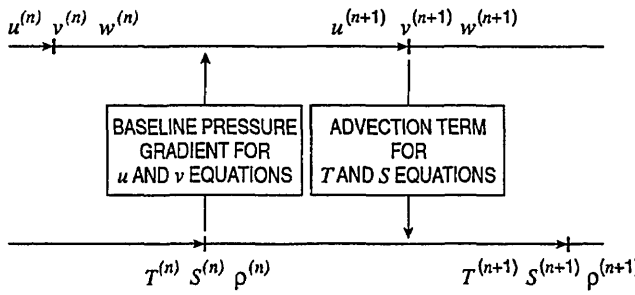

Fig. 40 — Schematic showing the effective leapfrogging in time of the momentum and salinity conservation equations of ECOM-si for the main internal gravity wave terms

rate of change of the horizontally averaged salinity due to the vertical divergence of the salt flux defined by $\overline{wS'}$. Using (74) and (75) from Sec. 6.0, we can write wS' as

$$wS' = A^2 \frac{N^2 \omega}{\beta g} \sin^2 (mz) \sin (kx - \omega t) \cos (kx - \omega t) \; . \tag{B8}$$

If (B8) is horizontally averaged over one wavelength, the product of sin $(kx - wt)$ and cos $(kx - wt)$ integrates to zero, i.e., there is no net vertical flux of salt due to the passage of the internal wave. However, if there is an error in the phase of S' relative to w, the horizontal average of (B8) will not be zero.

Since we estimate that for internal wave propagation in ECOM-si, the value of S in the salinity advection term effectively lags w by half a timestep, we get

$$wS' = A^2 \frac{N^2 \omega}{\beta g} \sin^2 (mz) \sin (kx - \omega t) \cos (kx - \omega (t - \Delta t/2)) \; . \tag{B9}$$

Using some trigonometric relations, this becomes

$$wS' = -A^2 \frac{N^2 \omega}{\beta g} \sin^2 (mz) \sin^2 (kx - \omega t) \sin (\omega \frac{\Delta t}{2}) \; . \tag{B10}$$

Taking the horizontal average over one wavelength gives

$$\overline{wS'} = -A^2 \frac{N^2 \omega}{2\beta g} \sin^2 (mz) \sin (\omega \frac{\Delta t}{2}) \; . \tag{B11}$$

Hence, the mean vertical flux of salinity due to the phase lag of S' with respect to w is downward. Note that the direction of this flux is against the ambient salinity gradient. The rate of change of the salinity with time is given by the negative of the spatial derivative of the flux and is

$$\frac{\partial \bar{S}}{\partial t} = -\frac{\partial (\overline{wS'})}{\partial z} = A^2 \frac{N^2 \omega m}{2\beta g} \sin (2mz) \sin (\omega \frac{\Delta t}{2}) \; . \tag{B12}$$

The results of the analysis predict that the rate of change of the background stratification with time depends on the sine of the phase error between w and S in the salinity advection term, and is proportional to the square of the amplitude of the internal wave.

Figure 41a shows a comparison of S' calculated by (B12) with the result from ECOM-si at 24 h for the propagation of the 8-km wavelength internal wave reported in Sec. 6.0 with Δt = 200 s. Also shown are comparisons from two similar experiments – one in which the amplitude of the wave was increased from 100 to 200 cm with Δt kept at 200 s and another in which the amplitude was increased to 400 cm and the timestep was increased to 400 s. The comparisons show good agreement between the analysis and the results from ECOM-si in terms of the structure and amplitude of the change in the ambient stratification. At the higher wave amplitudes, the analysis appears to overestimate the change in the ambient stratification slightly.

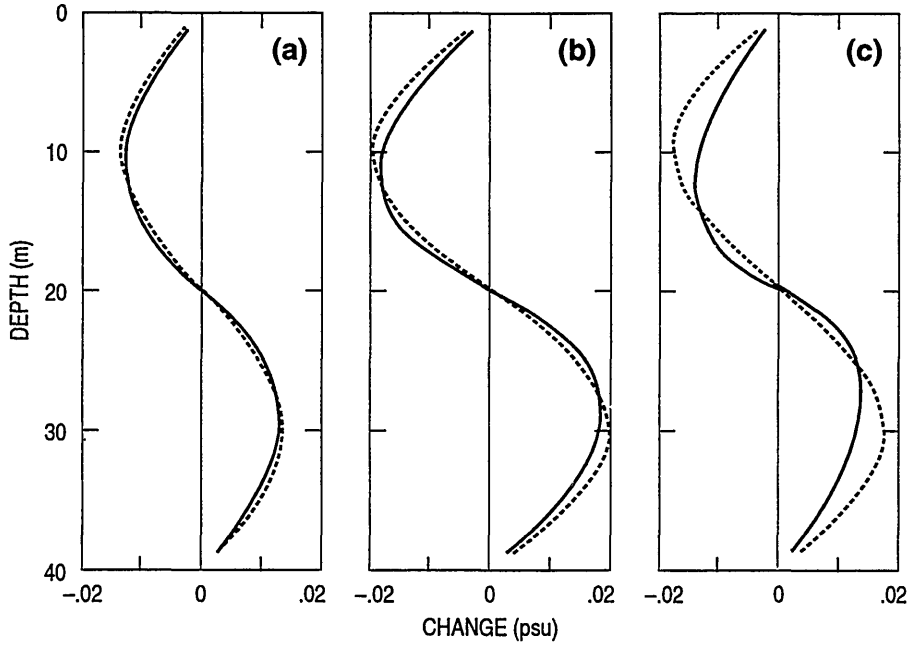

Fig. 41 — Change in ambient stratification during internal wave propagation for ECOM-si (solid line) and as predicted by numerical analysis (dashed line) after 24 h. The wavelength is 8 km. The internal wave amplitude and timestep are (a) 100 cm and 200 s, (b) 200 cm and 200 s, and (c) 400 cm and 400 s.

Appendix C

ANALYTICAL SOLUTION FOR TOPOGRAPHIC WAVES WITH STAIRSTEP BOTTOM

The linearized equations for barotropic shelf waves propagating in the x-direction along a straight coast with bathymetry varying only in the offshore direction are

$$\frac{\partial u}{\partial t} = fv - g\frac{\partial \zeta}{\partial x}, \tag{C1}$$

$$\frac{\partial v}{\partial t} = -fu - g\frac{\partial \zeta}{\partial y}, \tag{C2}$$

$$0 = -H\frac{\partial u}{\partial x} - \frac{\partial Hv}{\partial y}. \tag{C3}$$

Note that the time derivative has been scaled out of the continuity equation. This term is not essential to the physics of small-amplitude, topographic waves, and its elimination simplifies the solution of the equations (LeBlond and Mysak 1978).

Cross-differentiation of the momentum equations yields the vorticity equation

$$\frac{\partial}{\partial t}\left(\frac{\partial v}{\partial x} - \frac{\partial u}{\partial y}\right) = -f\left(\frac{\partial u}{\partial x} + \frac{\partial v}{\partial y}\right). \tag{C4}$$

Based on the continuity equation, we can define a stream function Ψ where

$$u = -\frac{1}{H}\frac{\partial \Psi}{\partial y}, \tag{C5}$$

$$v = \frac{1}{H}\frac{\partial \Psi}{\partial x}. \tag{C6}$$

Substituting the stream function into the vorticity equation, we get

$$\left(\frac{1}{H}\frac{\partial^2 \Psi}{\partial x^2} + \frac{\partial}{\partial y}\left(\frac{1}{H}\frac{\partial \Psi}{\partial y}\right)\right) = \frac{f}{H^2}\frac{\partial H}{\partial y}\frac{\partial \Psi}{\partial x}. \tag{C7}$$

We can assume a traveling wave solution in x of the form

$$\Psi = \Psi'(y)e^{i(kx-\omega t)}, \tag{C8}$$

where k is the along-shore wavenumber and ω is the frequency.

Substituting into (C7) and dropping the prime on Ψ, we get an equation for the cross-shore structure of the topographic wave

$$\frac{\partial}{\partial y}\left(\frac{1}{H}\frac{\partial \Psi}{\partial y}\right)+\left(\frac{fk}{\omega H^2}\frac{\partial H}{\partial y}-\frac{k^2}{H}\right)\Psi=0\,. \tag{C9}$$

This equation can be solved for a particular bathymetry $H(y)$.

For a region of constant depth, (C9) simplifies to

$$\frac{\partial^2 \Psi}{\partial y^2}-k^2\Psi=0\,. \tag{C10}$$

Solutions of this equation have the form of cosh and sinh functions.

Since a step-wise bathymetry consists of a series of adjoining regions of uniform depth, with a discontinuity in the depth between each region, the solution can be represented as cosh or sinh functions within each region of uniform depth, with the amplitude of the functions determined by appropriate matching conditions between the regions.

For a domain extending from $y = 0$ to $y = L_y$, in which the depth between y_{j-1} and y_j is H_j for $j = 1$ to $j = m$, the solution within the region from y_{j-1} to y_j can be represented as

$$\Psi_j = A_j\ \sinh(ky) + B_j\ \cosh(ky)\,. \tag{C11}$$

Boundary conditions of zero transport ($\Psi = 0$) at $y = 0$ and $y = L_y$ give

$$\Psi_1 = \sinh(ky)\,, \tag{C12}$$

$$\Psi_m = A_m\ \sinh(k(y-L_y))\,. \tag{C13}$$

The unknowns A_j, B_j, and ω can be determined from the matching conditions between the regions at each y_j (Stocker and Hutter 1987)

$$\Psi_j = \Psi_{j+1}\,, \tag{C14}$$

$$\left(\frac{\partial \Psi_j}{\partial y}-\frac{kf}{\omega}\Psi_j\right)\frac{1}{H_j}=\left(\frac{\partial \Psi_{j+1}}{\partial y}-\frac{kf}{\omega}\Psi_{j+1}\right)\frac{1}{H_{j+1}}\,. \tag{C15}$$

This coupled set of $2m-2$ equations for the cross-shore structure of the topographic wave for a stairstep bottom can be solved numerically using a shooting method.